

# Advanced MTI methods for spaceborne radars and their application to the SwarmSAR concept

by

# Guillermo de Dios

to obtain the degree of Master of Science at the Delft University of Technology, to be defended publicly on Monday January 1, 2024 at 10:00 AM.

Student number: 5610099

Project duration: November 19, 2024 – August, 2025

Thesis committee: Prof. Dr. A. Yaravoy, TU Delft, supervisor, chair

Prof. Dr. ir. F. Lopez Dekker TU Delft Dr. F. Fioranelli, TU Delft TNO

Cover: SAR in Multi-sensor Data Collection by ICEYE

An electronic version of this thesis is available at http://repository.tudelft.nl/.





The work presented in this thesis was performed as part of a graduation internship at TNO.

Company supervisors: Dr. M. Caro Cuenca A. Bazzoni



# Preface

With the completion of this Master's thesis, my time at TU Delft and in the Netherlands comes to an end. These have been two years full of learning and personal growth that I will remember for the rest of my life. I want to start by thanking my parents for giving me the opportunity to study at this university and for always being willing to help me with everything I needed. To my girlfriend, for always supporting me and helping me find joy in everyday moments. And to my friends, for making this journey easier and for all the laughter we have shared.

I would also like to thank my main supervisor at TNO, Miguel, for trusting me with the opportunity to explore such an interesting and meaningful topic, as well as for always being available to support me and help push the project forward. Additionally, I want to thank Alessandro, who, along with Miguel, participated in the weekly meetings. I truly enjoyed our discussions on how to tackle the challenges that arose, always approached with a smile and a strong commitment to delivering the best possible project. They consistently provided me with valuable feedback and helped me not only to develop my own ideas but also to learn how to critically assess them.

I would also like to thank Olexander for his role as my academic supervisor on behalf of the university. He has always supported me with feedback that helped me shape a higher-quality project and has consistently looked out for my best interests since the day this project was proposed. Lastly, I want to thank the entire MS3 group, with a special thanks to Francesco, for always being willing to help and for offering new perspectives on ideas related to the project.

Guillermo de Dios Delft, August 2025

# **Abstract**

One of the main challenges of Moving Target Indication (MTI) with spaceborne radars is distinguishing moving targets from strong ground clutter, primarily due to the high velocity of the radar platform. This issue is particularly pronounced in spaceborne systems, where satellites in Low Earth Orbit (LEO) travel at speeds of approximately 7,000 m/s. Such rapid motion causes a broadening of the clutter Doppler spectrum, making it especially difficult to detect slowly moving targets, as their signals are often masked by the clutter. To address this challenge, advanced MTI techniques are required, which rely on multiple receiving antennas arranged along the flight direction and separated by a defined baseline. These multiple antennas enable spatial sampling, allowing the system to resolve differences not only in Doppler frequency but also in angle, thereby enhancing the ability to separate moving targets from ground clutter. Among these techniques, Space-Time Adaptive Processing (STAP) has been the most extensively studied in the literature, as it offers full adaptivity in both space and time domains.

In this study, we implement STAP and evaluate its efficiency in a SwarmSAR system, which is a multi-static spaceborne radar configuration where each satellite carries a single antenna and serves as an individual element of the distributed array. To the best of our knowledge, STAP has not previously been applied in such a configuration. The results demonstrate that STAP can be effectively applied, with clutter suppression improving as the target moves further from the clutter subspace. Due to the significantly larger baselines in SwarmSAR systems compared to the wavelength, targets can be detected at relatively low velocities (below 1 m/s). However, these large baselines are also the primary limitation to STAP performance in a SwarmSAR topology. They give rise to grating lobes, which cause angular ambiguities that, due to the coupling between angle of arrival and target velocity introduced by platform motion, translate into velocity ambiguities. Consequently, multiple angle-velocity pairs fall within the clutter subspace, making it impossible to detect targets with those specific combinations.

Moreover, when the baselines are large enough that each satellite measures a different target velocity—differing by more than the velocity resolution—the efficiency of STAP decreases by a factor equal to the array processing gain, and each satellite produces a separate detection. To address this, we propose a strategy to achieve the same observation geometry across all satellites. Results from this approach demonstrate that it is possible to recover the array processing gain and achieve a single detection per target. Additionally, when the baselines are non-uniform, the ambiguities in angle of arrival and target velocity are also resolved. It is important to note that these results were obtained under several ideal assumptions, including perfect synchronization and phase stability between satellites, precise knowledge of satellite positions, and stationary clutter.

# Contents

Lis	st of Figures	viii
Lis	st of Tables	ix
Lis	st of Abbreviations	X
1	Introduction  1.1 Motivation  1.1.1 SwarmSAR project  1.2 Problem Definition  1.3 Literature review  1.3.1 State-of-the-art  1.3.2 Research novelty  1.4 Thesis focus and goals  1.5 Thesis structure	1 1 2 2 4 4 7 8
2	Theoretical background  2.1 Radar Concepts	10 10 11 12 13 14 14 16 17
3	Simulation Setup 3.1 System Geometry and Parameters 3.2 Rough surface response 3.3 Received signal 3.4 Doppler processing 3.5 Summary	18 18 18 21 22 25
4	Classical STAP applied to SwarmSAR  4.1 Metrics  4.2 Interference Covariance Matrix  4.2.1 Orthogonal Projection of Clutter Subspace  4.2.2 Eigenvalues Analysis  4.3 STAP Processing  4.3.1 Proposed Methodology  4.3.2 STAP Performance Results  4.4 Summary	33
5	Proposed approach for STAP in SwarmSAR  5.1 Motivation	42 43 43 44 44 45 46

Contents	V
COILLEILLS	VJ

		Proposed Approach Results	47 50
_	6.1	Conclusion and Future Lines  Conclusion	
Re	fere	nces	57

# List of Figures

1.1	Representation of the SwarmSAR concept. It is a MIMO system where FDM is used for transmission. The receiver bandwidth is equal to the number of antennas times the bandwidth of a single antenna [5]	2
1.2 1.3 1.4	Lines of Constant Clutter Doppler Frequency for Level Flight above a Flat Earth.[10] Spatial-Frequency filter representation in Angle-Doppler plane [6]	3 3 5
1.5	Uniform Linear Array beamformer and the radar data cube utilized by STAP for its processing operations [6]	6
2.1 2.2 2.3	Pulse radar range ambiguity. $\Delta T$ represents the actual time delay of the echo from target B while $\Delta t$ shows the time delay that the radar measures [59]	11 13 15
3.1 3.2	Geometry of the problem	19
3.3 3.4 3.5	ization	20 21 21
3.6	range cell after range compression and implementation of radar range equation (b) Range-Doppler plot of 5 scatterers with a central one centered around cero velocity: (a)	22
3.7	without azimuth compression, (b) with azimuth compression	24 25
4.1	Representation of the three satellites positions over four consecutive time instances with only one satellite transmitting $(S_1)$ for $N_{DPCA}=2$ (a) and for $N_{DPCA}=3$ (b). Each time instance represents the moment where the first satellite transmits. The location of the equivalent phase centers for the bistatic acquisitions is represented with triangles	29
4.2	Estimated normalized clutter covariance Matrix for $PRF=1000$ Hz and $N_{DPCA}=2$ and 10 integrated pulses (a) and its respective normalized eigenvalues with the corresponding threshold that indicates the estimated separation between the noise and the clutter	
4.3	eigenvalues (b)	30
4.4	eigenvalues (b)	31
4.5	eigenvalues (b)	32
4 6	eigenvalues (b)	32 33

List of Figures viii

4.7 4.8	Interference covariance matrix convergence for 25 m, 50 m, and 100 m baselines Power spectrum of (a) obtained eigenvalues and (b) true eigenvalues for 25 meter base-	35
	line with a PRF of 8150 Hz	36 37
4.11	line with a PRF of 8150 Hz	38 38
	Power spectrum of (a) obtained eigenvalues and (b) true eigenvalues for 100 meter baseline with a PRF of 8150 Hz	39
	Angle-Doppler Improvement Factor (a) and $SCNR_{Loss}$ (b) for 100 meters baseline FFT over the slow-time data in the target's range cell for each satellite. The resulting velocity estimates for the target are 5.2, 5.3, and 5.4 m/s for satellites 1, 2, and 3, respectively.	39
4.15	tively	40
	velocity of 0 m/s, and (b) at a fixed angle of 0 degrees	40
5.1 5.2	Workflow of proposed approach for STAP in a SwarmSAR system	43
5.3	scheduled to start recording reflections at that moment. On the right, a zoomed-in view along the red dotted line highlights the virtual baseline $\Delta x$	44
5.4	for both uniform and non-uniform baselines configurations	46 48
5.5	Angle-Doppler Improvement Factor (a) and $SCNR_{Loss}$ (b) for 450 meters baseline using the proposed approach	40
5.6	Power spectrum of (a) obtained eigenvalues and (b) true eigenvalues for 450 meter	
5.7	baseline in the proposed approach	50
5.8	baselines, 450 meters and 700 meters, using the proposed approach	51
	Uniform Baselines (450 m and 700 m)	51
5.9	Angle-Doppler Improvement Factor (a) and $SCNR_{Loss}$ (b) for non uniform non uniform baselines, 450 meters and 700 meters, using the proposed approach	52
5.10	Power spectrum of (a) obtained eigenvalues and (b) true eigenvalues for non uniform baselines, 450 meters and 700 meters, using the proposed approach	53

# List of Tables

1.1	Assumptions throughout the Thesis	9
3.1	System parameters	19
4.1	Comparison of the number of dominant eigenvalues for various baselines under DPCA condition for 3 satellites and 10 integrated pulses	33
4.2	Parameters for STAP performance analysis	34
4.3	Classical STAP results	40
5.1	Parameters for performance analysis of STAP proposed approach	47
5.2	Parameters for performance analysis of STAP proposed approach	50
5.3	Proposed approach results	52

# List Of Abbreviations

ATI Along-Track Interferometry

**DPCA** Displaced Phase Center Antenna

**CPI** Coherent Processing Interval

**FFT** Fast Fourier Transform

**GMTI** Ground Moving Target Indication

**IF** Improvement Factor

**IFFT** Inverse Fast Fourier Transform

**ISTAP** Imaging Space-Time Adaptive Processing

**LEO** Low Earth Orbit

LFM Linear Frequency ModulationMDV Minimum Detectable VelocityMIMO Multiple-Input Multiple-Output

MTI Moving Target Indication

MSAR Multichannel Synthetic Aperture Radar

**PRF** Pulse Repetition Frequency

**PRI** Pulse Repetition Interval

RCM Range Cell Migration
RDC Range-Doppler Cell
RCS Radar Cross-Section

**RX** Receiver

**SAR** Synthetic Aperture Radar

**SCNR** Signal-to-Clutter-plus-Noise Ratio

SIMO Single-Input Multiple-Output

**SNR** Signal-to-Noise Ratio

**STAP** Space-Time Adaptive Processing

TX Transmitter

**ULA** Uniform Linear Array

# Introduction

## 1.1. Motivation

Radar systems have become indispensable tools in modern technology due to their flexibility and utility. These are active sensors that transmit radio-frequency electromagnetic waves. They are capable not only of measuring the range of targets, but also of tracking, identifying, imaging, and classifying them, while effectively suppressing strong environmental interference. Initially used only for military purposes, they now have a wide variety of applications, such as remote sensing, autonomous navigation, meteorology and space exploration.

In the context of moving target tracking, stationary radar stations equipped with rotating antennas were originally used for this task. This method limits the angular resolution achievable by the antenna beamwidth, which is inversely proportional to the antenna size. Therefore, in this scenario, the use of large antennas is required. In Synthetic Aperture Radar (SAR), a large antenna aperture is artificially created by coherently combining signals collected over time from a moving radar platform such as an aircraft or a satellite [1]. Having a radar on these platforms is also very convenient for ground moving target indication (GMTI). In comparison with ground radars, they offer a wider area coverage with a better line of sight and lower ground clutter. Although SAR systems can provide high-resolution images of the earth's surface, they are unable to detect moving objects with a lower velocity than the radar platform (such as ground moving vehicles) [2]. This problem is even greater in space radars, since satellites move at a relatively high speed. Not only that they cannot be not be detected, but also moving objects present a problem for the quality of SAR images quality, as they are represented blurred and displaced from their actual potion, due to the additional Doppler shift [3]. However, showing moving targets detections at the top of the SAR image is important for many applications, such as military operations.

In contrast to the classical airborne MTI situation, it is not possible to use a a particularly narrow beamwidth, as this worsens the azimuthal resolution in SAR images. A solution to this problem is to implement multiple receiving antennas which are arranged in the flight direction and separated by a certain baseline. The use of multichannel SAR (MSAR) is capable of suppressing clutter and estimating the motion and position parameters of the targets [2]. One suitable technique is space-time adaptive processing (STAP) combines spatial and temporal radar samples in a finite response filter to cancel stationary clutter while providing maximal gain on target [4]. Unlike airborne radars, the application of this technique in space-based radars has the advantage of achieving worldwide coverage in all weather conditions and of not requiring a specific mission for each pass.

1.2. Problem Definition 2

#### 1.1.1. SwarmSAR project

In the context of MSAR, the SwarmSAR concept was introduced in [5], and to the best of our knowledge, it represents the first proposal of its kind. It consists of a closed formation of simple, self-sufficient and equal satellites that aims to exploit multi-static radar capabilities through their mutual cooperation. Simple nodes means that satellites cannot have complex beam-steering or digital beam-forming capabilities. This implies that each satellite will only include a single antenna. In addition, they are expected to fly with a short along-track separation, in an orbit height of 514 km (low Earth orbit (LEO)) and illuminate a common footprint, ensuring all antennas are pointed at the same area on the ground. Another relevant feature of a SwarmSAR is that it allows MIMO configurations where all satellites must transmit simultaneously using frequency division multiplexing (FDM) with S-Band frequency and 20 MHz of transmitted signal bandwidth. The receiver bandwidth of each satellite shall be wide enough to receive all signals (i.e. it will be equal to the number of channels multiplied by the single channel bandwidth). Overall, this system aims to improve imaging capabilities due to MSAR, while offering good flexibility and cost-effectiveness. Fig.1.1 shows a representation of the SwarmSAR concept

In addition to enhancing SAR images quality, this system has a great potencial for GMTI. It meets the multiple channels requirement but it also has the peculiarity that the aperture of the antenna array will be extremely large, since each satellite will have an antenna and they will be separated by more than a hundred meters. A larger antenna length improves the detection capability of slowly moving targets masked in the clutter, because the clutter bandwidth is reduced [6]. The implementation of a STAP technique in a SwarmSAR has the potential to perform better than any other existing system by obtaining a lower minimum detectable velocity (MDV) for a certain target radar cross-section (RCS). As an example, one of the few satellites that combines GMTI with MSAR is the RADARSAT-2 [7], which operates in C-Band and is equipped with a 15 meter long phased-array antenna. This system is capable of detecting a target with a RCS that exceeds 10  $m^2$  and a MDV higher than 5 m/s with the implementation of STAP [8]. A baseline greater than one hundred meters in a SwarmSAR is expected to improve performance, although the use of such a large baseline will also include new difficulties, such as ambiguities in the spatial domain due to a separation greater than half the wavelength between array elements.

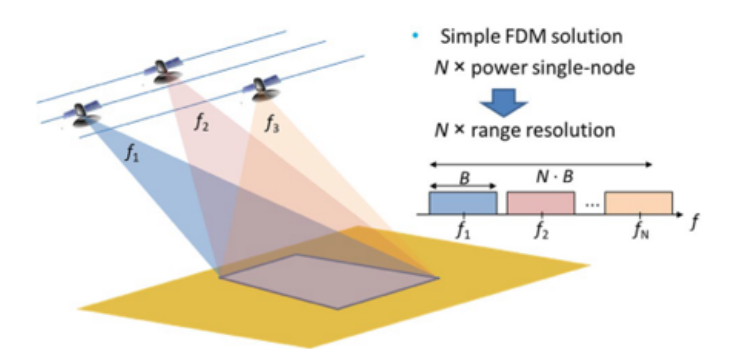


**Figure 1.1:** Representation of the SwarmSAR concept. It is a MIMO system where FDM is used for transmission. The receiver bandwidth is equal to the number of antennas times the bandwidth of a single antenna [5]

#### 1.2. Problem Definition

The main difficulty of MTI with Spaceborne radars is to distinguish moving targets from the strong ground clutter, because of the high velocities of the radar platform motion. This problem is especially accentuated in spaceborne radars since the velocity of a satellite in a LEO orbit is around 7000 m/s. This motion causes a spread of the clutter Doppler spectrum so that especially signals backscattered from slowly moving targets are masked and, hence, cannot be detected [4]. This masking occurs because for normal ground reflectivity per unit area, range resolution and antenna beam values, the RCS will be around 30 dB bigger than a normal vehicle RCS, which is around 10  $m^2$  [9]. On the other hand, to understand why the spread of the clutter spectrum occurs it is important to introduce the following

1.2. Problem Definition 3

relationship of the measured Doppler frequency from the ground and the angle between the direction of flight and the direction of the scatterer  $\phi$ 

$$f_D = -\frac{2v_p}{\lambda}cos\phi \tag{1.1}$$

where  $v_p$  is the platform velocity and  $\lambda$  is the wavelength. This relationship makes surfaces of constant radial velocity, and thus constant clutter Doppler frequency, which are cones around the direction of flight [10]. The lines in the ground of constant radial velocity are formed by the intersection of the cones with the surface plane. These constant radial velocity lines are shown in Fig.1.2.

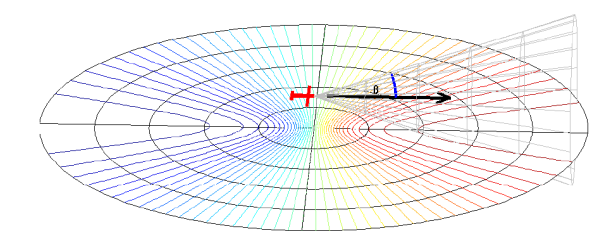


Figure 1.2: Lines of Constant Clutter Doppler Frequency for Level Flight above a Flat Earth.[10]

In addition, the clutter Doppler spectrum is shaped by the antenna beam. For low PRF radars, such as those commonly used in SAR, main lobe and sidelobe clutter may completely fill the Doppler space. To quantify how much the ground clutter will affect the detection of slow moving targets, it is important to note the expression of the transmitted main beam in the clutter spectrum. For side-looking radars where the antenna beam points perpendicular to the flight direction the bandwidth of main beam of the clutter spectrum is equal to [6]:

$$B_C \approx \theta_{3dB} \cdot \frac{2v_p}{\lambda} = 0.886 \cdot \frac{2v_p}{L_a}$$
 (1.2)

where  $\theta_{3dB}$  is the transmitted main lobe beamwidth and  $L_a$  is the length of the antenna. With this equation we can see that for our very high satellite velocities, the echo spectrum of ground moving targets (with low velocity) will be entirely submerged in the extended ground clutter spectra. This means that the ground clutter cannot be just filtered in the Doppler domain, as it would inevitably reduce the energy of useful signals. Note that this spread is invariant with radar frequency if one assumes that the antenna size does not change. Therefore single-channel GMTI is restricted either to fast moving targets whose Doppler shifted signals lie outside the clutter bandwidth, or to targets with high RCS. Fig.1.3 shows a representation of a space-time filter for a side-looking radar in a moving platform.

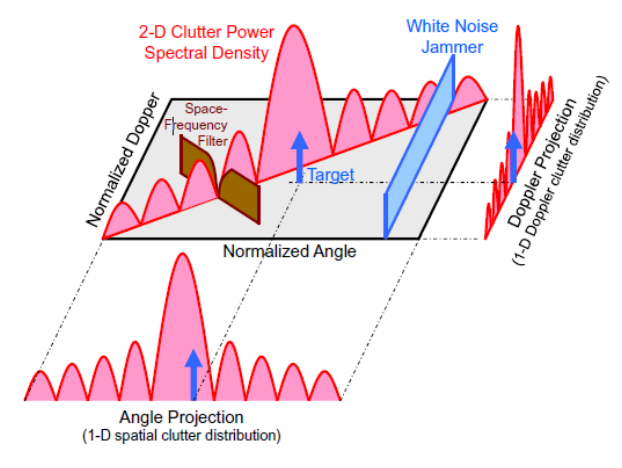


Figure 1.3: Spatial-Frequency filter representation in Angle-Doppler plane [6]

The angle axis of Fig.1.3 is represented by the normalized directional of cosine which is also the normalized spatial frequency  $f_s = d_r cos(\phi)/\lambda$ , where  $d_r$  is the distance between the receiving antennas. Moreover, the frequency axis is equal to the normalized Doppler frequency of the clutter  $f_n = 2vTcos(\phi)/\lambda$ , where T is the pulse reptetition interval (PRI). This is known as the clutter ridge and can be also defined with respect to the normalized spatial frequency as  $f_n = \beta f_s$ , where  $\beta = 2vT/d_r$ . With this last equation we clearly see the linear relationship between the cosine of the angle of arrival and the resulting Doppler frequency represented in Fig.1.3, where the inclination of the ridge depends on the projected platform velocity on the ground versus azimuth angle. Note that the intensity of the signal at different frequencies and angles is modulated by the transmitting beam. Therefore, the clutter is strongest at mid-beam, where the Doppler frequency is cero. The key is that the moving targets will have their return echoes shift out of the clutter ridge as a function of their velocities over the ground. For this reason, advanced MTI techniques that operate in both the spatial and temporal domain are necessary to detect these targets from a moving platform.

## 1.3. Literature review

This section contains a summary of the state-of-art work done in the area of STAP algorithms for MTI in a SAR scenario and the research gaps identified in the literature.

#### 1.3.1. State-of-the-art

The last section discusses why classical MTI techniques are ineffective for moving platforms, requiring the use of spatial samples from multiple channels to exploit the dependence of the clutter on the angle of arrival. Over the last decades, three techniques have been the most frequently mentioned in the literature, displaced phase center antenna (DPCA), along-track interferometry (ATI) and STAP. DPCA techniques were first introduced and they are motivated by the classical two-pulse canceller MTI. Since platform motion causes clutter Doppler spreading, DPCA aims to maintain the moving aperture over two successive pulses. This is achieved by aligning the transmit and receive phase centers over two or more pulses. For this purpose, the distance between phase centers must be equal to an integer multiple of the distance the platform travels between pulses. Subtraction of the received pulses will eliminate ground clutter but retain the target signal due to its motion [11, 12].

In the literature of recent years, multiple works have analysed the performance of this GMTI technique in simulations of different SAR systems, especially in airborne radars [13–19]. The results show that ground vehicles with a mid-high RCS (10-15  $dBm^2$ ) at velocities of a few meters per seconds can be detected (less than 5 m/s). Note that the results are highly dependent on the speed of the platform. For example, in the experiment analyzed in [17], an airborne radar with a speed of only 55 m/s is used, yielding a MDV of less than 1 m/s. In addition, the antenna length is also important (as discussed in section 1.2), and this is reflected in the results of [15], where they increase the aperture by using a bistatic configuration with two platforms (one for transmitter and one for receiver). Nevertheless, the simplest way to implement this technique is by using an array of antennas on the same platform, where the first pulse is received by one-half of the antenna, while the second pulse is received by the other half. In [19] A. Hussain et al. implement this method for an airborne radar obtaining a MDV of 5m/s for a 2  $m^2$  RCS target. However, this kind of implementation requires speficic requirements between radar platform speed, length of the antenna and the pulse repetition frequency. To mitigate this dependence but still maintain good performance, [20] proposes a method introducing a correction signal to the two received pulse signals in the first stage of cancellation in spaceborne radar.

In addition, A DPCA analysis has been performed by L. Lightstone et al. for different numbers of received phase centers and different distances between them in [21]. The results show that an important factor in detecting the slowest possible target is not the number of receive phase centers but the maximum separation between them. Nevertheless, since DPCA was originally designed for two-channel radar system, it is suboptimal for a larger number of receiver (RX) channels. For this reason, D. Cerutti-Maori and I. Sikaneta recently proposed a method for a generalization of DPCA for any number of RX channels, called extended displaced phase (EDPCA) [22]. Each of the RX channels generates a SAR image with a consistent effective phase center across pulses. The key aspect is that each image is processed using a compression filter matched to the moving target's parameters, thereby maximizing the target's signal-to-noise ratio (SNR). Next, the clutter-plus-noise covariance matrix is estimated

by averaging the measured data, and this estimate is subsequently used to filter the MSAR complex images, effectively reducing clutter. This proposed algorithm is then partially adapative, as it is only adaptive in slow time and not in the spatial domain. In addition, [22] demonstrates that meeting the DPCA condition (phase center separation must be an integer multiple of the platform's displacement per pulse) still remains essential for achieving high performance.

In the SAR imaging context, ATI is a another technique that is really similar to DPCA. In ATI, the phase of two complex SAR images, taken under identical geometries and separated by a short time interval, is compared when their transmitter and receiver phase center are aligned. A phase difference greater than zero indicates a moving target [12]. For instance, if two satellites are obtaining a mono-static SAR image, the phase center would correspond to the actual satellite position and the ATI implementation would consist of just subtracting the phase difference from both satellites when they are in the same spatial position.

A comparison between ATI and DPCA for this configuration is represented in Fig.1.4. Nevertheless, this technique has the drawback that the estimated radial velocity of a moving target may be ambiguous due to the interferometric phases being nearly wrapped. Different solutions for this problem are proposed in [23, 24]. Another disadvantage of this method is that it is highly sensitive to phase difference errors and the velocity accuracy is determined by the accuracy of the interferometric parameters. For this reason, there has been work conducted on sensitivity analysis of ATI [25–27]. In addition, the implementation of ATI in combination with DPCA has also been proposed, where DPCA first gives a rough estimate and then ATI is used improve the estimation [28, 29].

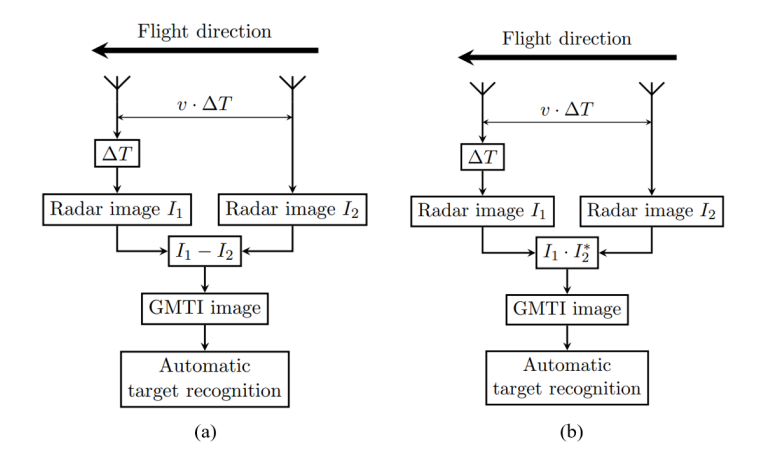


Figure 1.4: Comparison between DPCA (a) and ATI (b) techniques for two monostatic SAR images. [12]

Regarding the current space-based system that use MSAR, one of the few is the German TerraSAR-X [30] which is a dual-channel SAR satellite. It has been tested for both ATI and DPCA in traffic monitoring by F. Meyer et al. in [31]. The results of this study indicate that at low velocities, ATI provides better results, as low phase values are more susceptible to noise, which significantly degrades DPCA performance since it purely relies on the interferometric phase. On the other hand, ATI makes also use of the amplitude, so one additional feature is still left for detection. Yet, slow moving cars where hard to distinguish from non moving background. This motivated S.V. Baumgartner and G. Krieger in [32] to introduce a novel method for GMTI using the formation TanDEM-X based on two TerraSAR-X radar satellites [33].

The key to making this algorithm work is that distance between both satellites is on the order ten to several tens of kilometers which is, so far in the published literature, the formation of satellites used for GMTI with the largest baseline. Due to the significant time lag caused by the large baseline, even slow-moving targets shift across multiple range and azimuth resolution cells between the two SAR observations. As a result, their positions appear displaced in the conventionally processed SAR images. By applying 2-D cross-correlation to estimate this displacement, it is possible to accurately determine the target's true geographic location, velocity, and direction of motion—without ambiguity. However, in contrast with a SwarmSAR it requires two channels per antenna and it is fixed for two satellites.

On the other hand, STAP is a technique that also operates in the spatial-temporal domain but, unlike DPCA and ATI, it is fully adaptive in both domains requiring simultaneous processing of spatial and temporal samples, provided by multiple echoes in a coherent processing interval (CPI) of the radar [4]. Therefore, the angle of arrival can also be estimated with this technique, but it requires an estimation of the clutter-plus-noise covariance matrix from the received data to compute an adaptive weight vector that corresponds to a beamformer that operates in the angle-Doppler plain. Fig.1.5 shows the radar data cube that STAP uses to operate, as well as the implementation of the weight vector on the received data. In [34], T. J. Nohara compared DPCA and STAP in a space-based radar system, highlighting that DPCA can be viewed as a special case of STAP with a temporal-spatial constraint. The study showed that STAP significantly outperforms DPCA, particularly when the phase centers are not collinear with the platform's motion vector. Moreover, DPCA is only optimum for two receiver channels while STAP is optimum for any number of them. On the downside, STAP requires a higher antenna complexity to obtain the same results and higher computational load.

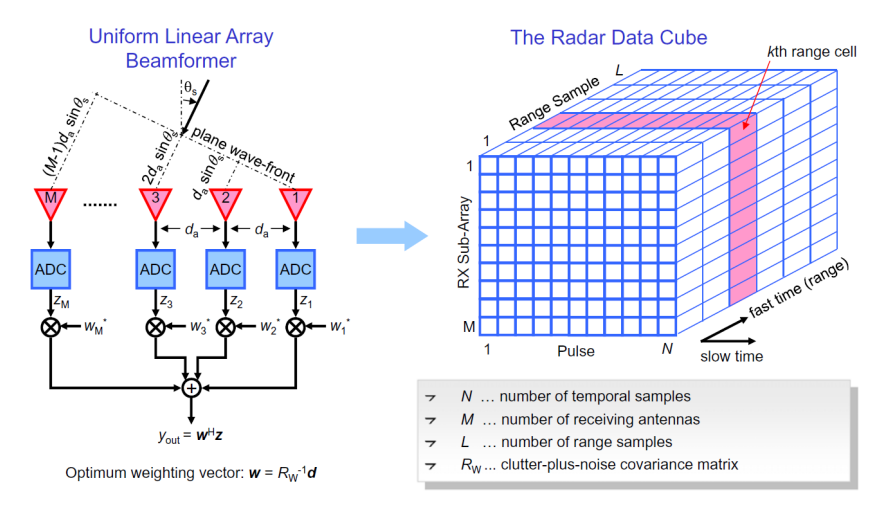


Figure 1.5: Uniform Linear Array beamformer and the radar data cube utilized by STAP for its processing operations [6]

Moreover, STAP requires an accurate estimation of the clutter-plus-noise covariance matrix, which presents two main challenges: the limited number of available samples and the high computational burden. These challenges are critical to achieving high performance with STAP and they have been extensively addressed in recent literature. In [35–37] they employ techniques that project the data into a lower dimension to reduce the rank of the covariance matrix, which leads to improved performance, especially when the number of available samples for estimation is small (sometimes even smaller than the original rank of the covariance matrix). In addition to these, one of the most mentioned reduced-dimension techniques in the literature is Post-Doppler STAP (PD-STAP), which transforms the received data into the Doppler domain before STAP processing takes places [2]. It requires that the target and clutter remain in the same range-Doppler resolution cell during the integration time. Performance analysis of PD-STAP has been conducted across various configurations, demonstrating that it is both a practically implementable and efficient algorithm [38–42].

Other than rank reduction, there is also work that exploits prior information of properties of the covariance matrix to obtain a more robust estimation, such as [43] using cyclic characteristics. Additionally, several studies have explored the integration of STAP with Multiple-Input Multiple-Output (MIMO) radar systems, as they are advantageous for GMTI systems due to waveform diversity, perspective, longer illumination time and the larger aperture [44]. Since incorporating a MIMO configuration directly increases the volume of received data proportional to the number of transmitters, recent literature has addressed this challenge through low-rank MIMO approaches [45–47]. The results show an approximate full dimension optimum performance, while the computational complexity can be significantly decreased. On the other hand, there are works involving MIMO STAP performance for different diversity transmitted waveforms [48, 49].

In all the works mentioned above, the analysis of STAP has focused on airborne radar systems that include multiple receiver channels in their platform. This is because there are few articles that study the implementation of STAP in spaceborne systems. Among them, the largest number of articles is on the study of STAP using a single satellite with multiple RX channels and the most relevant ones are shown next. In [50], F. Yang et al. analyzed the performance of STAP under various clutter distribution models, showing that these models have a negligible impact on overall performance. In the work conducted by J.H.G. Ender et al. in [51] a novel method was proposed to generate additional independent phase centers on a fixed number of RX channels by trading off unambiguous bandwidth of the system.

This is achieved by alternating the RX channels used in consecutive pulses, which enhances STAP performance as additional degrees of freedom can be introduced. In the context of SAR imaging at the same time as STAP, D. Cerutti-Maori et al. proposed a new method called imaging STAP (ISTAP) which is a combinations of PD-STAP and SAR [52]. As with EDPCA, a SAR compression filter is matched to the moving target parameters for maximizing the target SNR. In contrast, with PD-STAP all available pulses are coherently processed, not only the ones that ensure that a moving target stays in one range-Doppler cell. The increase of SNR shows a maximization of the detection probability and it is of great interest in systems such as RADARSAT-2 due to the significant SNR losss reduction when using a smaller CPI [53]. It has been tested for RADARSAT-2 in traffic monitoring and for ship detection and results show that an accurate estimation can be obtained from space without knowledge of the street network [9] [54].

There are even fewer articles in the literature on the performance analysis of STAP in a multistatic (i.e multiple satellites) configuration for space-based radars. One of them is conducted by D.J.E. Cerutti-Maori and J.H.G. Ender in [55]. In this work, one of the subapertures operates at transmission, whereas all the subapertures are used for coherent multistatic reception of the echoes. A suboptimal approach is proposed, which involves beamforming toward both the target source and interference cells to significantly reduce the volume of data that needs to be processed. It is adapted for small baselines (around a 100 meters) and it enables the detection of targets moving at very low velocities while providing highly accurate estimation of their direction of motion.

Moreover, in this same configuration some research has also been done on the problem of spatial ambiguities and the grating lobes due to undersampling in spatial frequency, when using a large baseline between satellites in [56]. They propose a method based on waveform diversity and non-equal subarray distances to reduce the ambiguities. Furthermore, another study on multistatic STAP has been conducted by X. Li et al. in [57]. What makes this article particularly interesting is that it considers a configuration with a single channel per satellite—that is, one antenna per satellite as in SwarmSAR. In a MIMO scenario, the study provides an accurate prediction of STAP performance to analyze the impact of nonstationary clutter and nonideal orthogonal waveforms. The performance expression is validated through simulations, revealing that higher cross-correlation energy between waveforms leads to degraded STAP performance. However, the study maintains a fixed baseline of only 200 meters, and does not investigate the influence of varying baseline lengths on performance. One more article that studies STAP performance in a multistatic scenario with a single channel per satellite is also conducted by X. Li et al. in [58]. They implement STAP in a scenario where there is also cross-track baseline and they a novel method for a more robust selection of the training samples used for the estimation of the clutter covariance matrix to oververcome the difficulty of terrain clutter suppression in hybrid baseline radar system.

#### 1.3.2. Research novelty

The state-of-the-art review reveals that three main advanced MTI techniques have been implemented and studied over the past decades, with single-platform airborne radars featuring multiple channels being the most commonly employed configuration. These articles not only assess the performance of advanced MTI techniques across various systems, but also propose enhancements aimed at reducing implementation complexity and improving overall effectiveness. Among these techniques, Space-Time Adaptive Processing (STAP) stands out as the only method that is fully adaptive in both spatial and temporal domains. Its main disadvantage is the increased antenna complexity and the significantly higher computational burden compared to methods that are adaptive only in either the spatial or temporal domain. Although STAP has been extensively studied, the number of publications significantly decreases

when the focus shifts to its implementation in spaceborne radar systems, as opposed to airborne platforms. Between them, the most repeated studied configuration involves a single satellite equipped with multiple channels. Some of the few existing SAR satellites with multiple channels such as RADARSAT-2 and TerraSAR have been analysed for their effectiveness in applying ATI, DPCA and STAP [31, 48, 49].

But there are even less articles regarding a multistatic satellite system used for MTI. One of them is on the TanDEM-X formation based on two TerraSAR-X satellites [32]. They proposed a novel method for a large satellite baseline (on the order of ten to several tens of kilometers) designed for a fixed number of two nodes. An additional one is [55], which proposes a reduced-dimension STAP technique for a variable number of satellites and the performance its analyzed for three satellites, yielding high effectiveness.

Nevertheless, both of these MTI techniques require multiple channels on each satellite to function effectively. This is not the case for the work in [57, 58] which are one of the only articles that study STAP performance in a multistatic configuration where each satellite is equipped with a single channel. However, the satellite baseline is fixed at only a few hundred meters, and the number of satellites remains constant at three. To the best of my knowledge, current existing work done in literature does not implement and analyze advanced MTI algorithms performance in a multistatic spaceborne system comprising one antenna per satellite (such as SwarmSAR), for different number of satellites and large distances of at least 500 meters. Therefore the research novelty can be summarized as:

• The implementation and performance analysis of STAP algorithm for different satellite formation topologies on a multistatic spaceborne system with a single antenna per node.

## 1.4. Thesis focus and goals

Based on the current state of the art, gaps in the literature have been identified, and the novelty of this research has been established. Consequently, the aim of this thesis is to answer the following research question:

 How is the performance of STAP going to be influenced by the topology of a multistatic spaceborne system with a single antenna per node, such as a SwarmSAR system?

This question can be further divided into the following subquestions

- Can STAP be efficiently implemented in a SwarmSAR system?
- How does the system geometry influence STAP performance in a SwarmSAR system?
- What strategies can be used to better manage the configurations required in a SwarmSAR system?

Accordingly, this thesis focuses on analyzing the performance of STAP as a function of the distances between satellites in a Single-Input Multiple-Output (SIMO) configuration. Therefore, one satellite will serve as both the transmitter and a receiver (monostatic), while the remaining satellites will function solely as receivers (bistatic). The simulations to test the performance of the STAP processing through the thesis are done on a SIMO SwarmSAR thesis with a fixed number of satellites three satellites, but with varying baselines.

Although SwarmSAR is a MIMO system, it can also be regarded as a multiple SIMO system. In terms of complexity, the problem is simplified while still representing a realistic initial approach. In addition, throughout this thesis, a flat Earth model will be assumed, along with ideal synchronization among satellites and the absence of phase noise. Note that to ensure perfect synchronization it is necessary to know the exact time at which the signals were received. In practice, this is not a trivial matter because of how fast and how distant the satellites will be. A good estimation of the reception time is outside the scope of this thesis and requires another extensive study. Regarding the clutter, it will be assumed to be stationary for a simplification, although in practice ground can experience slight motion during the integration time (such as trees movement due to wind). The following table outlines the assumptions made throughout the project:

1.5. Thesis structure 9

# Assumptions Perfect synchronization between satellites Perfect phase stability between satellites No phase noise in the satellite oscillators Stationary clutter Perfect knowledge of satellite positions Flat earth

Table 1.1: Assumptions throughout the Thesis

## 1.5. Thesis structure

The rest of this thesis will be organized as follows. Chapter 2 presents the background theory necessary to understand the work carried out in this thesis and to address the research questions. This includes fundamental radar concepts and signal processing techniques such as pulse compression and digital beamforming. The chapter concludes with an introduction to the theory of STAP. Building on this theoretical foundation, Chapter 3 provides a detailed explanation of how satellite reflections are modeled and simulated within a SwarmSAR system. The simulator developed in this chapter generates the radar data required for applying STAP processing.

Chapter 4 presents the implementation of the conventional STAP algorithm, where the inverse of the interference covariance matrix is estimated using an orthogonal projection onto the clutter subspace. The chapter analyzes the effectiveness of this estimation approach. Additionally, the chapter evaluates the performance of the conventional STAP algorithm applied to a SwarmSAR system consisting of three satellites with a single transmitter, across three different satellite baselines: 25 meters, 50 meters, and 100 meters.

Chapter 5 presents a modified approach to the conventional STAP algorithm, aimed at improving its effectiveness in SwarmSAR systems. The motivation behind this approach was to enhance its effectiveness when the SwarmSAR system operates with baselines that are feasible from an engineering perspective— at least a few hundred meters. The chapter outlines the complete methodology for implementing this approach and includes a performance evaluation based on a system composed of three satellites with a single transmitter. The evaluation considers two baseline configurations: a uniform spacing of 450 meters, and a non-uniform arrangement with 450 meters between the first and second satellites, and 700 meters between the second and third. Finally, Chapter 6 concludes the thesis by addressing the research questions based on the work presented and by outlining potential directions for future research.

# Theoretical background

This chapter covers the basic radar theory and background information necessary to understand the rest of this work. It starts with a brief overview of radar fundamentals, including the methods for measuring range and velocity measurements. The principles of pulse compression, motion compensation and digital beamforming signal processing techniques are then introduced, along with the multistatic radar concept, which is used in the following chapters. The end of the section explains the concept of STAP for detection of moving targets.

## 2.1. Radar Concepts

#### 2.1.1. Range Measurements

A radar, standing for Radio Detection and Ranging, is an electrical system that transmits radiofrequency electromagnetic waves toward a region of interest and receives and detects these waves when they are reflected from objects in that region. The small portion of the signal that is reflected back to the radar is captured by the antenna. A pulse radar transmits short pulses at a specific carrier frequency, followed by quiet periods during which it listens for echoes returning from targets. From these echoes, the target range is determined by measuring the time it takes for the electromagnetic wave to travel to the target and back at the speed of light c. The following equation shows the relationship between the target range R and the time delay  $\tau_d$  of a received signal coming from a target.

$$R = \frac{c\tau_d}{2} \tag{2.1}$$

The pulses are transmitted at a rate called the Pulse Repetition Frequency (PRF), which is the inverse of the time interval between the start of each pulse, known as the Pulse Repetition Interval (PRI). This parameter defines the maximum unambiguous range, as echoes from more distant targets arrive after the next pulse is transmitted, causing uncertainty about which transmitted pulse correspond to the received echo. The maximum unambiguos  $R_{max}$  range can be written as:

$$R_{max} = \frac{c \cdot PRI}{2} = \frac{c}{2 \cdot PRF} \tag{2.2}$$

Therefore, long-range radars have PRF in the order of kHz, while short-to-medium range radars have PRF in the order of MHz, resulting in maximum unambiguous ranges of a hundred kilometers and a hundred meters, respectively. An illustration of the pulses transmitted by a radar with a range ambiguity situation is shown in Fig.2.1, where the tall rectangles represent the transmitted pulses and the shorter ones represent the received echoes. It shows that a second target signal from the first transmitted pulse is received during the listening time of the second pulse. This second echo's measured time delay will be much shorter than the actual one, resulting in a significantly different range measurement.

2.1. Radar Concepts

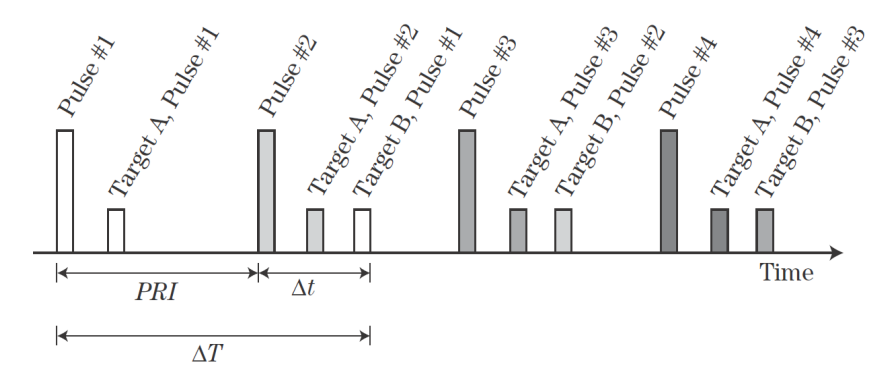


Figure 2.1: Pulse radar range ambiguity.  $\Delta T$  represents the actual time delay of the echo from target B while  $\Delta t$  shows the time delay that the radar measures [59]

Another important parameter in radar systems for range measurements is range resolution. This refers to the ability to distinguish between two or more closely spaced targets. For accurate range measurements, two closely spaced targets can be resolved if the time delay between their echoes is greater than the pulse duration. Therefore, shorter pulse lengths result in better range resolution. The pulse length  $\tau_p$  can be approximated using the bandwidth B as  $\tau_p \approx 1/B$ , and the range resolution becomes

$$\Delta R = \frac{c\tau_p}{2} = \frac{c}{2B} \tag{2.3}$$

In addition, the range uncertainty or accuracy is dependent on the time at which we consider that the pulse has arrived. A threshold is set on the pulse's leading edge. If the measured pulse crosses this threshold too soon due to noise, it results in a range error. This error is influenced by the signal-to-noise ratio (SNR) and the bandwidth as

$$\delta R \approx \frac{c}{2B\sqrt{2\cdot SNR}} = \frac{\Delta R}{\sqrt{2\cdot SNR}}$$
 (2.4)

#### 2.1.2. Velocity Measurements

Target radial velocity can also be measured with radar reflections. The radial velocity is the projection of full velocity on the line of sight of the radar. The simplest way to measure it is by determining the target range displacement over consecutive pulses, using only the amplitude information. However, this method has limited accuracy, as demonstrated eq.2.3 and eq.2.4 for range measurements. For this reason, there are more complex methods that involve the ability to measure the phase of the received signals, which requires the transmitter and receiver to be phase-locked. This systems are known as coherent and they can reveal small differences in the echo frequency which is necessary to make use of the Doppler shift. The Doppler effect is the change in frequency of the returned signal caused by the relative motion of a target. This frequency shift occurs because the signal travels a longer or shorter distance and it can be written as

$$f_D = -\frac{2v_r}{\lambda} = -\frac{2v\cos\theta}{\lambda} \tag{2.5}$$

where  $\lambda$  is the wavelength,  $v_r$  is the radial component of the target velocity towards the radar, v is the target velocity and  $\theta$  is the angle between the line of sight of the radar and the target's longitudinal axis. The convention is that a positive Doppler shift indicates the target is approaching the radar, corresponding to a negative velocity, and vice versa. For this expression to be fulfilled  $v_{target} \ll c$ . Additionally, note that the Doppler shift is zero for a target moving perfectly along the radar's view angle. One approach to estimate the target velocity is to measure the frequency difference between the incident and reflected wave. However, the frequency resolution, and consequently the velocity resolution, is limited by the transmitted pulse length. A longer pulse length is required for lower resolution as  $\tau_p \approx 1/\Delta f$ ,

but this negatively impacts the range resolution as seen in eq.2.3. For this reason, it is not possible to achieve both precise range and velocity resolution with this approach. A solution to this problem is to measure the phase shift over a sequence of  $N_{burst}$  pulses within a fixed period, known as the coherent integration time  $T_i$  (CPI). The velocity resolution depends on the integration times as

$$\Delta v_r = \frac{\lambda \Delta f_D}{2} = \frac{\lambda}{2T_i} = \frac{\lambda}{2N_{burst} \cdot PRI}$$
 (2.6)

The frequency shift can then be calculated by a Fast Fourier Transform (FFT) over consecutive received pulses (slow time) for every range bin (fast time). A longer coherent processing interval (CPI) improves speed resolution. However, if the CPI is too long, the target will experience range migration, causing it to appear elongated on a range vs. velocity plot [1]. Unlike using a single pulse to estimate velocity, this approach considers the phase (and time) to change in discrete steps. Each step corresponds to a new received pulse within the CPI, and the time difference between these steps depends on the PRF, which is equal to the sampling frequency. According to the Nyquist sampling theorem, the maximum unambiguous Doppler shift  $f_D^{max}$  is then  $\pm PRF/2$  which corresponds to the following maximum unambiguous velocity  $v_r^{max}$ :

$$v_r^{max} = \pm \frac{\lambda f_D^{max}}{2} = \pm \frac{\lambda PRF}{4} \tag{2.7}$$

A larger velocity than  $v_r^{max}$  will cause a phase difference outside the interval  $\Delta \phi < |\pi|$  and the measured velocity will experience a Doppler ambiguity folding and it will not correspond the actual target velocity. For instance, if the true target velocity is twice the maximum unambiguous velocity, the Doppler shift warps around in such a way that the radar measures zero velocity. Regarding the velocity accuracy, it is has a similar expression than eq.2.4, with a better accuracy for a greater SNR

$$\delta v_r \approx \frac{\Delta v_r}{\sqrt{2 \cdot SNR}} = \frac{\lambda}{2T_i \sqrt{2 \cdot SNR}}$$
 (2.8)

## 2.2. Pulse Compression

In a radar system, a filter is applied to the received signal to maximize the SNR at the time corresponding to the target's delay. This filter is derived from the transmit waveform and is known as a matched filter. It is implemented by correlating the received signal with a time-reversed copy of the transmitted waveform, and can thus be expressed as [59]:

$$h(t) = s^*(\tau_p - t) {(2.9)}$$

where  $\tau_p$  is the duration of the signal. Note that matched filter is an optimal filter for white noise case. For colored noise, the optimal filter is a combination of a whitening filter followed by a matched filter [59]. After the implementation of this filter, the SNR is maximized at the instant when the received signal is fully aligned with the filter. This is the moment when the entire signal has been received, and the matched filter output produces a peak. With an unmodulated waveform, such as simple rectangular pulse, the matched filter output produces a triangular peak. Here, the peak width, and consequently the range resolution, is limited by the pulse duration. A shorter pulse duration, resulting in a larger bandwidth, produces a sharper triangular peak improving range resolution. Conversely, a larger bandwidth increases noise, leading to a poorer SNR. To overcome the trade-off between range resolution and SNR, modulated waveforms are employed, introducing the concept of pulse compression. In modulated waveforms, the frequency varies with time, yielding a higher bandwidth for the same duration. The use of these waveforms, when used in conjunction with a matched filter, results in a receiver output with a concise energy concentration relative to the pulse duration. This results in a sharper peak, improving the range resolution as the bandwidth is increased (eq.2.3)), without compromising the SNR. Intuitively, this implies that the autocorrelation of the waveform should destructively interfere at all delays except zero. A measure of the of the improvement in range resolution of a modulated waveform versus that of an unmodulated waveform is known as the Pulse-Compression Ratio:

$$PCR = \frac{\Delta R_{pulse}}{\Delta R_{compressed}} = \frac{c\tau_p/2}{c/2B} = B\tau_p$$
 (2.10)

This is known as the time-bandwidth product. In addition to the enhanced range resolution, there is also an improvement in SNR, equal to the time-bandwidth product, due to the concentration of energy into a shorter time interval. A widely used example of a modulated waveform is the Linear Frequency Modulation (LFM) waveform, known as chirps, where the frequency increases or decreases linearly throughout the pulse duration. Figure 2.2 shows the matched filter output for a non-modulated waveform compared to a LFM waveform. Both waveforms have a duration of 20  $\mu$ s; however, the LFM waveform has a bandwidth of 20 MHz, while the non-modulated waveform has a bandwidth equal to the inverse of its duration. The improvement in range resolution when using the LFM waveform is clearly observable.

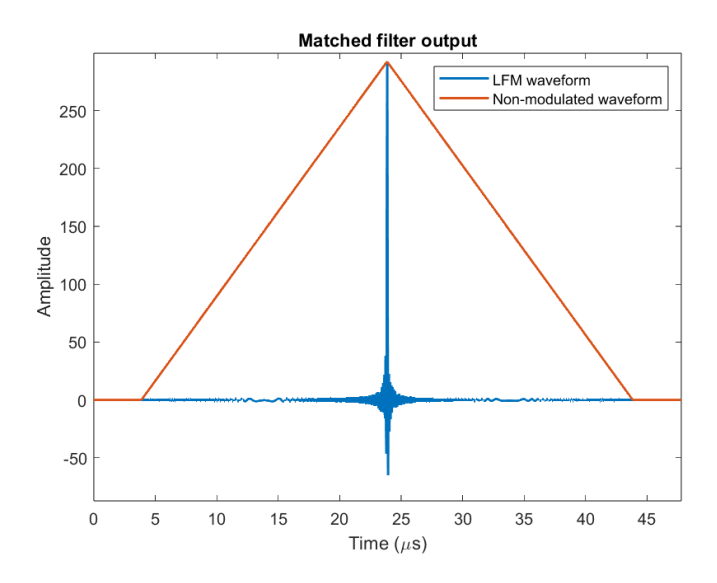


Figure 2.2: Matched Filter Output Comparison Between a Non-Modulated and an LFM Waveform

## 2.3. Azimuth Compression

As mentioned in section 2.1.2, a radar system typically determines the target's velocity by measuring the phase shift over a sequence of pulses within a fixed period known as CPI. The illumination time  $T_{ill}$  is the total time duration within the CPI during which a radar target is effectively illuminated by the radar. During this period, the target may shift to different range and velocity cells, resulting in an energy spread. A range cell migration (RCM) can occur when the target or radar platform has a sufficiently high velocity relative to the CPI, causing the target to travel a distance comparable to the range cell. Each range cell is defined by the sampling frequency, and usually each range cell represents a distance equal to the resolution  $\Delta R$ . The point target energy will be distributed over several range cells when  $RCM(t=T_{ill}/2)>\Delta R/2$ . Similarly, there are velocity cells that are equal to the velocity resolution given in eq.2.6. A spread in across the velocity cells can occur when a target is accelerating during the illumination time. Just like in RCM, this leads to a degradation of the scatterer's SNR, resulting in azimuth defocusing in the SAR image [1].

In the context of spaceborne radars in a SwarmSAR sytem, the high platform velocity and geometry cause ground reflections to spread across the velocity cells. This occurs because ground reflections experience apparent acceleration during the illumination time. To mitigate this spread, a compression can be performed over the velocity cells, functioning as a matched filter in the velocity domain. Since the measured velocity can be translated into an azimuth angle following eq.1.1, this can also be seen as an azimuth compression. Similar to the range domain, where compression is achieved by correlating the received signal with a time-reversed copy of the transmitted waveform (eq.2.9), compression in the azimuth domain involves convolving the signal with its reference function, which represents the

2.4. Multistatic Radars

expected response from a point target on the ground. Considering an elemental scatterer at range r(t), the azimuth signal reference signal can be modeled as [6]:

$$h_{az}(t) = exp(-j\frac{4\pi}{\lambda}r(-t)) \approx exp(-j\pi k_a t^2)$$
 (2.11)

where  $k_a=(-2v_p^2)/(\lambda r_0),\ v_p$  is the platform velocity and  $r_0$  is the minimum range at  $t_0$ . This equation can only be implemented when the target range as a function of time is known or can be estimated. Note that azimuth compression primarily focuses the energy in the velocity domain. To correct RCMC, more complex methods are required, such as the "Keystone Transform." Introduced several years ago, this technique aims to remove the linear range cell migration of moving target signals, regardless of their motion parameters [60].

## 2.4. Multistatic Radars

This section presents the theoretical background of multistatic radar systems, such as SwarmSAR, where transmitters and receivers are distributed across different locations. A bistatic radar utilizes two antennas at separate locations, one for transmission and one for reception, typically with the transmitter (TX) and receiver (RX) accompanying the antennas. A variation of this is the multistatic radar, which employs multiple antennas at different locations—one for transmission and multiple for reception, or vice versa. Similarly, transmitters or receivers can accompany these antennas. In contrast with the monostatic case, the receiving system is entirely passive, making it undetectable and immune to deliberate directional interference known as jamming. Additionally, multistatic radar provides a larger effective aperture due to the spatially separated receivers, which can enhance angle and position accuracy. The larger aperture also provides multiple perspectives, as the target is observed from different angles by each receiver. This can enhance the target's RCS, as a target that reflects poorly in one direction may reflect strongly in another, thereby increasing the overall detection probability [61]. A large separation also reduces TX-RX direct coupling, enhancing the ability to measure weak signals. Regarding the radar equation for a bistatic system, which shows the radar's capability to detect targets, it can be written as

$$P_{RX} = \frac{P_{TX}G_{TX}G_{RX}\lambda^2\sigma_{bist}}{(4\pi)^3R_1^2R_2^2L_{sys}}$$
 (2.12)

where  $P_{TX}$  is the transmitted power,  $G_{TX}$  is the transmitter antenna gain,  $G_{RX}$  is the receiver antenna gain,  $\sigma_{bist}$  is the bistatic RCS,  $L_{sys}$  are the system losses,  $R_1$  is the range from the transmitter to the target and  $R_2$  is the range from the target to the receiver. This equation can be applied in a multistatic radar system for each TX-RX pair. Each of these pairs create a virtual radar node, which is a conceptual point where the TX and RX are considered to be co-located for analytical purposes. This point in space represents the monostatic geometric equivalent of the bistatic system, often used to simplify the analysis or interpretation of the bistatic measurements such as bistatic range. It corresponds to the midpoint along the line connecting the each TX-RX pair. It is accurate only under the assumption of far-field conditions, which hold when the target is far compared to the TX-RX distance, and the assumption of a small bistatic angle, which holds when the path geometry approximates a straight line. This is usually the case in spaceborne multistatic systems such as SwarmSAR.

## 2.5. Digital Beamforming

Digital beamforming is a signal processing technique used to steer beams electronically with an array of sensors or antennas. It is employed to achieve angular resolution and can be described as the multiplication of the signal from each antenna element by a specific weight vector, as detailed by [62]

$$y(t) = \mathbf{w}^T \mathbf{x}(t) \tag{2.13}$$

where the operator  $(\cdot)^T$  indicates the transpose, y(t) output signal at time t,  $\mathbf{w}$  is the  $N \times 1$  vector of weights,  $\mathbf{x}(t)$  is the  $N \times 1$  spatial vector representing the received signal at each antenna at a given

time instant and N is the number of antennas. From the last equation, it is evident that beamforming involves a linear combination of the antenna outputs. For a narrowband source s(t), where the time delays are smaller than the inverse bandwidth, the received baseband signal  $\mathbf{x}(t)$  in a uniform linear array (with equal antennas and uniform spacing) can be modeled as

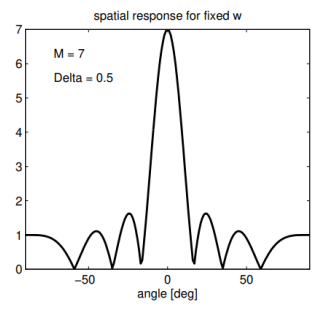
$$\mathbf{x}(t) = \begin{bmatrix} 1 \\ e^{j2\pi \frac{d}{\lambda}sin(\theta)} \\ \vdots \\ e^{j2\pi(N-1)\frac{d}{\lambda}sin(\theta)} \end{bmatrix} a_0(\theta)s(t) = \mathbf{a}(\theta)s(t)$$
(2.14)

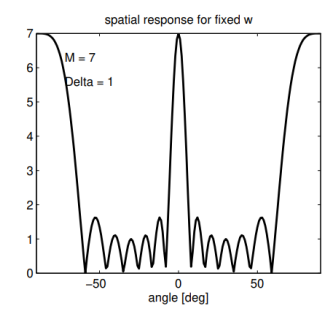
where  $a_0(\theta)$  is the direction-dependent antenna response of a single element of the array and  $\mathbf{a}(\theta)$  is called the array response vector. By substituting the expression for  $\mathbf{x}(t)$  into the equation eq.2.13 and computing the output power for a single unit-power source, we obtain

$$P_y(\theta) = |y(t)^2| = |\mathbf{w}^H \mathbf{a}(\theta)|^2$$
(2.15)

By choosing  $\mathbf{w}(\theta) = \mathbf{a}(\theta)$ , one can achieve a maximum power response for signals arriving from the direction corresponding to angle  $\theta$ . This occurs because the phase shift induced in the array by a signal s(t) arriving at angle  $\theta$  is effectively counteracted by the phase shift introduced by the beamforming weight vector  $\mathbf{w}$ . This represents the simplest form of beamforming and can be employed for direction finding by varying the angle  $\theta$  in the weight vector  $\mathbf{w}$ . For instance, if there are two sources with distinct angles of arrival, applying this weight vector will result in an output power pattern exhibiting two peaks at the corresponding angles. However, in practical scenarios, the presence of noise and interference requires the use of more advanced beamforming techniques. These methods adjust both the amplitude and phase of the weight coefficients to maximize the SNR or to suppress interference from undesired directions.

In addition, the use of an antenna array is equivalent to a discrete sampling in the spatial domain. Just as temporal sampling of received pulses (used to estimate target velocity) can lead to an ambiguous velocity measurement, as discussed in section 2.1.2 , an spatial ambiguity occurs when the phase difference between consecutive elements is outside the interval  $\Delta\phi<|\pi|$ . This occurs for certain angles of arrival  $\theta$  when the antenna spacing exceeds  $\lambda/2$ , since the phase difference between elements in  $\mathbf{a}(\theta)$  is given by  $2\pi\sin(\theta)d/\lambda$ . As a result, an ambiguity arises in estimating the angle of arrival of the received signal. In the spatial response for a fixed  $\mathbf{w}$ , it translates into grating lobes, which are unwanted secondary lobes in the radiation pattern of an antenna array. Fig.2.3 shows the grating lobes produced in an antenna array when the spacing is larger than  $\lambda$ . More grating lobes appear when the spacing is greater. Note that the lobes become narrower with larger spacing, which corresponds to increased directivity due to the extended overall antenna aperture. The increased directivity can also be seen as a better resolution in the estimation of the angle of arrival.





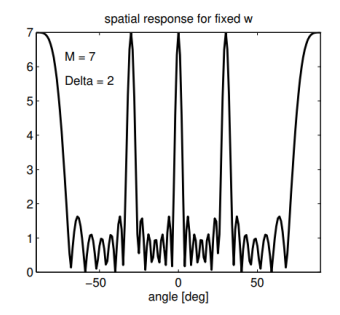


Figure 2.3: Grating lobes in spatial response for a fixed weight vector, for 3 different arrays of 7 elements and normalized spacing  $\Delta=d/\lambda$  equal to 0.5, 1 and 2 [62]

2.6. STAP 16

### 2.6. STAP

Space-Time Adaptive Processing (STAP) is a method that cancels stationary clutter while providing maximal gain on target used for GMTI. This section derives the beamformer expression for STAP and the traditional approach to implement it in a multichannel system. Consider a system with a M-element uniform linear array (ULA) with distance between elements d. In a CPI the radar transmits a sequence of K pulses. The received data at each range cell can be vectorized by stacking each succeeding temporal samples K with the space samples N in a  $KN \times 1$  vector [4].

$$\mathbf{x} = \alpha \mathbf{v}(\theta, f_t) + \mathbf{q} \tag{2.16}$$

where  ${\bf q}$  is the space-time vector of the clutter and noise which is considered to be independent from the reflections of the target. On the other hand,  ${\bf v}$  is the return echo from the moving signal which has a certain Doppler frequency  $f_t$ , angle of arrival  $\theta$  and a reflectivity equal to the complex amplitude  $\alpha$ . The complete derivation of the target Doppler frequency  $f_t$  induced by a moving object in spaceborne radar is presented in [32]. As a final result, and under the assumption that the CPI is sufficiently short to neglect the quadratic term in the range variation due to platform motion (a valid approximation in STAP [6]) we obtain the following expression for the target Doppler frequency

$$f_t \approx -\frac{2}{\lambda}(v_t - v_p cos(\theta)) = -\frac{2}{\lambda}(v_t - v_{rp})$$
(2.17)

where  $v_t$  is target radial velocity and  $v_{rp}$  is the platform radial velocity. It is important to note that this value is assumed to remain constant throughout the entire CPI, which is a valid approximation for the  $f_t$  after SAR azimuth compression when the CPI is short. Taking this into account, the  $KN \times 1$  space-time vector  $\mathbf{v}$  is given by

$$\mathbf{v}(\theta, f_t) = \mathbf{b}(f_t) \otimes \mathbf{a}(\theta) \tag{2.18}$$

where

$$\mathbf{a}(\theta) = \begin{bmatrix} 1 & e^{j\frac{2\pi d}{\lambda}cos(\theta)} & \dots & e^{j(M-1)\frac{2\pi d}{\lambda}cos(\theta)} \end{bmatrix}^T$$
 (2.19)

$$\mathbf{b}(f_t) = \begin{bmatrix} 1 & e^{j2\pi f_t T_s} & \dots & e^{j(M-1)2\pi f_t T_s} \end{bmatrix}^T$$
 (2.20)

where  $T_s$  is the PRI of the radar. Note that  $\mathbf{b}(f)$  is the  $K \times 1$  temporal steering vector and  $\mathbf{a}(\theta)$  is the spatial steering vector  $N \times 1$  of a ULA. Note that assuming a finite number of clutter patches  $N_c$ , one can use  $a(\phi)$  and  $b(f_c)$  (where  $f_c$  is the Doppler frequency of the clutter) to write the space-time vector of the clutter as

$$\mathbf{y}_c = \sum_{i=1}^{N_c} \rho_i \mathbf{v}_c(\theta_i, f_{c,i}) = \sum_{i=1}^{N_c} \rho_i \mathbf{v}_c(\theta_i)$$
(2.21)

where  $\mathbf{v}_c$  is the same one as in eq.2.18 but now it only depends on  $\theta$  because we can obtain the Doppler frequency of the clutter  $f_c$  just with this angle (eq.1.1). The space-time processor linearly combines the elements of the space-time snapshot  $\mathbf{x}$  of every range cell by applying a weight vector . As result at the output of the space-time processor a scalar is obtained for every range cell

$$\mathbf{y} = \mathbf{w}^H \mathbf{x} \tag{2.22}$$

where  $(\cdot)^H$  denotes the conjugate transposition and  $\mathbf{w}$  is  $KN \times 1$  the weight vector. The objective of STAP is to design a weight vector to maximize the SINR. By modeling the received space-time signal as described in Equation 2.16, the Signal to Clutter plus Noise Ratio (SCNR) after the implementation of the weight vector can be expressed as follows

$$SCNR(\mathbf{w}) = \frac{|\alpha|^2 |\mathbf{w}^H \mathbf{v}(\theta, f_t)|^2}{\mathbf{w}^H \mathbf{R}_O \mathbf{w}}$$
(2.23)

2.7. Summary 17

where  $\alpha$  is the reflectivity. The optimal weight vector that maximizes the output SCNR in eq.2.23 is given by the following expression [6]

$$\mathbf{w}_{opt} = \mathbf{R}_O^{-1} \mathbf{v}(\theta, f_t) \tag{2.24}$$

where  $\mathbf{R}_Q$  is the interference covariance matrix of dimension  $KN \times KN$ . Note that this corresponds to the expression of the matched filter. This space-time beamformer is designed to enhance the response in the direction of the target signal while suppressing clutter and noise by effectively whitening the interference. It is expected to perform well when the target steering vector is not aligned with the clutter subspace. The  $\mathbf{R}_Q$  is equal to

$$\mathbf{R}_O = \mathbf{R}_C + \mathbf{R}_N + \mathbf{R}_J \tag{2.25}$$

where  $\mathbf{R}_C, \mathbf{R}_N$  and  $\mathbf{R}_J$  denote the covariance matrices of the clutter, white noise, and jamming interference, respectively. In most cases, ground clutter is the dominant source of interference, allowing the interference covariance matrix to be approximated by  $\mathbf{R}_C$ . If we assume the clutter is stationary, homogeneous and spatially white (i.e  $E[|\rho_i \rho_k^*|] = \sigma_{c,i}^2 \delta(i-k)$ ) the clutter covariance matrix can be modeled as [4].

$$\mathbf{R}_C = E[\mathbf{y}_c \mathbf{y}_c^H] = \sum_{i=1}^{N_c} \sigma_c^2(\theta_i) \mathbf{v}_c(\theta_i) \mathbf{v}_c^H(\theta_i)$$
(2.26)

where  $\sigma_c^2(\theta)$  is the clutter intensity, and  $\mathbf{v}_c(\theta)$  is the steering vector of a single clutter patch. In practice  $\mathbf{R}_Q$  is not known and therefore it is necessary to estimate them from the received data. The method used in this project for this estimation will be analyzed in Chapter 4 In addition, the direct computation of  $\mathbf{R}_Q^{-1}$  is not only expensive but also requires enough spatial-time vectors used in the estimation of  $\mathbf{R}_Q$ , each corresponding to a different range cell. Regarding the optimal output SCNR after STAP weight vector implementation, it is equal to the following expression

$$SCNR_{opt} = |\alpha|^2 \mathbf{v}(\theta, f_t)^H \mathbf{R}_Q^{-1} \mathbf{v}(\theta, f_t)$$
(2.27)

## 2.7. Summary

In conclusion, this chapter provides the essential background needed to understand how Radars obtain the range and velocity information from scatterers. The principle of beamforming is also introduced, as it is a key concept in STAP processing. Similarly, the concept of multistatic radar is important for the scenario analyzed in this project, which involves multiple satellites, each with a single antenna. This information is essential for understanding both how the received signal is generated in the simulator and how the STAP algorithm is implemented.

# Simulation Setup

This chapter explores the methodology used to simulate satellite-received ground reflections from a SwarmSAR system. A simulator is essential for generating synthetic data required to implement the STAP algorithm. Since, to the best of our knowledge, no SwarmSAR system has been launched and thus no real measurements are available, it is necessary to model and simulate the system ourselves. First, the system geometry is introduced. Next, the modeling of the channel response from the rough surface is described, along with the necessary steps to reconstruct the complete received signal at each satellite. Finally, we analyze the velocity measurements obtained using multiple received pulses from the rough surface, while applying azimuth compression, and we validate the results through Doppler processing.

## 3.1. System Geometry and Parameters

This section presents the geometric configuration of the problem under study, along with the relevant satellite radar system parameters . It involves a single transmitter and multiple receivers, all configured as side-looking radars mounted on moving platforms. These platforms simulate satellites, characterized by their high velocity and altitude. During the integration time, all sensors illuminate the same ground area, referred to as the footprint. This footprint is modeled as a square grid, with each side equal in length to the swath width. Fig.3.1 shows the complete geometry. The slant range illustrates the direct line-of-sight distance to a point of the ground and the look angle is defined as the angle between the vertical direction (nadir) and the slant range to the nearest point within the swath width.

For the system parameters, this report follows the configuration described in [63], which represents a potential setup for a SwarmSAR system. The transmitted radar signal is a LFM waveform (or chirp) of 20 MHz with a carrier frequency in S-Band. The PRF is chosen to ensure a sufficiently large maximum slant range, allowing full coverage of the simulated ground grid. Although the maximum unambiguous range corresponding to this PRF is much shorter than the slant ranges within the grid, this is not an issue, as the region preceding the grid is assumed to be empty. A complete list of all system parameters is presented in Table 3.1.

## 3.2. Rough surface response

This section discusses the modeling of the frequency response of the simulated rough surface. Electromagnetic scattering from a rough surface is analyzed using a finite grid composed of equally sized cells. Each grid cell backscatter coefficient is associated with a Gaussian random distribution, as it models a localized region containing numerous randomly distributed elemental scatterers. When a large number of independent, small-scale scatterers (such as those found on a rough surface that give rise to the so-called speckle effect in SAR images [1]) contribute to the scattered signal, the central limit theorem applies. As a result, radar echoes tend to follow a Gaussian distribution. It is well known that, in such cases, the magnitude of the resulting complex signal follows a Rayleigh distribution, while the phase is uniformly distributed.

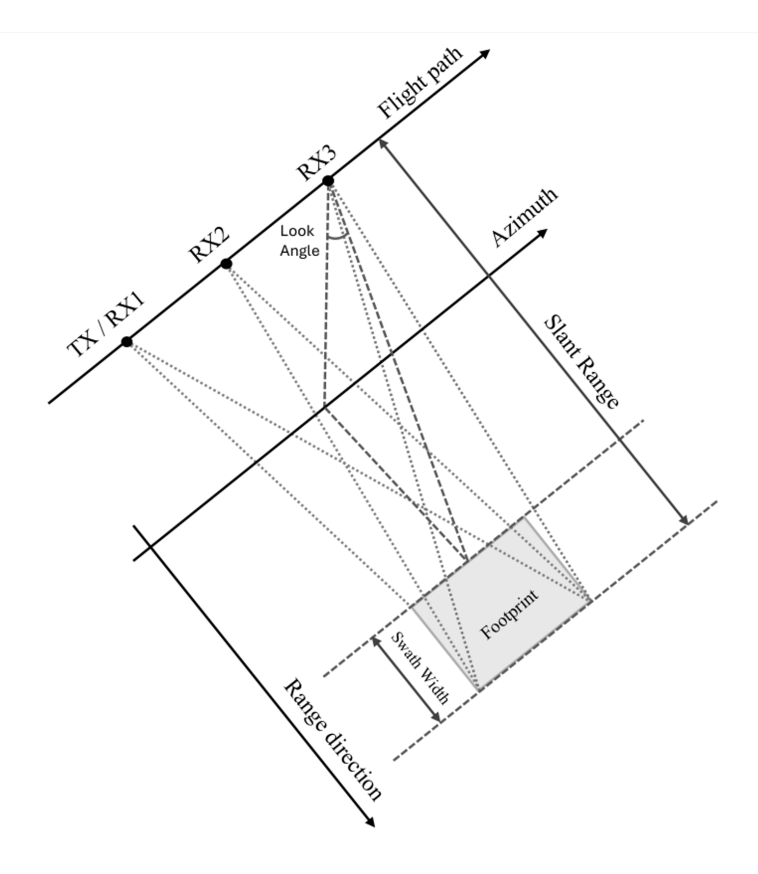


Figure 3.1: Geometry of the problem

<b>Geometry Parameters</b>	Value
Satellite Height	500 km
Satellite Velocity	7000 m/s
Look Angle (near range)	22°
Swath Width	5 km
Number of Grid Cells	10000

Radar Parameters	Value
Central Frequency	3200 MHz
PRF	8150 Hz
Bandwidth	20 MHz
$\Delta R$	7.5 m
Average Transmitted Power	40 W
Antenna Gain	36 dBi

Table 3.1: System parameters

Additionally, each of these grid cells is modeled as a point scatterer, positioned at the center of the cell. This approach is justified, as in the space-time model of STAP, each range-Doppler cell (RDC) is typically treated as a point scatterer. A point scatterer introduces a phase shift proportional to the round-trip delay and is scaled in magnitude according to its RCS. For accurate modeling, the mean RCS magnitude should vary with the incidence angle, with higher values occurring at lower incidence angles. This is because, when the radar looks more directly downward, a greater portion of the transmitted energy is reflected back toward the radar. To estimate the mean of the Rayleigh distribution, which the RCS follows because it represents the magnitude of a complex Gaussian radar echo, we use a database developed by Ulaby et al. [64] which provides different models for the backscattering coefficient  $\sigma_{0_i}$  depending on frequency, polarization, and terrain type. Fig, 3.2 shows one of this models for short vegetation and HH polarization.

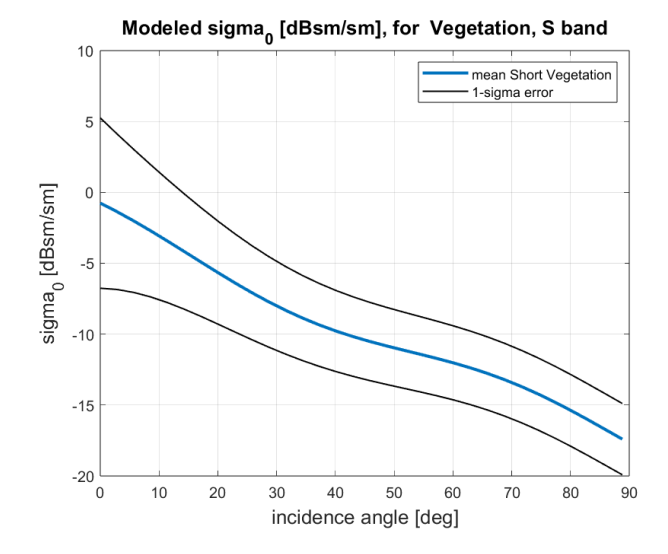


Figure 3.2: Backscatter coefficient with respect to the incidence angle for short grass and HH polarization

Moreover, the overall frequency response of all the N grid cells can be represented as the sum of the individual frequency responses of each grid cell i

$$H(f) = \sum_{i=1}^{N} \sqrt{A\sigma_{0_i}} e^{-j2\pi \frac{(R_{TX_i} + R_{RX_i})}{c} f}$$
(3.1)

where  $\sigma_{0_i}$  is the normalized RCS or backscatter coefficient, A is the area of the rectangular cells, c is a constant corresponding to the speed of light,  $R_{TX_i}$  is the distance from the transmitter to the grid cell i,  $R_{RX_i}$  is the distance from the receiver to the grid cell i. Note that the RCS of each range cell is  $\sigma_i = A\sigma_{0_i}$  and the total round-trip delay is  $(R_{TX_i} + R_{RX_i})/c$ .

Since the transmitted signal in SwarmSAR is not narrowband and is instead an S-band chirp of 20 MHz bandwidth, each transmitted frequency component must correspond to a distinct frequency response, H(f). This occurs because the phase shift introduced by the propagation delay varies with frequency, even though the RCS is assumed to be frequency-independent. To analyze the frequency response across the transmitted frequency range, it is necessary to define a frequency step to discretize the interval of transmitted frequencies. To ensure adequate sampling and avoid aliasing, the inverse of the frequency step  $\Delta f$  must be smaller than the delay introduced by the dimensions of the grid  $\tau_{max}$ . Hence, the condition

$$\frac{1}{\Delta f} > \tau_{max} \tag{3.2}$$

This is because the inverse of the frequency step determines the maximum unambiguous time window, and it has to be long enough to capture the full delay spread. To obtain the total spectrum of ground reflections within the transmitted signal band, the frequency response H(f) is computed repeatedly at intervals of  $\Delta f$ . Note that the radial distances  $R_{TX_i}$  and  $R_{RX_i}$  need to be computed only once, as frequency is the only parameter that varies in each iteration.

Fig.3.3 shows the flowchart of the computation of the frequency response of the complete grid for all the frequencies in the band. We define a grid and compute its spectrum for a given frequency by calculating the backscattering coefficient and phase delays, using Equation 3.1. This process is repeated for each frequency in the spectrum, with a frequency step defined in Equation 3.2.

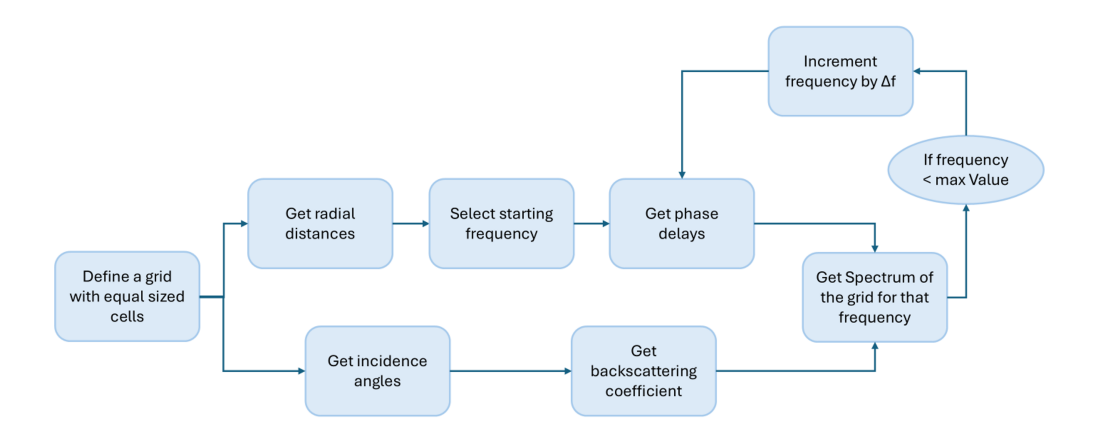


Figure 3.3: Flowchart of calculation of frequency response of the grid

In addition, Fig. 3.4 shows the normalized impulse response of the ground reflections for the grid parameters of Table 3.1. The time axis in the figure has been converted to range using eq.2.1. The width of the impulse response corresponds to the the slant range measurements of the grid. The shape of the pulse is influenced by the random Gaussian-distributed RCS values of the grid cells, as well as by the varying number of grid cells contributing to each slant range bin. Note that the width of each range bin is determined by the sampling frequency along the fast time axis.

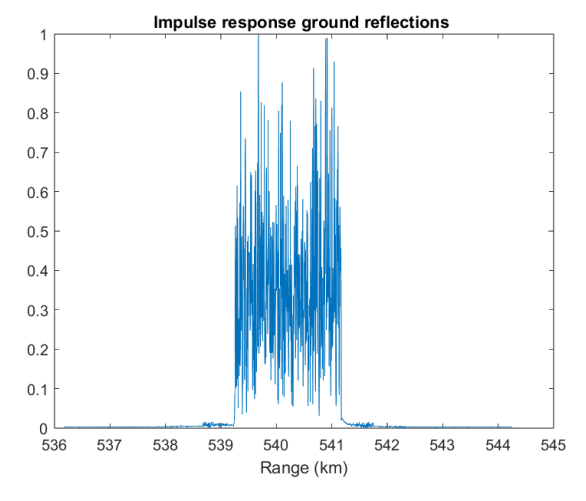


Figure 3.4: Impulse response of ground reflections from a grid with Table 3.1 parameters

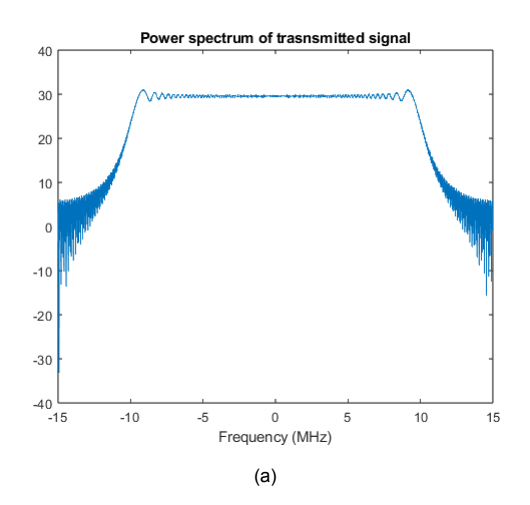
## 3.3. Received signal

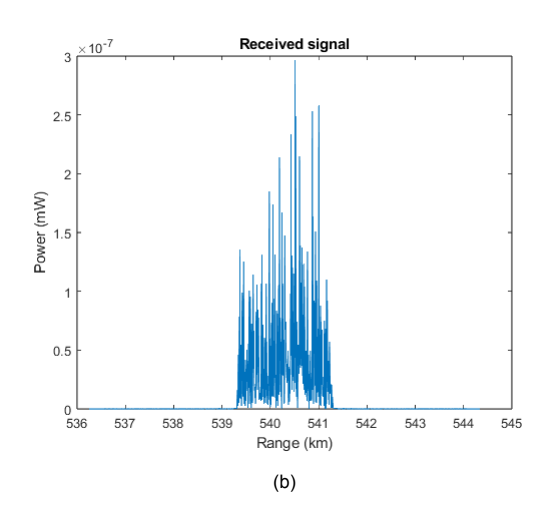
Once we compute the channel's frequency response across all frequencies present in the transmitted signal, the received signal can be obtained by convolving the transmitted signal with the channel. To simplify the computation, this convolution is performed in the frequency domain, where it becomes a straightforward multiplication. For this approach to be valid, both the transmitted signal and the channel response must be centered around zero and span the same frequency interval. The chosen sampling frequency,  $f_s$ , is 30 MHz. Given that the signal occupies a 20 MHz bandwidth and is complex-valued, this sampling rate satisfies the Nyquist criterion. For complex signals, the Nyquist rate equals the signal bandwidth, as both the real and imaginary components are sampled separately. Figure 3.5 shows the power spectrum of the transmitted signal. As observed, there is no aliasing, and the essential information of the signal is fully captured.

Fig. 3.5 illustrates the transmitted signal. After computing the convolution of the transmitted signal with the channel response, we perform range compression using a time-delayed replica of the transmitted waveform. The time delay represents the round-trip duration required for the transmitted wave to travel from the TX satellite to the RX satellite and back. Section 2.2 explains the theoretical background of this process. Range compression enhances the range resolution, achieving the value listed in Table 3.1, and provides a gain equivalent to the time-bandwidth product. As the final step, we apply the radar range equation (Equation 2.12) to calculate the actual received power at the satellite. Since the transmitter and receiver use the same antenna, they share identical gain values. The range values correspond to the measured slant range, and it is also included an additional intrinsic gain due to range compression, equal to the time-bandwidth product. In addition, we consider the system losses to be equal to 3 dB. Table 3.1 lists the antenna gain and transmitted power values used. In summary, the steps we follow to derive the final received signal are as follows:

- 1. Get ground frequency response
- 2. Convolve with transmitted signal
- 3. Implement range compression
- 4. Apply Radar range equation

Fig.3.5 shows the received signal after all these steps. Above, we discussed how to obtain the received signal from the grid that simulates the rough surface. In contrast, the signal from a target is modeled as originating from a single point scatterer with a specific velocity, unlike the static point scatterers representing the ground. Consequently, the target signal is modeled as the transmitted waveform with a phase shift corresponding to the round-trip delay and scaled in magnitude according to the target's RCS. This target signal can be added to the signal received from the rough surface before applying range compression and the radar range equation to the combined signal.





**Figure 3.5:** Transmitted chirp with 20 MHz of bandwidth (a) and power of received signal for each range cell after range compression and implementation of radar range equation (b)

## 3.4. Doppler processing

This section focuses on analyzing and validating the results obtained using the selected models for the received signal and channel response, discussed in the previous sections. It studies the monostatic case, where only a single satellite is employed. To achieve this, we aim to measure the velocity induced in ground reflections due to the platform's motion. This is done by integrating several received pulses to enable an accurate velocity estimation. The detailed procedure is described in Section 2.1.2. The core idea involves estimating velocity by measuring the phase shift across consecutive pulses which is done through the FFT. This step is performed after applying range compression using a time-delayed replica of the transmitted signal as explained in section 3.3. This approach results in a set of velocity cells, each representing a distinct measured velocity, with a width determined by the velocity resolution and

inversely proportional to the coherent processing interval (CPI). Using a total of 512 pulses for Doppler processing and the PRF specified in Table 3.1, this corresponds to a coherent processing interval (CPI) of 62.8 milliseconds, and thus a velocity cell width (or resolution) of 0.75 meters per second. This CPI will be used for the rest of the project.

Even with this short CPI, the velocity measurements for each scatterer are expected to show a spread across the velocity cells. This is due to the platform's high motion (7000 km/s), as each scatterer undergoes significant acceleration during the CPI. This occurs because the viewing angle changes continuously throughout the CPI, and as shown in eq.1.1, each viewing angle (which is the angle between the direction of flight and the line of sight) corresponds to a different Doppler frequency, and therefore to a different apparent velocity. In particular, the ground scatterers located in the broadside direction of a side-looking radar (i.e., perpendicular to the platform's motion) are the ones that yield zero velocity, since the viewing angle in this case is 90°.

Considering a radar mounted on a platform traveling at 7000 m/s at an altitude of 500 km, and using the parameters listed in Table 3.1, we can simulate as a starting point the returns over the entire CPI from a few point scatterers, whose RCS follows a Gaussian distribution as described in Section 3.2. Once the received pulses are simulated, including range compression, we perform an FFT over the consecutive pulses (slow time) for each range cell, resulting in the range-Doppler plot shown in Fig. 3.6a. In this figure, we observe five point scatterers. The central scatterer is positioned such that, at the midpoint of the CPI, the line of sight from the moving platform is perpendicular to the flight direction, resulting in a measured radial velocity of 0 m/s.

The figure shows that, as expected, the scatterers exhibit energy spread across multiple velocity bins (approximately five, with each bin representing 0.75 m/s) due to the linear acceleration each one experiences during the CPI. On the other hand, no range cell migration is observed, since the CPI duration is not long enough to produce a slant range variation greater than the width of a range cell. Note that the range cell spacing is 5 meters, which is smaller than the range resolution, as the signal is sampled at a higher frequency than the system bandwidth.

To mitigate the velocity spread and enhance the SNR by concentrating the energy into a single Doppler bin, we apply azimuth compression with motion compensation as described in Section 2.3. Fig. 3.6b shows the points scatterers range-Doppler plot after the implementation of this technique. The reference ranges used for the compression correspond to the central scatterer, meaning that r(t) in Equation 2.11 takes on the values associated with this scatterer throughout the CPI. For this reason, its energy is now concentrated around the velocity bin corresponding to 0 m/s, resulting in an integration gain (relative to a single pulse) equal to the number of integrated pulses (512). In practice, due to imperfections in the system geometry and the presence of numerous scatterers in the environment, it is convenient to estimate the range r(t) of the point scatterer at each time instant t of the CPI using the following equation [1]

$$r(t) = r_0 + \frac{(vt)^2}{2r_0} \tag{3.3}$$

which is true for  $vt/r_0 \ll 1$  and where v is the platform velocity and  $r_0$  is the closest point of approach, which, without loss of generality, is assumed to occur at  $t=t_0=0$ . Regarding the phase history (or the velocity) of the rest of the scatterers, it does not align with the reference. As a result, these scatterers are not properly compensated during azimuth compression. Consequently, after compression, each of these scatterers exhibits a Doppler frequency offset, and therefore a relative velocity, with respect to the assumed reference. This velocity offset corresponds to the additional apparent velocity induced in a scatterer due to its angular deviation from the central scatterer.

Next, we simulate the received pulses over the 100×100 defined grid of point scatterers, with each scatterer's RCS following a Gaussian distribution. It is assumed that the RCS of each scatterer remains constant throughout the entire CPI. If, instead, the RCS were to vary randomly for each received pulse, the ground clutter would lack of correlation between pulses. As a result, the STAP algorithm would no longer function effectively. This will be further analyzed in the next chapter.

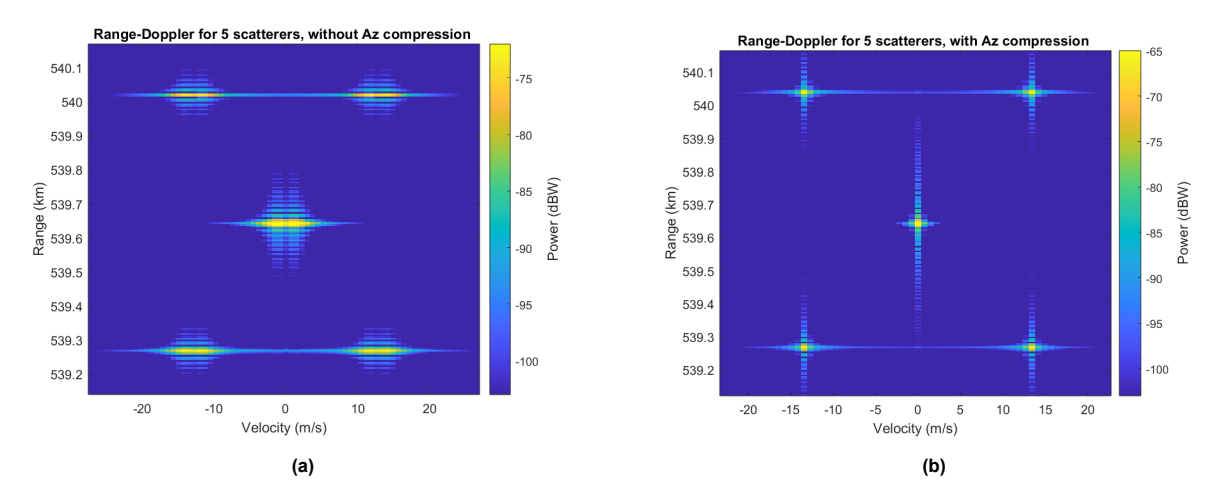


**Figure 3.6:** Range-Doppler plot of 5 scatterers with a central one centered around cero velocity: (a) without azimuth compression, (b) with azimuth compression

Fig.3.7a shows the range-Doppler plot of the reflections from the entire grid over the CPI. Due to the 5-meter slant range cell spacing, multiple grid cells may fall within the same range bin. The reflections from these cells are summed within each bin. However, this summation is not coherent, as the RCS values of the individual grid cells are randomly assigned. This implies that the average power level increases by a factor equal to the number of contributing cells. Moreover, the satellite's position is configured such that, at the midpoint of the CPI, the line of sight to the center of the grid is perpendicular to the flight direction. For this reason, the plot is symmetric around zero velocity. Additionally, this configuration causes the scatterers located at the edges of the grid to exhibit the highest measured velocities. This is because their line-of-sight angles form the largest deviation from the direction perpendicular to the flight path. For these point scatterers, the angular deviation is approximately 0.287°, which corresponds to the maximum measured velocity in the plot (approximately 35 m/s), thereby validating the expression given in eq.1.1. Due to the relationship between measured velocity and angle of arrival, the velocity axis in Fig.3.7a can also be interpreted in terms of the viewing angle.

For the azimuth compression, we now select the reference ranges corresponding to the center of the grid. As a result, after compression, the scatterers located within the range cell at the grid center have their energy concentrated in the velocity bin corresponding to zero velocity. This is because we are accurately compensating for all the velocity components experienced by the center of the grid throughout the CPI. Similar to the previously simulated scatterers, those located outside the center of the grid exhibit a relative velocity with respect to the assumed reference. On the other hand, after azimuth compression, the integration gain for each point scatterer, relative to a single received pulse, is no longer equal to the number of integrated pulses. This is because each range bin contains several grid cells that contribute incoherently, and none of them stands out significantly, which leads to a lower overall gain.

Moreover, note that we are compensating for the apparent velocity observed in static scatterers, which is caused by the motion of the platform. However, if a target scatterer has a certain radial velocity, there will be an additional residual velocity that remains uncompensated, beyond the one associated with the scatterer not being located at the center of the grid. Therefore, to accurately estimate a target's true radial velocity relative to the ground, it is also necessary to estimate its angle of arrival. This allows the subtraction of the velocity component caused by the target's position within the grid from the total measured velocity, in order to obtain the target's true radial velocity.

3.5. Summary 25

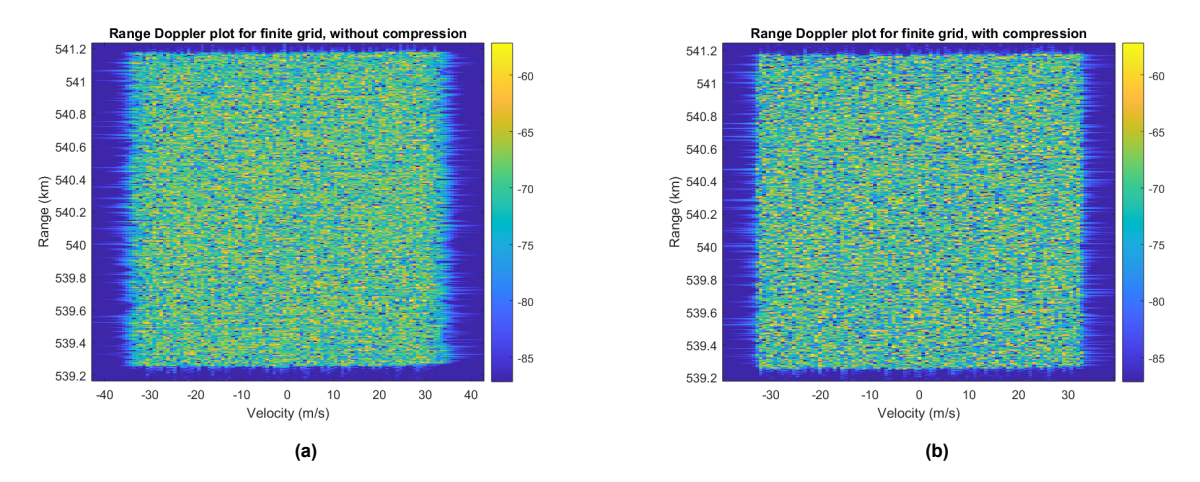


Figure 3.7: Range-Doppler plot of a the grid centered around cero velocity: (a) without azimuth compression, (b) with azimuth compression

## 3.5. Summary

In conclusion, this chapter outlines the simulation of received signals from a rough surface observed by a moving platform. The Doppler processing presented in the final section validates these simulations, which employ a finite grid approach to model ground reflections. Furthermore, the results confirm the effectiveness of the azimuth compression processing, which will serve as a preliminary step toward implementing the STAP algorithm.

# Classical STAP applied to SwarmSAR

This chapter presents the implementation of the classical STAP algorithm using simulated data, generated based on the expected geometry and system parameters outlined in the previous chapter and intended for use in the SwarmSAR system. The main objective is to evaluate the performance of the classical STAP algorithm in the context of a SwarmSAR satellite configuration. We begin by introducing the performance metrics. Following that, we describe the computation of the interference covariance matrix, which is essential for the algorithm's implementation. We then analyze the method employed to invert this nearly singular matrix, a critical step in the STAP process. Finally, we present the performance results of the classical STAP algorithm for three different baselines: 25 meters, 50 meters, and 100 meters.

#### 4.1. Metrics

To assess the performance of STAP across different scenarios, it is essential to define appropriate evaluation metrics. These metrics are based on the Signal-to-Clutter-and-Noise Ratio measured after applying the STAP weight vector to the received data, denoted as  $SCNR_{out}$ . Theoretically, after applying STAP, one expects to achieve the SCNR as defined in Equation 2.27. However, in practice, performance is often degraded due to non-idealities. In this project, these non-idealities arise from using an estimated interference covariance matrix instead of the true one. To capture the performance degradation, we define the following metric, that quantifies the loss by comparing the theoretical results with those obtained in practice [57].

$$SCNR_{Loss} = \frac{SCNR_{out}}{SCNR_{opt}} = \frac{SCNR_{out}}{|\alpha|^2 \mathbf{v}(\phi, f_t)^H \mathbf{R}_Q^{-1} \mathbf{v}(\phi, f_t)}$$
(4.1)

where  $\mathbf{R}_Q$  is the true interference covariance matrix,  $\alpha$  is the target reflectivity,  $\mathbf{v}(\phi,f_t)$  is the target matched space-time steering vector at a certain angle of arrival  $\phi$  and Doppler frequency  $f_t$ . In the ideal case, the  $SCNR_{Loss}$  equals the  $SCNR_{opt}$ , resulting in a value of 0 dB. Additionally, it is useful to evaluate the improvement in SCNR achieved through the implementation of STAP, highlighting the gain introduced by the processing itself. For this reason, this gain is usually measured with the Improvement Factor [6]

$$IF = \frac{SCNR_{out}}{SNR_{in}} \tag{4.2}$$

where  $SNR_{in}$  corresponds to the signal-to-noise ratio of a single received pulse, without any integration, after the matched filter has been applied and the gain equal to the time-bandwidth product has been obtained. We choose this moment to measure the SNR because the gain provided by the STAP algorithm does not depend on the pulse compression gain. In scenarios where the target is sufficiently

separated from the clutter subspace, the STAP algorithm should ideally eliminate the clutter, assuming a perfect estimate of the interference covariance matrix.

When the clutter is completely removed,  $SCNR_{out}$  becomes equal to  $SNR_{out}$ . Since the STAP weight vector cannot suppress thermal noise due to its uncorrelated nature across pulses, the difference between the measured SNR before and after applying STAP reflects the integration gain, which corresponds to the number of integrated pulses, combined with the array processing gain, which corresponds to the number of antennas. This means that the maximum value this metric can reach is equal to the sum of the integration gain and the array processing gain. This maximum is only achievable for combinations of target Doppler frequency and angle of arrival that are sufficiently separated from those associated with ground reflections, which correspond to clutter and follow the relationship described in Equation 1.1.

The required separation in the angle-Doppler domain between a target and ground reflections, in order to achieve the IF, depends on the shape of the STAP filter. Figure 1.3 illustrates the position of a target in the angle-Doppler plane relative to ground reflections. The STAP filter inherently includes a notch at zero relative velocity with respect to the ground, since targets with this velocity produce signals indistinguishable from clutter. The slope of the filter determines the minimum detectable velocity (MDV), and this slope is primarily influenced by the array aperture length (see eq.1.2). A larger aperture results in a steeper slope, enabling detection of lower velocities. To estimate the MDV for each satellite configuration, we identify the target velocity that yields an output SCNR of at least 13 dB. Maintaining an SCNR above this minimum level allows the detection threshold to operate effectively, ensuring reliable target detection.

$$v_{\min} = \min \left\{ v \in \mathbb{R} \mid SCNR_{\mathsf{out}}(v) \ge 13 \,\mathsf{dB} \right\} \tag{4.3}$$

where  $v_{\rm min}$  is the MDV. Together, these three metrics provide sufficient insight to evaluate the performance of STAP under any satellite configuration. Each metric relies on the measured output SCNR, which is obtained by calculating the ratio of the power in the range cell containing the target to the average power in the range cells containing ground reflections. To avoid contamination from target side lobes, the range cells adjacent to the target are excluded from this calculation.

#### 4.2. Interference Covariance Matrix

For the implementation of STAP optimal weight vector (eq.2.24) it is necessary to estimate the interference covariance matrix  $\hat{\mathbf{R}}_Q$ . Since this is not known in practice, it is necessary to perform an estimation using the space-time received data vectors. A common way to approach this problem is to estimate a single interference covariance matrix for all the range cells, averaging over L of them as shown in the equation below. This is possible because an along-track array composed of subapertures with identical elevation characteristics results in a covariance matrix  $\hat{\mathbf{R}}_Q$  that is independent of range [2].

$$\hat{\mathbf{R}}_{Q} = \frac{1}{L} \sum_{l=1}^{L} \mathbf{x}_{l} \mathbf{x}_{l}^{H} \quad \hat{\mathbf{R}}_{Q} \in \mathbb{C}^{KN \times KN}$$
(4.4)

where  $\mathbf{x}_l$  is the  $KN \times 1$  space-time receiving data vector at range cell l. K is the number of received pulses and N is the number of antennas. This is an unbiased estimate, known as the sample covariance matrix, which converges to the true interference covariance matrix as the number of samples approaches infinity. Here, the cell under test and the cells where a target has been detected should be excluded from the data. With this expression we are assuming that that a single range-Doppler resolution cell can be regarded as an independent point scatterer, which is reasonable according to [4]. This approach requires a sufficient number of training samples that are independent and identically distributed (IID) to achieve good performance. However, in our case, as in many practical scenarios, we face a situation where the number of observations is smaller than the number of samples in each observation. As a result, the estimation of the interference covariance matrix becomes singular, lacking full rank and thus not invertible. This is a significant challenge, since our ultimate goal is to obtain a reliable estimate of its inverse. For this reason, an alternative method must be used to estimate the

interference covariance matrix  $\hat{\mathbf{R}}_Q^{-1}$  since direct inversion would result in an ill-posed estimate due to the matrix's singularity.

#### 4.2.1. Orthogonal Projection of Clutter Subspace

In the context of GMTI with spaceborne radar, the primary source of interference is clutter, which is the interference that can be suppressed using the optimal STAP weight vector. Therefore, the interference covariance matrix can be approximated by the clutter covariance matrix (CCM)  $\mathbf{R}_Q \approx \mathbf{R}_c$ . Given this assumption and the need to avoid the numerical instability associated with inverting a singular matrix, we propose approximating the inverse of the interference covariance matrix by employing the orthogonal projection onto the clutter subspace. This approach not only preserves numerical stability but also reduces computational load. This is feasible because clutter resides in a low-dimensional subspace, due to correlations across pulses and sensors, and because it is constrained by the physical relationship between angle of arrival and Doppler frequency. Since the target has a different space-time signature, it lies outside the clutter subspace. One can anticipate that a greater difference indicates the target lies further from the clutter subspace, which leads to improved performance, as the orthogonal projection onto the clutter subspace will preserve all the target signal components. The orthogonal projection onto the clutter subspace can be expressed as the identity matrix minus the projection matrix of the subspace [2]

$$\hat{\mathbf{R}}_Q^{-1} = I - \sum_{m=1}^M u_m u_m^H \quad \hat{\mathbf{R}}_Q^{-1} \in \mathbb{C}^{KN \times KN}$$

$$\tag{4.5}$$

where I is the  $KN \times KN$  identity matrix, and  $u_m$  is the eigenvector from the matrix  $\hat{\mathbf{R}}_Q$  corresponding to the m largest eigenvalue. Since  $\hat{\mathbf{R}}_Q$  is Hermitian and positive semidefinite, it possesses a complete set of orthonormal eigenvectors. The dominant eigenvectors (those associated with the largest eigenvalues) span the subspace where the clutter energy is concentrated, as clutter is the primary source of interference. For this reason, we use the M most dominant eigenvectors from the interference covariance matrix to estimate the clutter subspace. The eigenvectors that do not belong to the clutter subspace, which are the less dominant ones, are associated with noise. Overall, the interference covariance matrix contains eigenvalues that correspond either to clutter or to noise, depending on their respective power levels.

To identify the eigenvectors corresponding to the M largest eigenvalues, a threshold must be defined to distinguish them from those associated with noise. Eigenvalues below this threshold are the ones assumed to represent thermal noise. In this project we propose to use the following threshold

$$T = \sigma_N^2 \cdot CNR \tag{4.6}$$

where  $\sigma_N^2$  is the noise power and CNR is the Clutter-to-Noise ratio in linear scale after pulse compression in the matched filtering process. The purpose of this threshold is based on the fact that all eigenvalues corresponding to noise should be exactly equal to the noise power [2]. However, in practice, since we can only estimate the covariance matrix rather than access the true one, this does not hold perfectly. As a result, some of the eigenvalues associated with noise may appear larger or smaller than expected. This reduces the distinction between the eigenvalues associated with clutter and those associated with noise, particularly in scenarios with high noise power. This is further analyzed discussing the simulation results the next section.

#### 4.2.2. Eigenvalues Analysis

This section examines the estimate interference covariance matrix using eq.4.4, which is approximated by the clutter covariance matrix, along with its associated eigenvalues. The analysis is conducted within a simulation environment where the satellite configuration satisfies the DPCA condition, which means that the baseline b must be an integer multiple of the platform's displacement per pulse. This displacement is equal to the satellite velocity  $v_p$  divided by the PRF, which means that

$$b = N_{DPCA} \cdot \frac{v_p}{PRF} \tag{4.7}$$

In our case, the baseline always corresponds to the distance between the antennas. However, this does not correspond to the distance between the phase centers (virtual nodes), as each phase center is located at the midpoint between the two satellites forming a bistatic pair. This section explores a scenario where the transmitter satellite (monostatic) aligns with the positions of all virtual nodes at different time instances ( $N_{DPCA}=2$ ), as well as a more general case where this alignment does not occur ( $N_{DPCA}=3$ ).

The satellites use the parameters listed in Table 3.1 and follow the same geometric configuration shown in Figure 3.1, where three satellites receive the signal transmitted by only one of them. However, in this section only, the PRF values will vary depending on the specific simulation scenario. For simplicity, the number of integrated pulses at the receiver is fixed at 10 in these simulations, resulting in a lower-dimensional covariance matrix, and consequently, a smaller number of eigenvalues. The matrix dimensions are therefore  $30\times30$ , corresponding to the number of satellites multiplied by the number of integrated pulses. Fig.4.1 illustrates the satellite positions at consecutive time instances for  $N_{DPCA}=2$  and for  $N_{DPCA}=3$ , along with the corresponding virtual node positions for each bistatic pair. The bistatic theory was presented in section 2.4.

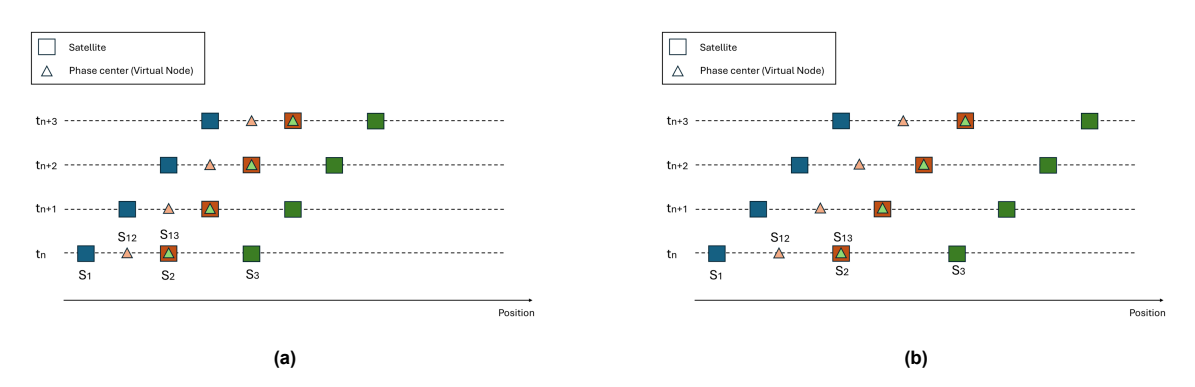


**Figure 4.1:** Representation of the three satellites positions over four consecutive time instances with only one satellite transmitting  $(S_1)$  for  $N_{DPCA}=2$  (a) and for  $N_{DPCA}=3$  (b). Each time instance represents the moment where the first satellite transmits. The location of the equivalent phase centers for the bistatic acquisitions is represented with triangles.

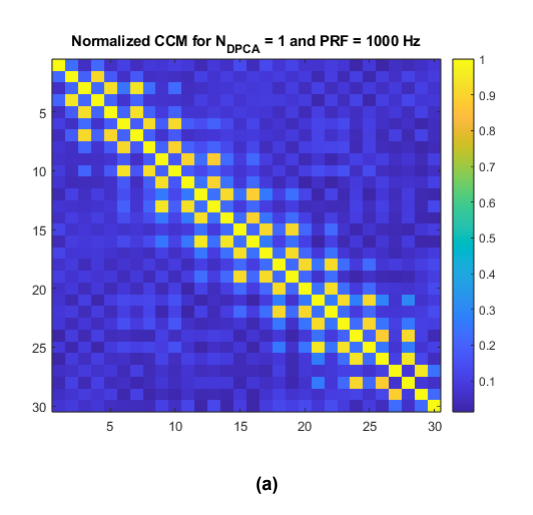
We begin by analyzing the estimated CCM for a configuration in which the satellite baseline is set to twice the distance each satellite travels between consecutive pulses ( $N_{DPCA}=2$ ), using a PRF of 1000 Hz and a CNR of 10 dB. Figure 4.2a illustrates the magnitude of each cell in the CCM for this configuration. Note that the diagonal elements represent the power at each space-time channel, while the off-diagonal elements indicate the cross-correlation between different space-time channels. For instance, with three antennas (yielding three spatial samples per slow-time instance) the entry  $\hat{\mathbf{R}}_{Q_{6,10}}$  corresponds to the correlation between antenna 3 at the second received pulse and antenna 1 at the fourth received pulse.

Since  $N_{DPCA}=2$ , in this simulation, during the second received pulse, the first satellite, which serves as the transmitter, is positioned at the virtual node located between the transmitter and the second satellite (see time instant  $t_n+1$  in Fig.4.1a). For this reason, the cross-correlation between the sample from the second antenna and the sample from the first antenna in the previous pulse is nearly as strong as the autocorrelations. Furthermore, after two transmitted pulses, the first satellite reaches the virtual node position corresponding to the pair formed by satellites 1 and 3.

As a result, we observe a strong correlation between the samples from the third satellite and those from the first satellite associated with the second-to-last transmitted pulse. Finally, there is also a strong cross-correlation between the samples from the second and third satellites at consecutive time instances. This is because, during these time steps, the virtual nodes formed between each of these satellites and the transmitter are located at the same position. In addition, aside from the high cross-correlations previously mentioned, all other correlations are significantly low, as they do not correspond

to a pair of space-time samples of different satellites that are observing reflections from the same location at different time instances.

Regarding the eigenvalues, Figure 4.2b presents the normalized eigenvalues of the CCM, ordered from largest to smallest. It can be observed that there are 12 dominant eigenvalues, which are estimated to correspond to the clutter subspace, as they all exceed the threshold defined in eq.4.6. As expected, due to the limited number of observations used to estimate the CCM, the dominant eigenvalues do not have identical magnitudes. These 12 dominant eigenvalues reflect 12 independent observations. This number is significantly lower than the total of 30 space-time channels, primarily due to the strong space-time cross-correlations identified in the CCM analysis shown in Fig.4.2a. These correlations are particularly high because the DPCA condition is fully satisfied. If this condition were not met, the number of dominant eigenvalues (representing independent observations) would increase.



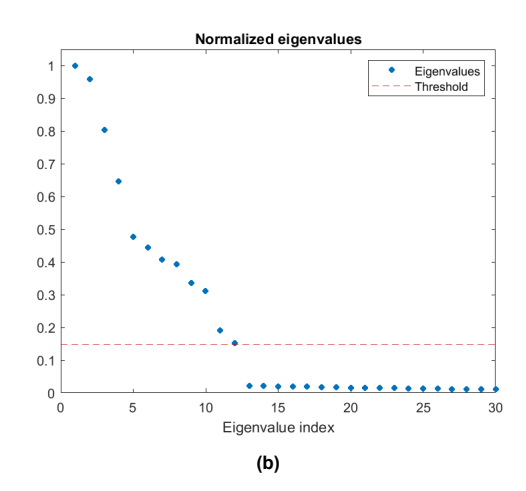
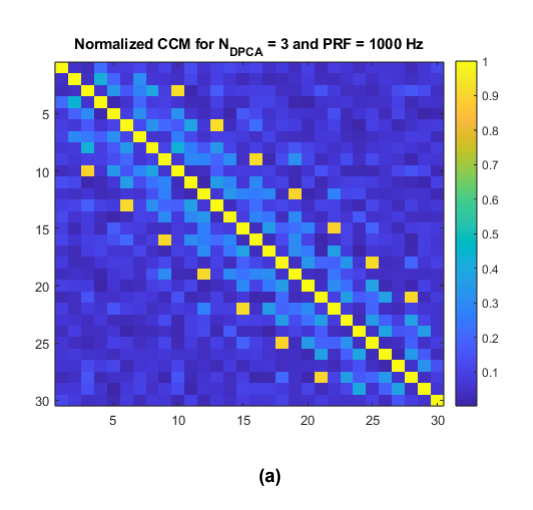


Figure 4.2: Estimated normalized clutter covariance Matrix for PRF = 1000 Hz and  $N_{DPCA} = 2$  and 10 integrated pulses (a) and its respective normalized eigenvalues with the corresponding threshold that indicates the estimated separation between the noise and the clutter eigenvalues (b)

The 12 independent observations result from the 12 unique positions of the virtual node across the integration interval. These distinct positions can be seen in Fig. 4.1a. After the second transmitted pulse, the virtual node positions begin to repeat throughout the interval. As a result, the number of independent observations equals the number of transmitted pulses plus two—yielding 12 for 10 transmitted pulses. This outcome holds only under perfect DPCA conditions. Additionally, it requires that the virtual node positions remain uncorrelated across consecutive time instances. This lack of correlation is satisfied for a PRF of 1000 Hz, but not for a PRF of 8150 Hz, as will be discussed later in the section. It can also be anticipated that reducing the alignment of virtual node positions across pulses would lead to an increase in the number of independent observations.

For instance, in a second simulation using the same parameters but with  $N_{DPCA}=3$ , the transmitter no longer aligns with the virtual node position at any time instance for the bistatic pair formed by the transmitter and the second satellite. This is because the virtual node position lies exactly between the first and second transmitted pulses (see Fig.4.1b). However, this is not the case for the virtual node formed between the transmitter (satellite 1) and satellite 3. After three transmitted pulses, the transmitter reaches this virtual node position. As a result, Fig.4.3a shows a strong cross-correlation between the samples from satellite 1 and satellite 3 when there is a time difference of three instances.

Additionally, in Fig.4.3b, we observe an increase in the number of dominant eigenvalues. This is due to the reduced level of strong space-time cross-correlations, which leads to a greater number of independent observations. Consequently, the distinction between eigenvalues associated with clutter and those associated with noise becomes less pronounced. This makes it more challenging to set a threshold that reliably separates the clutter subspace, potentially causing one clutter-related eigenvalue to fall below the threshold and be excluded.



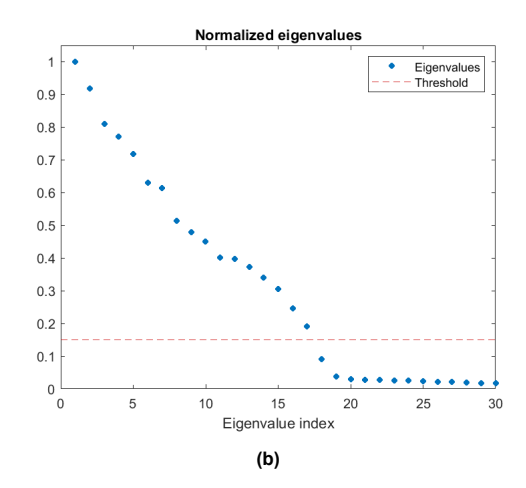


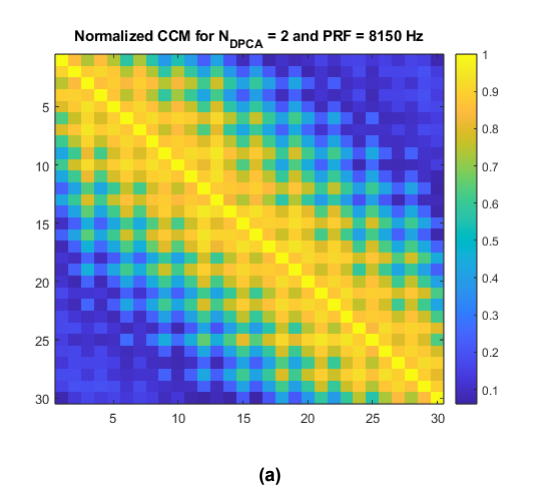
Figure 4.3: Estimated normalized clutter covariance Matrix for PRF = 1000 Hz and  $N_{DPCA} = 3$  and 10 integrated pulses (a) and its respective normalized eigenvalues with the corresponding threshold that indicates the estimated separation between the noise and the clutter eigenvalues (b)

Next, we change the PRF to the actual value that will be used throughout the project which is 8150 Hz, which the expected value to be used in a SwarmSAR system. To meet the DPCA condition, the baselines have to be much lower for the same  $N_{DPCA}$ . This causes to increase the cross-correlation between spatial samples from consecutive pulses. Figures 4.4a and 4.5a display the magnitude of the Clutter Covariance Matrix (CCM) for a PRF of 8150 Hz, with  $N_{DPCA}=2$  and  $N_{DPCA}=1$  respectively. In both cases, the high cross-correlation observed between consecutive pulses is comparable to the cross-correlation between space-time samples where the transmitter is positioned at the virtual node relative to the corresponding receiver in the bistatic pair.

Fig.4.4a and Fig.4.5a show the magnitude of the CCM for 8150 Hz PRF and for  $N_{DPCA}=2$  and  $N_{DPCA}=1$ , respectively. We see that in both cases, the high cross-correlation between consecutive pulses is comparable with the cross-correlation in space-time samples between the transmitter being at the virtual node position and the corresponding receiver the bistatic pair. Additionally, since high cross-correlation effectively reduces the number of independent observations, the number of dominant eigenvalues is significantly lower for both values of  $N_{DPCA}$ . Fig.4.4b and Fig.4.5b show that in both cases, only 3 out of the 30 total eigenvalues are estimated to correspond to the clutter subspace. Even if there are more than three distinct virtual node positions, the high cross-correlation between them means that the number of independent observations does not correspond to the number of positions. The high correlation is due to the significantly smaller observation window, which results in a much lower number of independent observations. Unlike the case with a PRF of 8500 Hz, there is no longer a difference in the number of dominant eigenvalues between the two  $N_{DPCA}$  configurations.

The reduction of number of dominant eigenvalues due to the increase of the PRF makes the covariance matrices nearly singular and complicates the prediction of the number of relevant eigenvalues. The reduction in the number of dominant eigenvalues can also be interpreted as a shortening of the observation window, since with a fixed number of received pulses, the satellites move less during the integration period. It is now no longer feasible to rely on the transmitter's alignment with virtual node positions of different bistatic pairs across time instances to predict the estimation of the dominant eigenvalues.

It is also worth noting the similarities between the STAP weight vector and the DPCA algorithm. In the case of DPCA, only two satellites are used, and the core idea is to subtract signals from two time instances where the phase center is located at the same position. In our case, these time instances correspond to moments when the transmitter reaches the virtual node position of a bistatic pair, after a certain number of transmitted pulses. In the analyzed scenario where  $N_{DPCA}=3$  and the PRF is 1000 Hz, Fig.4.3a illustrates that, despite the presence of three satellites, the STAP weight vector predominantly emphasizes samples from a single bistatic pair—similar to the DPCA approach. Consequently, the inverse of the CCM exhibits one strong negative cross-correlation per row.



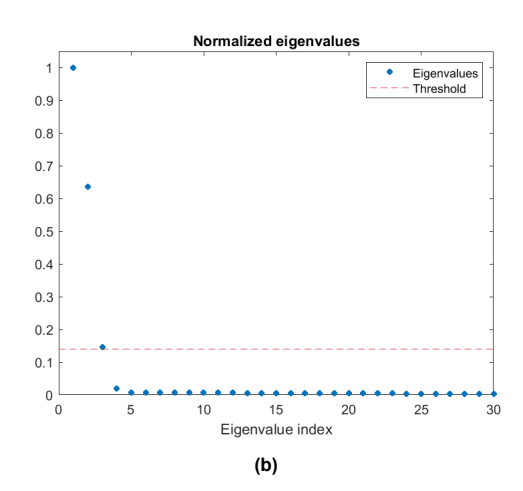
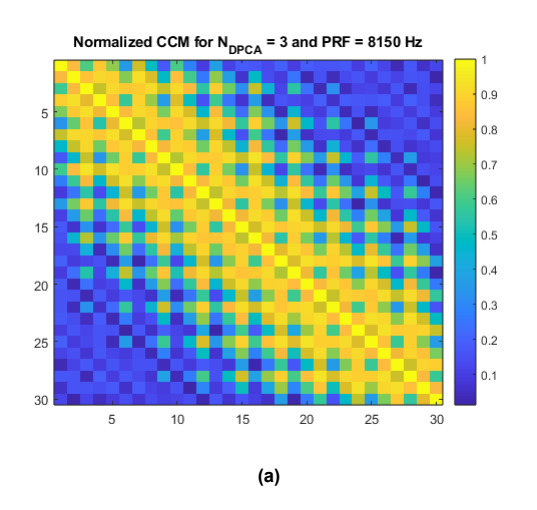


Figure 4.4: Estimated normalized clutter covariance Matrix for PRF = 8150 Hz and  $N_{DPCA} = 2$  and 10 integrated pulses (a) and its respective normalized eigenvalues with the corresponding threshold that indicates the estimated separation between the noise and the clutter eigenvalues (b)



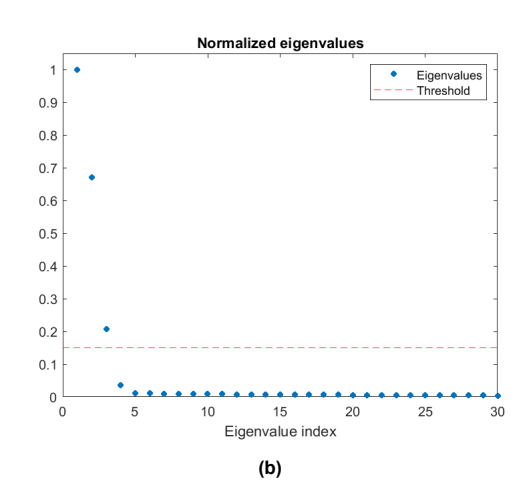


Figure 4.5: Estimated normalized clutter covariance Matrix for PRF = 8150 Hz and  $N_{DPCA} = 3$  and 10 integrated pulses (a) and its respective normalized eigenvalues with the corresponding threshold that indicates the estimated separation between the noise and the clutter eigenvalues (b)

This is shown in Fig.4.6 which shows the magnitude inverse CCM calculated using eq.4.5, for  $N_{DPCA}=3$  and PRF equal to 1000 Hz. We see that the cells off the diagonals with higher magnitude correspond to the cells with high cross-correlation in Fig.4.3a. When this inverse is applied to the received spacetime data, the effect is equivalent to subtracting two space-time samples sharing the same phase center, which is the same as the operation that would take place in the DPCA algorithm. This observation highlights that DPCA can be viewed as a specific case of the STAP algorithm.

Overall, this section examined the cross-correlation between space-time samples as a function of satellite baseline, and how it affects the number of dominant eigenvalues in the CCM. To make the interpretation of the CCM magnitudes more accessible, the analysis was performed using only 10 integrated pulses instead of the 512 that will be used in the rest of the project. Table 4.1 shows a summary of the results obtained from these section for a direct comparison.

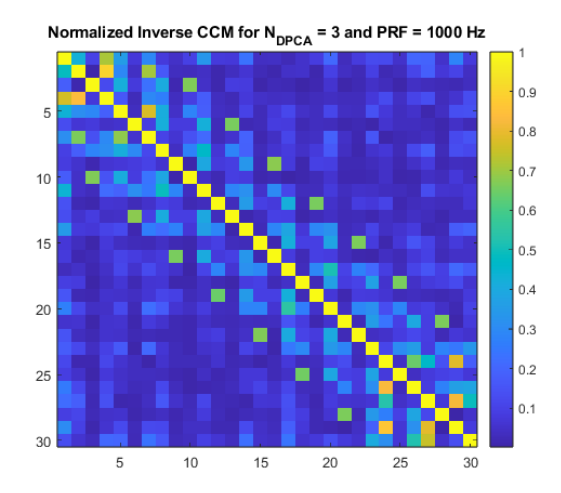


Figure 4.6: Normalized Inverse Clutter Covariance Matrix for  $N_{DPCA}=3$  and PRF=1000 Hz

N <sub>DPCA</sub>	PRF	Baseline	Number Dominant Eigenvalues (Out of a Maximum of 30)
2	1000 Hz	14 m	12
3	1000 Hz	21 m	17
2	8150 Hz	1.72 m	3
3	8150 Hz	2.58 m	3

**Table 4.1:** Comparison of the number of dominant eigenvalues for various baselines under DPCA condition for 3 satellites and 10 integrated pulses

## 4.3. STAP Processing

#### 4.3.1. Proposed Methodology

This section presents an analysis of the results obtained following the application of the STAP optimal weight vector (eq.2.24) to the received data. The performance evaluation is carried out using the metrics defined in Section 4.1, focusing on a satellite formation composed of three units (each equipped with a single antenna) and a single transmitter. The metrics are examined under varying target velocities and angles of arrival for a single target scenario. Additionally, the satellites are arranged with uniformly spaced along-track baselines, as detailed in the previous section. The parameters used are the ones described in Table 3.1 with 512 integrated pulses and thus a CPI of 62.8 milliseconds. After the application of STAP optimal weight vector to the received data we are left with a single complex number per range cell.

$$\mathbf{y} = \mathbf{w}_{opt}^H \mathbf{x} = \mathbf{v}(\phi, f_t)^H \mathbf{R}_Q^{-1} \mathbf{x} \quad \mathbf{y} \in \mathbb{C}^{1 \times 1}$$
 (4.8)

where  $\mathbf{v}(\phi,f_t)$  is the target space-time steering vector and  $\mathbf{x}$  is the received space-time vector at every range cell. An overview of the simulation parameters used is provided in Table 4.2. These parameter values are chosen to reflect conditions that could be encountered in real SwarmSAR scenario. For thermal noise, we assume a SNR of 10 dB after range compression. We focus on the SNR at the output of the matched filter, following range compression, since the STAP algorithm is independent of the gain introduced by the time-bandwidth product. All ratio values are provided prior to applying the optimal STAP weight vector. This is equivalent to computing the ratios based on a single received pulse from each satellite radar after range compression. The selected RCS is comparable to that of a typical car.

Parameter	Value
Number of Satellites	3
Number of Targets	1
RCS	10 $m^2$
$SCNR_{in}$	-10 dB
$SNR_{\sf in}$	0 dB
$CNR_{in}$	10 dB

Table 4.2: Parameters for STAP performance analysis

In practice, the exact range cell containing the target is unknown. However, for the purpose of this performance analysis, we assume that the target's location is known. This assumption allows us to exclude the target cell and its adjacent cells from the calculation of the interference covariance matrix. Without prior knowledge of the target's position, it would be necessary to treat every range cell as a potential target location. Consequently, the interference covariance matrix would need to be recalculated multiple times, each time excluding a different candidate cell and its neighboring cells. Moreover, assuming prior knowledge of the target's position is essential for conducting the performance analysis, as it enables the measurement of the SCNR of  $\bf y$ . To compute the SCNR, we evaluate the power in the target range cell and compare it to the power in the remaining range cells, excluding those adjacent to the target. These excluded cells are the same ones omitted from the interference covariance matrix calculation.

The interference covariance matrix is computed as shown in eq.4.4, as discussed in the previous section. Notably, the simulated grid, which spans 5 kilometers per side, corresponds to a slant range width of approximately 1.85 kilometers (see the geometry in Fig. 3.1). This slant range width is also evident in the impulse response of ground reflections shown in Fig.3.4. It corresponds to 370 range cells, each 5 meters wide, as determined by the 30 MHz sampling frequency. This implies that, for the calculation of the interference covariance matrix, there are 370 space-time vectors  $\mathbf{x}$  available for averaging. Given that the number of integrated pulses is 512 and the number of antennas (equal to the number of satellites) is 3, the dimension of each vector  $\mathbf{x}$  is 1536  $\times$  1. Consequently, the number of observations (370) is smaller than the number of samples per observation (1536), which is not ideal. A direct implication is that only 370 out of the 1536 eigenvalues of the covariance matrix will be non-zero.

However, as discussed in the previous section, when the pulse repetition frequency (PRF) is 8150, the number of dominant eigenvalues (representing effectively independent observations) can be significantly smaller than the total number of eigenvalues, due to the high correlation between consecutive pulses. Therefore, the estimate based on 370 observations is expected to be sufficiently accurate, provided that this number exceeds the number of dominant eigenvalues. However, to evaluate the accuracy of the interference covariance matrix estimation with this number of observations, it is necessary to examine the STAP results for the given satellite configuration, as will be done in this section. Particular attention should be given to the  $SCNR_{Loss}$ , as it reflects how closely the obtained results match the theoretical values.

Regarding the calculation of the true interference covariance matrix that is necessary to obtain the  $SCNR_{Loss}$  metric (eq.4.1), we will use the sample covariance matrix but using a much larger number of samples. To know when the number of samples is large enough we study the convergence to the true covariance matrix. For this purpose, we run several iterations, each time adding 370 observations (or range samples) to the computation of the matrix. After each iteration, we compute the Frobenius norm of the difference between the newly calculated interference covariance matrix, which includes the newly added samples, and the interference covariance matrix from the previous iteration (see Fig.4.7). Although this remains an estimation we refer to it as the true covariance matrix.

$$\Delta = ||\mathbf{R}_{Q_i} - \mathbf{R}_{Q_{i-1}}||_F \tag{4.9}$$

where i is the current iteration number. We continue performing iterations until this Frobenius norm becomes sufficiently small. Specifically, we stop when the Frobenius norm is one thousand times smaller than its maximum value, which corresponds to the Frobenius norm calculated in the first iteration. This point is selected as the moment of convergence. We then consider the estimated matrix obtained at that point as the true interference covariance matrix.

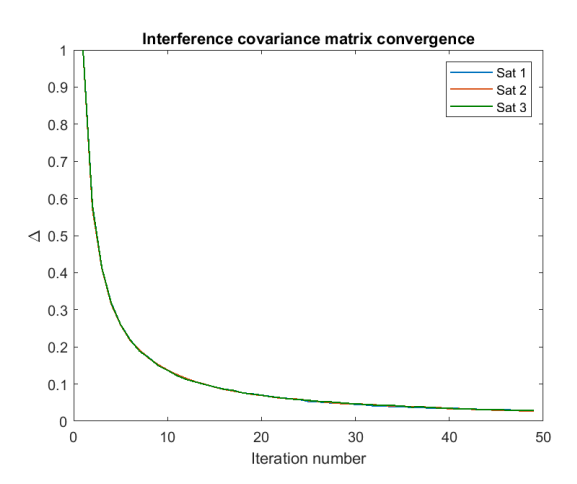


Figure 4.7: Interference covariance matrix convergence for 25 m, 50 m, and 100 m baselines.

#### 4.3.2. STAP Performance Results

For the performance results analysis, we study three different cases with varying baselines. All baselines are uniform, meaning the distances between adjacent satellites are equal. Each baseline is at least on the order of one hundred times the wavelength (9 cm), which results in the presence of grating lobes and, consequently, angular ambiguities when the satellites are treated as a single array. In other words, multiple angle-of-arrival solutions may arise, complicating accurate target localization. It is important to note that, since radial velocity is linked to the angle of arrival, accurately estimating this angle is essential for correctly determining the target's radial velocity. For example, a target located at an angle of 0.5 degrees will exhibit a measured velocity composed of both the velocity induced by the angle (approximately 60 m/s for 0.5 degree) and the target's actual radial velocity (see eq.2.17). Therefore, if the angle of arrival is not correctly estimated, the resulting radial velocity estimate will also be inaccurate, as it is necessary to subtract the induced velocity due to the angle to the total velocity to get the radial velocity of the target. However, this very large aperture (on the order of tens of meters) enables the detection of targets with extremely low radial velocities, potentially below 1 m/s.

First, we analyze a baseline of 25 meters. The eigenvalues corresponding to this configuration can be seen in Fig.4.8a. It is important to note that only 370 out of the 1536 eigenvalues are displayed in the plot, as these are the only ones with non-zero values—corresponding to the number of available observations. Among these, the thresholding method identifies 95 dominant eigenvalues associated with clutter, which are interpreted as independent clutter observations. This low number of dominant eigenvalues is due to the high cross-correlation between space-time samples of consecutive pulses received by the same antenna, as well as the strong correlation between space-time samples corresponding to the moments when the transmitter reaches the virtual node of each bistatic pair. These moments of high correlation occur because the received signal closely resembles one that has already been captured. This redundancy reduces the number of independent observations, and consequently, the number of significant eigenvalues. Although the total number of observations (370) is significantly lower than the number of samples per observation (1536), it still exceeds the number of independent clutter components (95). This indicates that the sample covariance-based estimation method (Eq.4.5) should have a sufficient number of samples to yield a reliable estimate.

Figure 4.10b presents the eigenvalues derived from the true interference covariance matrix. Due to the increased number of observations relative to the number of samples per observation, we observe that no eigenvalues are equal to zero. Additionally, we observe that the slope of the tail corresponding to the noise-related eigenvalues is now flatter. In the theoretical case where the number of observations

is equal to infinity, this slope would become completely flat, and all noise-related eigenvalues would converge to the same power level—equal to the noise power. This would result in an even more distinct separation between eigenvalues associated with noise and those associated with clutter. We also observe that the number of dominant eigenvalues selected by the threshold remains unchanged at 95, consistent with the results obtained using the estimated interference covariance matrix with 370 observations.

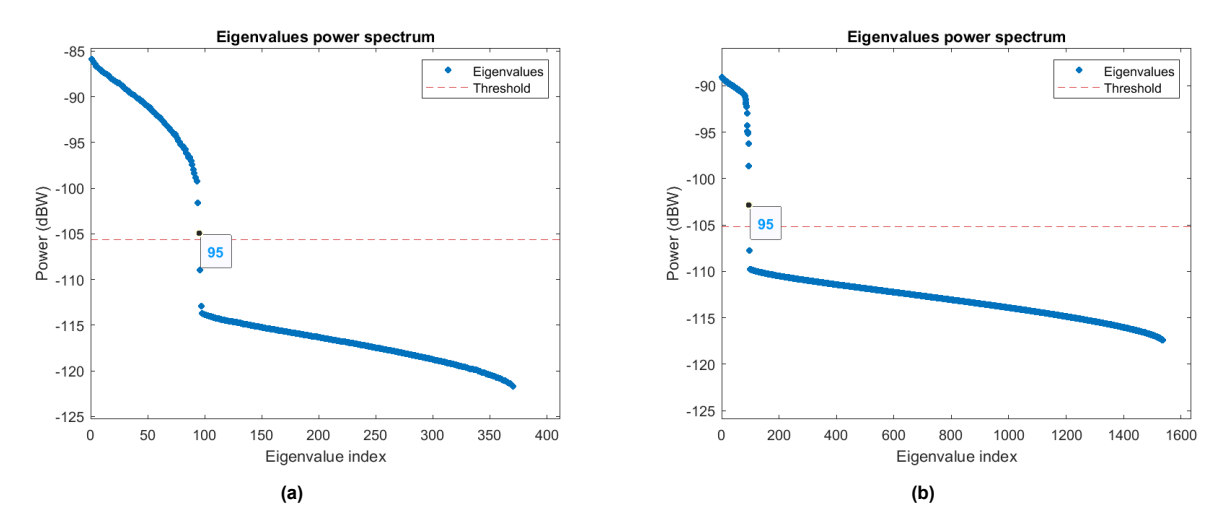


Figure 4.8: Power spectrum of (a) obtained eigenvalues and (b) true eigenvalues for 25 meter baseline with a PRF of 8150 Hz

By examining the expression for the phase delay between elements in a uniform linear array (ULA), as shown in eq.2.14, we can isolate the inter-element spacing variable. From this, we determine that the first angle-of-arrival ambiguity occurs at 0.215 degrees ( $\theta = \arcsin(\lambda/d)$  where d is the baseline). Due to the platform's motion, each angle-of-arrival corresponds to a specific Doppler velocity (as described in eq.1.1). In this case, the angle ambiguity translates to a velocity of 26.25 m/s, which explains the presence of ambiguity at this velocity in Fig.4.15a for this baseline. This figure illustrates the IF response for various combinations of the target's radial velocity, while maintaining a fixed angle-of-arrival of 0 degrees. In contrast, Fig.4.15b presents the IF response for varying angles-of-arrival, while keeping the target's radial velocity fixed at 0 m/s. Interestingly, a radial velocity of 0 m/s can still be detected when the angle-of-arrival is non-zero. This occurs because, although the measured radial velocity is zero, the target is not stationary relative to the ground—it still has motion. If the target was truly static, its measured radial velocity would exactly match the velocity associated with the angle-of-arrival as defined by Equation 1.1, making it indistinguishable from clutter and thus undetectable. For an angle-of-arrival of 0 degrees, this condition corresponds to a velocity of 0 m/s, resulting in a notch in the IF response.

Additionally, Fig.4.9a shows the IF for various combinations of angle-of-arrival and target velocity. Note that Fig. 4.15a and Fig. 4.15b show line profiles extracted from Fig. 4.9a, corresponding to a fixed target velocity of 0 m/s and a fixed angle of 0 degrees, respectively. The maximum angle of arrival shown in the figure corresponds to the largest angle defined within the 5 km × 5 km grid. It can be observed that the ambiguous velocity decreases as the angle of arrival increases. This is because a larger angle results in a greater induced velocity from the platform's motion, thereby requiring a smaller component of the target's radial velocity to reach the total measured velocity corresponding to the ambiguous velocity. For example, at an angle of 0.1°, the platform-induced velocity is 12.21 m/s. To reach the ambiguous velocity of 26.3 m/s (due to the 25 meters baseline), only 14.09 m/s of target radial velocity is needed, which is where we see the ambiguity.

It is worth noting that the maximum IF value—approximately 31 dB—is observed for combinations of target velocity and angle of arrival that are well separated from the clutter subspace. This aligns closely with the theoretical maximum IF, which is achieved when clutter is entirely suppressed. In such an ideal case, the IF equals the sum of the number of integrated pulses and the number of antennas. In our case, with 512 pulses and 3 antennas, the theoretical maximum is 31.86 dB, which explains the peak

values of the obtained IF observed in the plot. To compare the theoretical and obtained values, refer to Fig. 4.9b, which presents the  $SCNR_{Loss}$  in an angle-velocity plot. This figure illustrates the deviation of the measured result from the theoretical one, which is derived using the true interference covariance matrix. The loss is more significant when the target lies closer to the clutter subspace, highlighting the critical importance of accurate estimation in such scenarios. Therefore, using the true interference covariance matrix results in narrower notches with steeper slopes, which enhances the MDV.

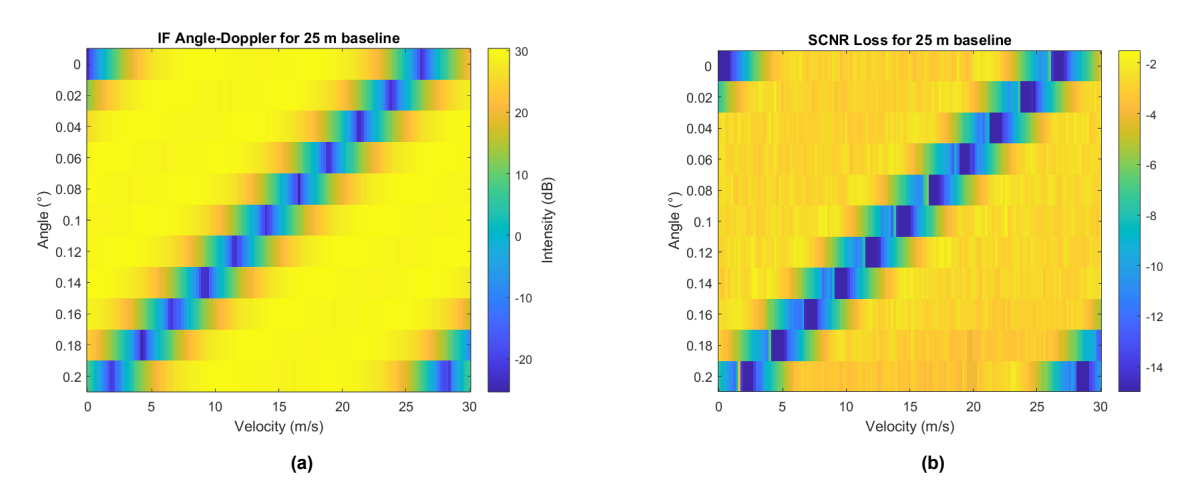


Figure 4.9: Angle-Doppler Improvement Factor (a) and  $SCNR_{Loss}$  (b) for 25 meters baseline

To evaluate the MDV at a 25-meter baseline, we analyze the  $SCNR_{\rm out}$  after applying STAP. The MDV is defined as the lowest velocity that yields 13 dB of  $SCNR_{\rm out}$  (see Eq. 4.3). This evaluation is performed at 0 degrees angle of arrival, where no additional velocity is induced in ground reflections by platform motion. At this angle, the measured radial velocity of the target corresponds directly to its velocity relative to the ground. Using the IF metric, we then relate  $SCNR_{\rm out}$  to a chosen  $SNR_{\rm in}$ . Based on the IF results shown in Fig. 4.15a, and for an  $SNR_{\rm in}$  of 10 dB, the MDV at a 25-meter baseline is 0.92 m/s.

Continuing the analysis, the same procedure is applied for a 50 meter baseline. Figure 4.10a presents the resulting eigenvalues for this configuration. The threshold now identifies 100 dominant eigenvalues associated with clutter—five more than in the 25 meter baseline case. This increase is due to the larger baseline, which allows for more independent observations. With a wider separation, there is less overlap in the satellite trajectories, meaning it takes longer for the transmitter satellite (satellite 1) and the virtual node formed by the bistatic pair of satellite 1 and satellite 2 to reach the initial position of the virtual node formed by satellite 1 and satellite 3. This reduced overlap enhances the diversity of observations. The exact number of additional dominant eigenvalues resulting from a larger baseline is difficult to predict without the simulation, primarily due to the high correlation between virtual node positions within the same antenna. This correlation arises from the use of a high PRF of 8150 Hz. Regarding the eigenvalues derived from the true clutter covariance matrix, we observe that, as with the 25 meters baseline, the number of dominant eigenvalues selected remains unchanged.

Next, we observe that the 50 meter baseline introduces an angular ambiguity of approximately 0.107 degrees, as shown in Fig. 4.15a, which displays the IF at a fixed velocity of 0 m/s. This angular ambiguity corresponds to a velocity ambiguity of 13.12 m/s, as illustrated in Fig. 4.15b, where the IF is shown at a fixed angle of 0 degrees. Compared to the 25 meter baseline, both angular and velocity ambiguities are halved. However, the notches become narrower due to the increased aperture, which enhances the MDV from 0.92 m/s (at 25 meters) to 0.34 m/s for an  $SNR_{\rm in}$  of 10 dB. Additionally, Fig. 4.11a presents the full angle-velocity response, highlighting the combined effects of these ambiguities.

It is important to note that now the maximum observed value (approximately 28 dB) is now lower than the theoretical sum of the integration gain and array processing gain (31.86 dB). This discrepancy of about 3 dB arises because the baseline is now sufficiently large that each satellite measures a noticeably different velocity. The reference satellite for the matched target velocity vector (eq.2.20) is satellite 1. The velocities measured by satellite 2 and satellite 3 differ enough from the velocity measured by satellite 1 so that they fall between the velocity cell centered at the value measured by satellite 1 and

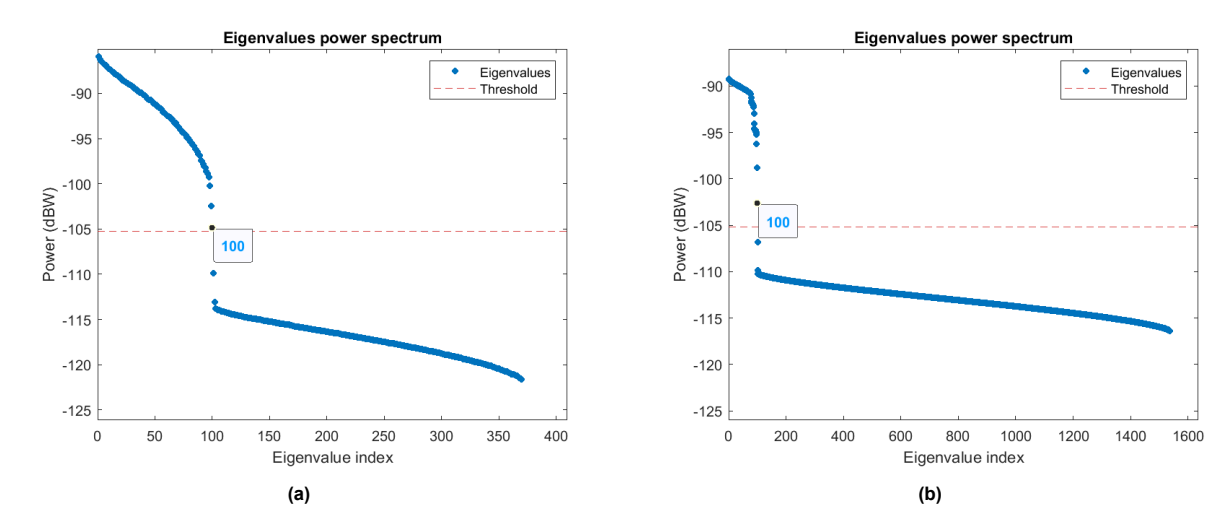


Figure 4.10: Power spectrum of (a) obtained eigenvalues and (b) true eigenvalues for 50 meter baseline with a PRF of 8150 Hz

the adjacent cell. This adjacent cell is centered at a velocity that differs by 0.75 m/s, which corresponds to the velocity resolution defined by Equation 2.6. This causes the signal energy to spread across two velocity cells. Consequently, when combining all three spatial samples (from the three satellites), the energy dispersion results in a peak value that is approximately 3 dB lower. This is highlighted in the  $SCNR_{Loss}$  results presented in Fig. 4.11b, where the loss is at least 3 dB for the angle-velocity pairs corresponding to the peak values of the IF (approximately 28 dB).

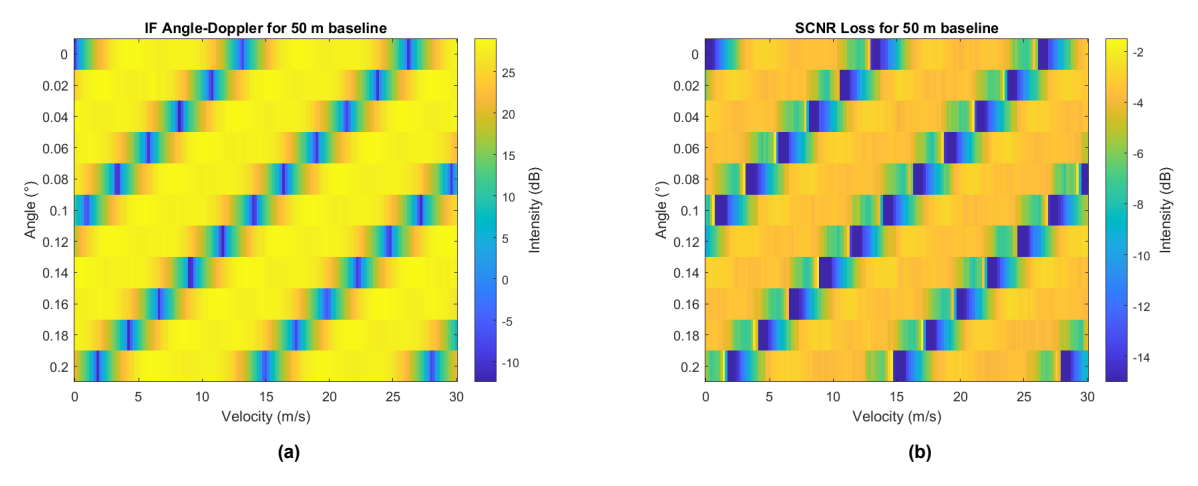
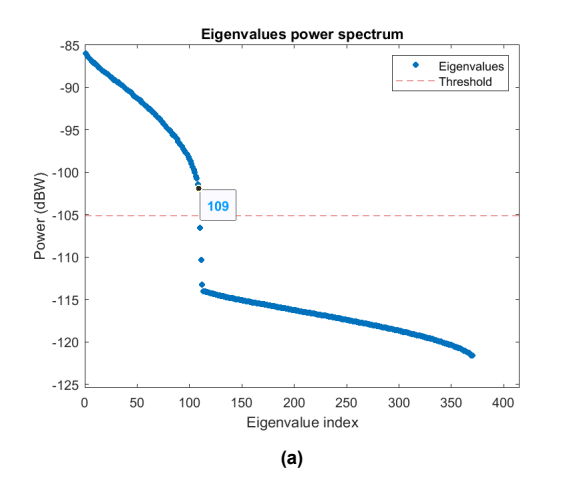


Figure 4.11: Angle-Doppler Improvement Factor (a) and  $SCNR_{Loss}$  (b) for 50 meters baseline

As a final baseline to analyze we now analyze 100 meters baseline. As expected, now there is more dominant eigenvalues selected by the threshold as the baseline is larger than before (Fig.4.12). We see that there are now 109 eigenvalues which is 9 more with respect to the previous baseline. Once again, even though there are more than 9 additional virtual node positions, the high correlation among them significantly limits the number of new, independent eigenvalues to just 9.

Fig. 4.13a illustrates that the ambiguous velocity is halved (6.56 m/s), as the baseline has doubled compared to the previously analyzed 50 meter baseline. Additionally, the maximum value of the IF is now approximately 26 dB. This reduction is due to the absence of array processing gain—i.e., the gain resulting from the coherent combination of spatial samples. Note that in our setup, each satellite provides one spatial sample. The reason for the lack of array processing gain is that the velocity differences measured by each satellite are large enough that they fall into different velocity cells. Consequently, when we use the velocity measured by the transmitter satellite as a reference to compute the



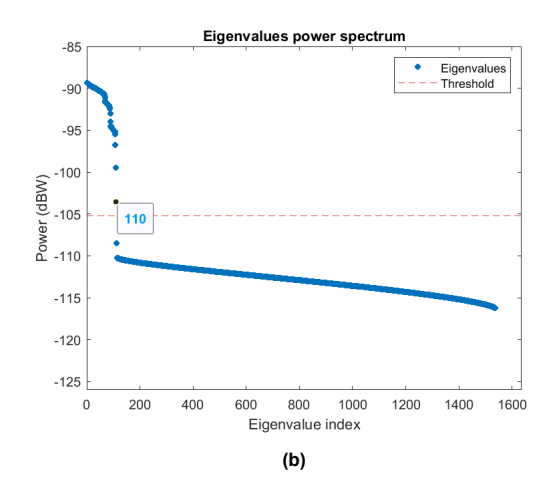
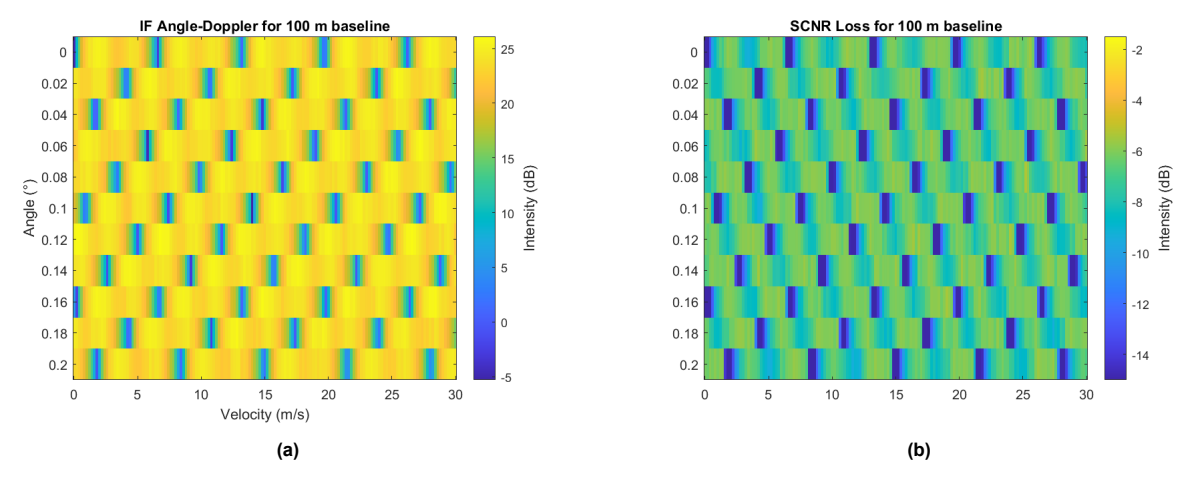


Figure 4.12: Power spectrum of (a) obtained eigenvalues and (b) true eigenvalues for 100 meter baseline with a PRF of 8150 Hz

matched target vector (formed by the Kronecker product of the spatial and temporal steering vectors (see eq. 2.18)) we are not coherently combining spatial samples, since the velocities measured by the other satellites do not align within the same velocity cell.



**Figure 4.13:** Angle-Doppler Improvement Factor (a) and  $SCNR_{Loss}$  (b) for 100 meters baseline

To observe the velocity measured by each satellite, an FFT can be applied to the consecutive time samples (slow time) within the range cell where the target is located. This process is equivalent to applying a matched filter across all possible target velocities, with a step of 0.75 m/s (see eq. 2.6). Fig.4.14 displays the results of the FFTs performed on the slow-time data from each of the three satellites. The velocity assigned to the target in the simulation is chosen as a representative example. As shown, three distinct peaks appear, each corresponding to the target's velocity measured by a different satellite. The target velocities are -5.22 m/s for Satellite 1, -5.96 m/s for Satellite 2, and -6.70 m/s for Satellite 3. This indicates a consistent difference of 0.75 m/s—equivalent to one velocity cell—between each pair of adjacent satellites. It is also worth mentioning that the difference in the target range measurements between satellites is smaller than the range resolution.

Fig. 4.15a illustrates that the notch slope in the 100 m baseline is significantly narrower compared to the other baselines, yielding an MDV of 0.15 m/s for an  $SNR_{\rm in}$  of 10 dB—representing the best MDV performance observed. However, it is important to note that taking full advantage of this low MDV may be challenging in real-world scenarios because ground clutter, such as tree leaves or grass moved by the wind, can exhibit very slow motion.

4.4. Summary 40

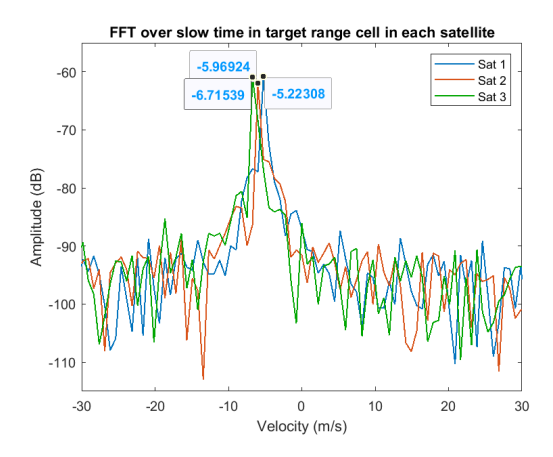


**Figure 4.14:** FFT over the slow-time data in the target's range cell for each satellite. The resulting velocity estimates for the target are 5.2, 5.3, and 5.4 m/s for satellites 1, 2, and 3, respectively.

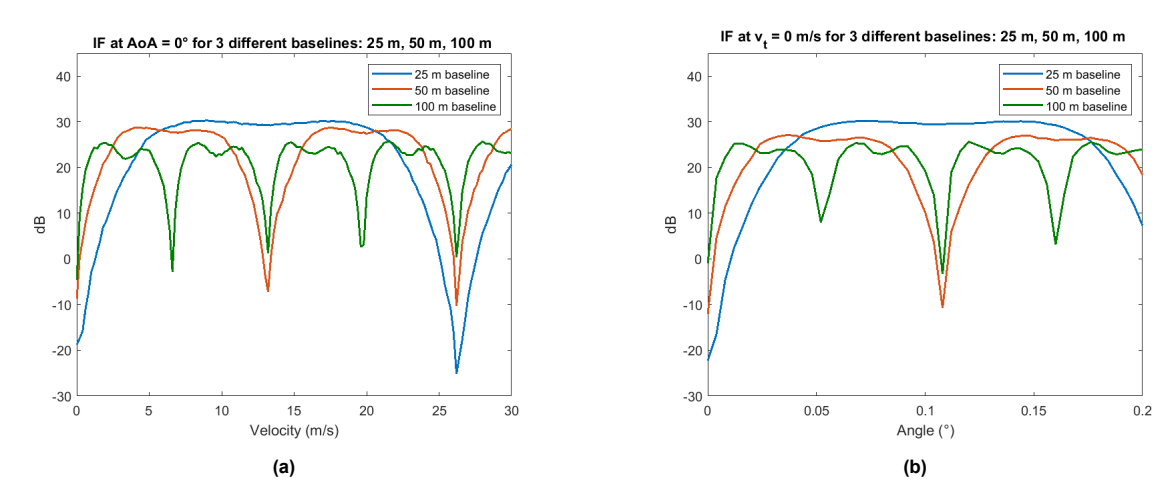


Figure 4.15: Improvement Factor comparison for 25 m, 50 m and 100 m baseline: (a) at a fixed target velocity of 0 m/s, and (b) at a fixed angle of 0 degrees.

Baseline (m)	First ambiguos	First ambiguos	Number of dominant	MDV (m/s)
Buseline (III)	velocity (m/s)	angle (°)	eigenvalues (out of 1536)	1010 (111/3)
25	26.25	0.215	95	0.92
50	13.12	0.107	100	0.34
100	6.56	0.054	109	0.15

Table 4.3: Classical STAP results

## 4.4. Summary

This chapter examined the procedure followed to implement the classical STAP algorithm within a SwarmSAR system. A key aspect of STAP implementation is the accurate estimation of the interference covariance matrix, which is essential for achieving effective performance.

To address this, we adopted the well-established sample covariance matrix estimation method. This approach is implemented averaging across range cells, which serve as the observations. Although the number of range cells (370) is smaller than the number of samples per space-time vector in each cell (1536), the estimation remains robust. This is because the number of observations (370) exceeds the

4.4. Summary 41

number of dominant eigenvalues (approximately 100), which corresponds to the number of independent components in the interference. Since the number of dominant eigenvalues is relatively small, the interference covariance matrix is nearly singular. To address this, its inversion—required for the STAP implementation (see eq. 2.24)—was approximated using an orthogonal projection onto the clutter subspace. Estimating this subspace involved selecting the eigenvectors associated with the dominant eigenvalues. To accurately identify these dominant eigenvalues, a thresholding method was developed based on noise power estimation and the CNR. While estimating the CNR can be more challenging in real-world scenarios, a practical alternative is to assume a fixed CNR value tailored to the specific environment under study.

A comparison between the estimated and theoretical results—derived using the true interference covariance matrix—demonstrates that the sample-based estimate and the selection of the most dominant eigenvalues is indeed reliable. Furthermore, the IF metric highlighted the primary advantage of a larger baseline: improved MDV. However, it also revealed a key drawback—an increase in velocity ambiguities. Additionally, when the baseline reached 100 meters, the IF metric dropped significantly. This occurred because the spatial samples could no longer be coherently combined (i.e., loss of array processing gain), as each satellite measured a different velocity exceeding the velocity cell width of 0.75 m/s.

In addition to the drop in the IF metric, another practical issue arises. In real-world scenarios, the target's velocity is typically unknown, requiring a velocity search by varying both the velocity and angle of arrival in the space-time steering vector. For large baselines, such as 100 meters, this process becomes problematic: even when searching within the non-ambiguous velocity range, the system may produce three separate detections corresponding to three different velocities—one for each satellite. This poses a significant challenge in multi-target environments, where it becomes difficult to determine which detections correspond to the same physical target. To address this issue, the next chapter introduces a technique designed to mitigate this problem.

# Proposed approach for STAP in SwarmSAR

This chapter proposes a novel approach to improve the efficiency of the STAP algorithm in a Swarm-SAR system. This chapter discusses both the methodology and the motivation behind the proposed approach. Additionally, we conduct simulations to demonstrate the effectiveness of this method compared to the classical STAP algorithm. It also includes an analysis of a more general case in which the satellite baselines are non-uniform.

#### 5.1. Motivation

In the previous chapter, we implemented the classical STAP algorithm for a SwarmSAR system and observed a significant drop in performance for baselines of approximately 100 meters or more. This degradation occurs because the spatial samples cannot be coherently combined—resulting in a loss of array processing gain—as each satellite measures a different target radial velocity that exceeds the velocity cell width. This cell width, set at 0.75 m/s, corresponds to the integration of 512 received pulses. As a result, the maximum achievable Improvement Factor (IF) is consistently lower than that of a SwarmSAR configuration with shorter baselines. Moreover, the drop in IF not only reduces performance but also complicates target detection. This is because, when each satellite measures a different radial velocity, it becomes non-trivial to determine whether the multiple angle-velocity detections correspond to the same target [65].

The results presented in the previous chapter, based on a velocity cell width of 0.75 m/s, indicate that baselines of 25 meters or less—which are unfeasible from an engineering perspective—enable the system to achieve the theoretical maximum interferometric factor (IF), which includes the full array processing gain and a single detection for all the satellites. However, in a SwarmSAR system, it is desirable to retain the flexibility of using baselines of several hundred meters while still achieving good performance with the STAP algorithm under such conditions. It is worth noting that the simplest solution would be to increase the velocity cell width as the baseline increases. However, this approach comes at the cost of reduced velocity resolution, which is not desirable. In particular, it would also degrade the angle resolution, significantly affecting the accuracy of target localization.

For this reason, in this chapter we propose an approach to address this issue without compromising either velocity or angle resolution. To the best of our knowledge, the approach proposed in this work has not been previously explored in the literature. This may be attributed to the fact that most implementations of STAP in spaceborne systems described in the literature rely on multiple channels within a single satellite—a configuration that has shown strong performance with conventional STAP techniques.

The key challenges we aim to address and overcome with this approach are as follows:

5.2. Methodology 43

1. Target radial velocity and angle of arrival is different for each satellite, which makes STAP not to be optimal and requires complex adaptation.

- 2. Different azimuth compression (motion compensation) for each satellite.
- 3. Very large number of observations due to large separations and high PRF, which presents a challenge for covariance matrix estimation.

### 5.2. Methodology

This section introduces the methodology of the proposed approach to deal with large baselines in a SwarmSAR system. The goal is to obtain a single angle-velocity detection per satellite in order to achieve array processing gain and to prevent multiple detections for the same target. For this reason, the approach is based on waiting for the satellites to get to a certain position to start taking measurements. The core idea is that the angle of arrival of each received pulse must be identical at each satellite. This ensures that the Doppler velocity measured from the reflections remains consistent across all satellites. This is because, when each satellite observes the same angle of arrival during its integration interval, the velocity component induced by the platform's motion is identical among all satellites. Similarly, the radial velocity component caused by the target's motion relative to the ground will also be consistent. This is based on two key assumptions: first, that the target maintains a constant radial velocity throughout each satellite's integration interval; and second, that the target's motion relative to the range is sufficiently small, allowing the angle of arrival to be considered constant during the time required for the satellites to begin data acquisition. Fig.5.1 illustrates the workflow of the proposed approach. Each step will be discussed in more detail in the following subsections.



Figure 5.1: Workflow of proposed approach for STAP in a SwarmSAR system

#### 5.2.1. Select same observation geometry

To ensure that the Doppler velocity measured from the reflections remains consistent across all satellites, it is necessary for the satellites to share the same observation geometry. To achieve this, it is necessary to wait until the virtual node of each bistatic pair—or the satellite itself in the monostatic case—reaches a designated reference position. This reference is defined in this project as the starting position of the virtual node associated with the bistatic pair whose receiver is located furthest from the target. Once this position is reached, data acquisition must begin for subsequent use in the STAP implementation. Consequently, the initial acquisition time will differ for each satellite. Since the initial measurement time differs for each satellite, this approach involves restructuring the traditional radar data cube—typically organized by fast time, slow time, and channel count. Consequently, for a given pair of slow and fast time indices, the samples across different channels no longer correspond to the same time instant.

Fig. 5.2 illustrates this setup for a configuration with three satellites and a single transmitter. In this example, Satellite 3 is positioned furthest ahead, and its initial time instant is taken as the reference. From this point, the relative time offsets for the other virtual nodes  $(S_{12},\ S_1)$  are calculated so that they reach the position of the virtual node of the bistatic pair formed by Satellite 1 and Satellite 3  $(S_{13})$  at the reference time. Therefore, during data collection, the trajectory of the virtual node is identical across all bistatic pairs. In the monostatic case, the trajectory of the transmitting satellite aligns with the position of the virtual nodes from the bistatic configurations. It is important to note that 'starting data acquisition' refers specifically to the collection of data intended for STAP processing. Satellites may continue acquiring measurements at other times for different operational purposes. The key steps required to implement the same observation geometry are as follows:

5.2. Methodology 44

1. Set the virtual node corresponding to the bistatic pair with the most distant satellite as the reference

- 2. Wait for the remaining virtual nodes to reach the position of the reference node
- 3. Begin STAP data acquisition at each receiver satellite when its corresponding virtual node reaches the reference position
- 4. Stop STAP data acquisition once the number of pulses specified for the integration interval has been collected.

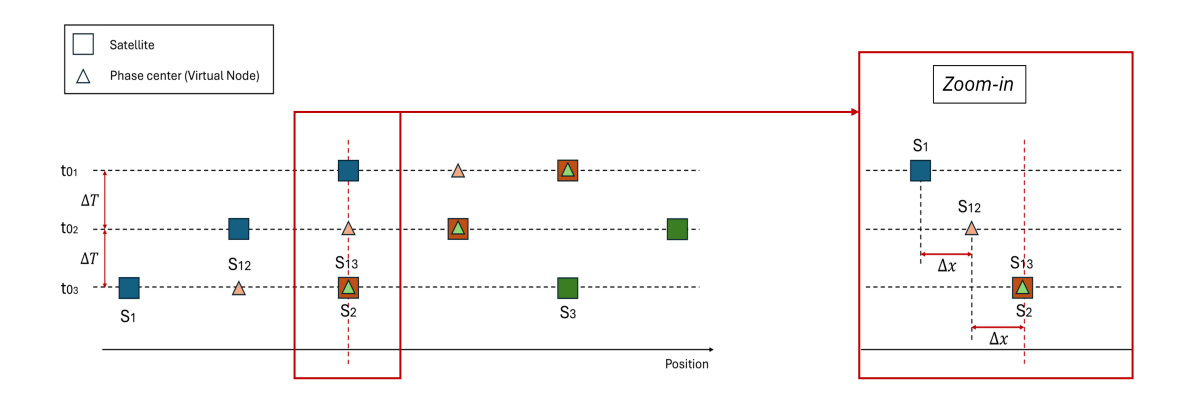


Figure 5.2: Illustration of the different time instants at which each satellite must begin acquiring measurements in the proposed approach ( $t_{0_3}$  is the starting time for satellite 3,  $t_{0_2}$  satellite 2 and  $t_{0_1}$  for satellite 1). The difference between the initial time instants of the various satellites is denoted by  $\Delta T$ . Satellite 1 is the transmitter. The red dotted line marks the position of the virtual node of the bistatic pair corresponding to the receiver that is scheduled to start recording reflections at that moment. On the right, a zoomed-in view along the red dotted line highlights the virtual baseline  $\Delta x$ 

#### 5.2.2. Apply same azimuth compression

Once the data is collected, each satellite applies the same azimuth compression (motion compensation), as they now observe identical angles of arrival for the received pulses within the integration nearly interval. Azimuth compression is performed with respect to the center of the Area of Interest (AoI). Specifically, eq.2.11 is applied using reference ranges corresponding to the center of the defined grid (see Fig.3.6b). We assume the integration interval is sufficiently short relative to the target's velocity, such that the targets do not undergo range cell migration.

#### 5.2.3. Estimate interference covariance matrix

The interference covariance matrix is estimated using a sample covariance approach, as defined in eq.4.4. In this context, each sample used for averaging corresponds to a space-time data vector associated with a single range cell. When the number of samples approaches infinity, the sample covariance matrix converges to the true interference covariance matrix. Although the total number of samples (370) is significantly smaller than the number of observations (1536), It still exceeds the number of independent clutter components (approximately 90), corresponding to the number of dominant eigenvectors, as demonstrated in Section 4.3.2. This suggests that the sample-based estimation method provides a sufficiently reliable approximation.

To implement the STAP weight vector (eq.2.24), inversion of the interference covariance matrix is required. This is achieved through orthogonal projection onto the clutter subspace, which involves selecting the eigenvectors corresponding to the largest eigenvalues of the estimated interference covariance matrix. This is done through the calculation of the threshold. A detailed explanation of this method is provided in section 4.2.1. The results presented throughout Chapter 4 demonstrate the efficiency of this step in the context of a SwarmSAR system.

5.2. Methodology 45

#### 5.2.4. Update steering vector

To correctly implement STAP in this context, it is essential to derive a new analytical expression for the phase difference between channels. This need arises because, for a given pair of slow and fast time indices, the samples across satellites do not correspond to the same time instant anymore, since each satellite begins data collection at a different initial time. As a result, the phase difference between adjacent channels no longer follows the conventional expression described in eq. 2.19.

Instead, it is influenced by the displacement of the target during the time delay  $\Delta T$  each satellite experiences before beginning its measurements. Therefore, it depends on the target's velocity. Additionally, the phase difference is affected by the variation in the positions of the virtual nodes at the start of data collection. In practice, these positions are not exactly the same across satellites when measurements begin. This discrepancy arises because the timing of data acquisition is constrained by the PRF, which limits the flexibility in synchronizing the start of measurements. Specifically, the positions of the virtual nodes  $S_{13}$ ,  $S_{12}$ , and  $S_{1}$  in Fig. 5.2 at their respective initial data acquisition times (t03, t02, t01), indicated by the red dotted line, do not exactly coincide. These positional differences  $\Delta x$  act as a *virtual baseline* since we can interpret each virtual node as an array element. As a result, the phase difference between adjacent channels also depends on the angle of arrival.

Furthermore, due to the system geometry, the positions of the virtual nodes do not lie along a straight line. As a result, the array formed is non-linear, which must be taken into account when analyzing the phase differences between adjacent virtual nodes. To account for this issue, we have to introduce an additional delay term which corresponds to the distance by which a given virtual node deviates from a reference straight line  $\delta_{ij}$ . This reference straight line corresponds to the velocity vector, as it defines the direction of arrival. This correction ensures that phase differences are accurately modeled despite the non-linear geometry of the array. The following equation represents the phase difference between two adjacent virtual nodes. Note that the number of unknowns  $(v_t, \theta)$  does not increase compared to the conventional approach.

$$\Delta\phi_{ij} = \frac{4\pi}{\lambda} (\Delta T_{ij} \cdot v_t + \Delta x_{ij} \cdot sin(\theta) + \delta_{ij})$$
(5.1)

where  $v_t$  is the target velocity,  $\theta$  is the angle of arrival,  $\Delta x_{ij}$  is the virtual baseline or distance between virtual nodes in the integration interval, and  $\Delta T_{ij}$  denotes the time difference between the arrivals of two virtual nodes at the position where data collection begins, and it is always an integer multiple of the PRF. Regarding,  $\delta_{ij}$  is the geometric offset of virtual node j from the projection onto the velocity vector, relative to the virtual node j. Note that the first two terms in this expression can be interpreted as follows: the second term represents the conventional phase difference between elements of a uniform linear array (ULA), where each element corresponds to a virtual node; the first term accounts for the target's displacement during the time each satellite takes to reach the reference position and initiate data acquisition. Additionally, in the specific case of uniform baselines, each  $\Delta T_{ij}$  and  $\Delta x_{ij}$  is identical for every pair of adjacent virtual nodes.

In the case of uniform baselines, the term  $\delta_{ij}$  becomes negligible for two main reasons. First, non-linear array configurations typically result from the presence of very large baselines, which are generally associated with non-uniform configurations—for example, when one satellite is positioned significantly farther away than the others. As the distance between satellites increases, the corresponding virtual nodes deviate more noticeably from the reference straight line defined by the velocity vector, leading to an increase in the value of  $\delta_{ij}$ . In terms of along-track and cross-track positioning, a larger inter-satellite distance—particularly between the first and the most distant satellite—results in a greater cross-track component in the position of the corresponding virtual node.

Fig. 5.3 shows the initial positions of three virtual nodes—corresponding to a SwarmSAR system with three satellites (two bistatic and one monostatic)—for both a uniform baseline scenario with 450 meters spacing and a non-uniform baseline scenario, where the distance between the transmitter and the adjacent receiver is 450 meters, and the distance between that receiver and the more distant one is 700 meters. The initial positions of the three virtual nodes are expressed in terms of along-track and cross-track coordinates, with the first virtual node serving as the reference point, located at coordinates

(0,0). This configuration is also the one analyzed in the performance evaluation for non-uniform baselines. Note that the position of the second virtual node remains the same in both configurations, as the distance between the first two satellites is identical. Additionally, the second reason why the term  $\delta_{ij}$  becomes more significant in non-uniform baselines is that accurate phase estimation is even more crucial in such configurations. This is because non-uniform spacing introduces additional complexity in the array's response pattern, making it more sensitive to phase errors [66].

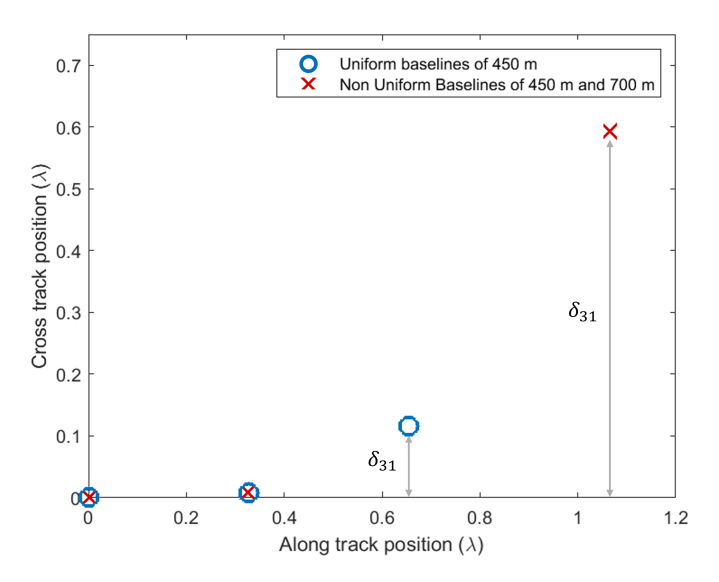


Figure 5.3: Virtual Node Separations During the Integration Interval for Uniform (450 m) and Non-Uniform Baselines (450 m and 700 m). The geometric offset of virtual node 3 with respect to the virtual node 1 is represented in the figure as  $\delta_{31}$ . Note that  $\delta_{21}$  would be negligible for both uniform and non-uniform baselines configurations

#### 5.2.5. Apply STAP

After computing the inverse of the interference covariance matrix—incorporating the orthogonal projection onto the clutter subspace—and updating the steering vector, we can apply the STAP optimal weight vector (eq. 2.24) to the received data. The target's velocity and angle of arrival are the two unknown parameters that must be estimated. This is achieved by searching over all possible values with a step size smaller than the first ambiguity. The pair that yields the highest  $SCNR_{out}$  is taken as the estimated target velocity and angle of arrival for the target under test.

## 5.3. Proposed Approach Results

To evaluate the effectiveness of this approach in implementing STAP in a SwarmSAR system, we perform simulations for both uniform and non-uniform baseline scenarios. The SwarmSAR system is configured to include three satellites, with only one functioning as the transmitter, as shown in Fig. 3.1. For each baseline configuration—uniform and non-uniform—we begin with a practical implementation. In this setup, a single target with a given velocity and position is considered, and the objective is to detect it and estimate its range, velocity, and angle of arrival. To achieve this, we implement the STAP weight vector following the workflow illustrated in Fig. 5.1. We evaluate the system over various target velocities and angles of arrival by computing the space-time steering vector  $v(\theta, f_t)$  from eq. 2.18, where the spatial steering vector now also depends on the target velocity, expressed as  $a(v_t,\theta)=e^{j\Delta\phi_{ij}}$  with  $\phi_{ij}$  following eq.5.1. After evaluating the  $SCNR_{out}$  across various angles of arrival and target velocities, the pairs yielding the highest  $SCNR_{out}$  are selected as the estimated angle and velocity.

After estimating the target parameters, we perform a performance evaluation for each baseline configuration. In this step, we compute the IF, which indicates the maximum improvement in SCNR for a target at a given position and velocity. Additionally, we calculate  $SCNR_{Loss}$  for different pairs of angle of arrival and target velocity, which quantifies the deviation of the obtained SCNR from the theoretical expected value. For more details, refer to section 4.1.

#### 5.3.1. Uniform Baseline Results

This section examines a specific case of a SwarmSAR configuration with uniform baselines with the following parameters Table 5.1 and the ones used for the conventional STAP approach, such as the  $SNR_{in}$  (Table 4.2). The radar system parameters used in the simulations are consistent with those employed throughout the project and are highlighted in Table 3.1. A baseline of 450 meters was selected as it represents a feasible distance that a SwarmSAR system could realistically support. The virtual baseline  $\Delta x$  of 0.031 meters represents the minimum achievable value, constrained by the PRF, since transmissions can only occur at discrete intervals that are integer multiples of the PRF. Since this distance is small compared to the wavelength, as it is equal to 0.32  $\lambda$ , and the angles of arrival are below 0.2 degrees (as defined by the grid dimensions), the third term in eq.5.1 becomes negligible.

With regard to  $\Delta T$ , it represents the time required to travel 225.03 meters, which is approximately half of the 450 meter baseline. This represents the relative displacement each satellite must achieve with respect to its adjacent counterpart in order to align their respective virtual nodes—formed by the bistatic pair with the transmitter—to the reference position. This is illustrated in Fig. 5.2, where it can be observed that half the baseline is covered between the start times of data collection for each satellite. The reason it does not exactly correspond to the time required to travel half the baseline (225 meters) in the simulation parameters is that data collection does not start precisely at the reference position, due to the inherent constraint imposed by the PRF.

Parameter	Value
Number of Satellites	3
Number of Targets	1
Baseline	450 m
$\Delta T$	32.1 ms
$\Delta x$	$0.33 \lambda$

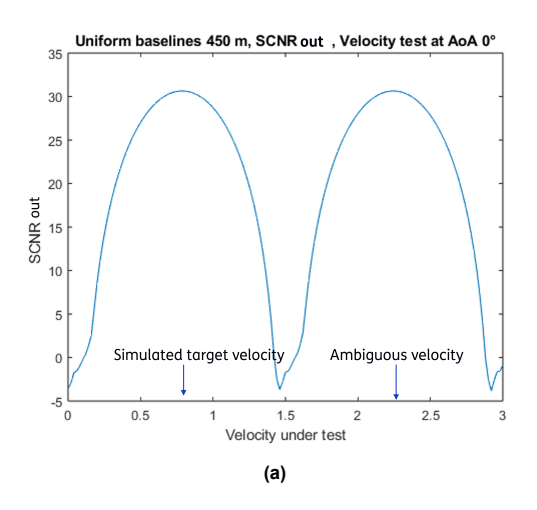
Table 5.1: Parameters for performance analysis of STAP proposed approach

First, the STAP weight vector (eq. 2.24) is implemented for different pairs of angle of arrival and target velocity, in order to estimate these parameters based on the maximum obtained  $SCNR_{out}$ . The true angle of arrival of the target under test is set to 0 degrees, and its true velocity is set to 0.75 m/s. Based on this setup, the results shown in Fig. 5.4a are obtained. In terms of velocity estimation, we fixed the angle of arrival at 0 degrees and try different velocity values, we observe a peak at 0.75 m/s, corresponding to the true value, but also a secondary peak at 2.21 m/s due to ambiguity. The resulting non-ambiguous interval is therefore 1.46 m/s. This occurs because, for certain target velocities, the phase difference between adjacent elements becomes ambiguous. The displacement of the target during the time each satellite takes to reach its data collection position influences the received phase difference between elements, as described by eq. 5.1. This can be validated by calculating the velocity that induces a phase shift of  $2\pi$  in eq. 5.1,assuming an angle of arrival of 0 degrees and a negligible  $\delta_{ij}$ . Accordingly, the non-ambiguous velocity interval is given by

$$v_{ambiguous} = \lambda/2\Delta T$$
 (5.2)

which using the parameters of this simulation yields in an ambiguous velocity of 1.46 m/s. Next, we analyze the angle estimation, fixing the velocity at 0.75 m/s and trying different angle values, with the results shown in Fig. 5.4b, where a peak is observed at the true angle of arrival of 0 degrees. It is important to note the relatively wide beamwidth in this case. The test was conducted using isotropic antennas on each satellite, with an equivalent array element spacing—corresponding to the distance between virtual nodes,  $\Delta x$ —set to  $0.33\lambda$ . No angular ambiguity is observed, as the virtual baseline  $\Delta x$  remains below  $0.33\lambda$ . Note that the step size used for the angles of arrival tested for the target under test at 0.75 m/s is 0.004 degrees, which is three times smaller than the first ambiguous angle (0.012 degrees) associated with the performance evaluation scenario. This is important to emphasize that the

absence of ambiguities in the angle test shown in Fig. 5.4b is not due to undersampling. In this case, angle ambiguities are absent because the term in eq. 5.1 representing the target displacement  $(\Delta T_{ij} \cdot v_t)$  is the only significant contributor at low angles of arrival and with a uniform baseline. In the current test, this term remains constant since only the angle of arrival varies. However, in the performance test conducted later (see Fig. 5.5a), both the angle and velocity vary, leading to the emergence of both velocity and angular ambiguities. However, further analysis is required to fully validate the system's response with respect to the angle of arrival. Based on the results, the parameter values associated with the highest  $SCNR_{out}$  values correspond to the true values of 0.75 m/s and 0 degrees.



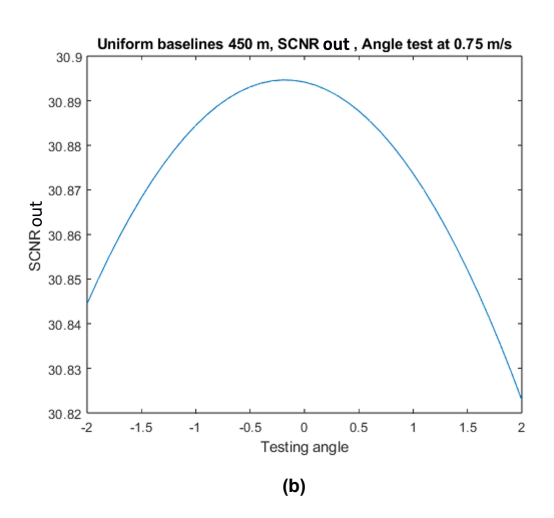


**Figure 5.4:** Implementation of STAP target velocity test (a) and angle of arrival test (b) for 450 meters baseline using the proposed approach

Next, we perform a performance analysis across various velocity and angle pairs. The results for the IF are presented in Fig. 5.5a, which reveals that we get multiple angle-velocity ambiguities. Notably, we see the ambiguity at 1.46 m/s and 0 degrees of angle of arrival that was validated with eq.5.1 before. This implies that a target with this velocity cannot be detected, as the IF factor is 0 dB—indicating that the SCNR has not improved following the implementation of STAP. To understand the remaining ambiguities, it is important to recall that the measured target velocity is the sum of the velocity induced by the platform's motion and the target's actual radial velocity relative to the ground, as described in eq. 2.17. For example, in Fig. 5.5a, the row corresponding to an angle of arrival of 0 degrees represents the target's true radial velocity relative to the ground, since no additional velocity component from platform motion is introduced in this case. However, the column corresponding to 0 m/s does not imply that the target is stationary relative to the ground. Instead, it indicates that the measured velocity from the satellite's perspective is 0 m/s. For instance, at an angle of 0.012 degrees, a stationary object—such as ground clutter—would exhibit a measured velocity of 1.46 m/s due to platform motion. This induced velocity corresponds to  $v_p \cdot \sin(\theta)$ , where  $v_p$  is the platform velocity (7000 m/s) and  $\theta$  is the angle of arrival.

Therefore, to measure a total velocity of 0 m/s, the target must have a radial velocity of -1.46 m/s relative to the ground. This compensates for the induced velocity from platform motion at an angle of 0.012 degrees. Since -1.46 m/s corresponds to the first ambiguous velocity, an ambiguity also appears at this angle of arrival for a measured velocity of 0 m/s. Similarly, the other angle-velocity ambiguities arise when the target's radial velocity relative to the ground combines with the platform-induced velocity to produce a total measured velocity (shown on the velocity axis) that is a multiple of 1.46 m/s. It is also important to note that this behavior occurs because the second term in eq. 5.1 is negligible. This is due to both the small angles of arrival and the short virtual baseline. If the virtual baseline were larger, the second term would contribute significantly to the phase difference. As a result, the target's radial velocity required to produce, for example, a total measured velocity of 0 m/s (when combined with the platform-induced velocity) would be smaller. This would cause the angle ambiguity at 0 m/s to appear at a smaller angle, and it would no longer necessarily align with a multiple of 1.46 m/s.

When comparing this approach to the conventional one, the number of ambiguities remains the same.

In the conventional STAP, ambiguities arise by equating the phase difference between adjacent ULA elements (as described in Eq. 2.14) to  $2\pi$ , leading to the first ambiguous angle at

$$\theta_{ambiguous} = \arcsin(\lambda/d)$$
 (5.3)

where d is the baseline. For a baseline of 450 meters, this results in a first angle ambiguity of approximately 0.012 degrees, which corresponds to an ambiguous velocity of 1.46 m/s using  $v_t = v_p \sin(\theta)$ . This is identical to the ambiguous velocity obtained using the proposed method in this chapter, by equating Eq. 5.1 to  $2\pi$  and solving for velocity. This is because the phase difference between adjacent channels remains unchanged, even if we wait for the satellites to reach a specific position before collecting measurements. As a result, this approach does not replicate the behavior of a system with a shorter baseline. The effects of a large baseline—particularly in terms of ambiguities—cannot be avoided. Even though measurements are taken at specific satellite positions, the results are not equivalent to those of a SwarmSAR system with a baseline of  $\Delta x$ ; the influence of the large baseline persists. Note that in the conventional approach, ambiguity is introduced through the angle and then translated into velocity. In contrast, the proposed method determines the ambiguity directly in velocity, which is subsequently mapped to an angle ambiguity.

Although the ambiguities cannot be reduced, this approach achieves a maximum IF of approximately 31 dB. The theoretical maximum IF, for an input  $SCNR_{in}$  of 0 dB, corresponds to the sum of the integration gain and the array processing gain, which equals 31.86 dB. It's important to note that in the conventional approach, achieving this level of IF would not be possible, as the spatial samples could not be coherently combined, since each satellite would be observing the same target with different velocities. Figure 5.5b presents the  $SCNR_{Loss}$  values across all angle-velocity pairs. The results indicate that the loss is more pronounced when the target lies closer to the clutter subspace, underscoring the importance of precise estimation in such cases. Conversely, for angle-velocity pairs located farther from the clutter subspace (or notch), the  $SCNR_{Loss}$  approaches zero. This demonstrates that the signals from the different satellites have been successfully coherently combined.

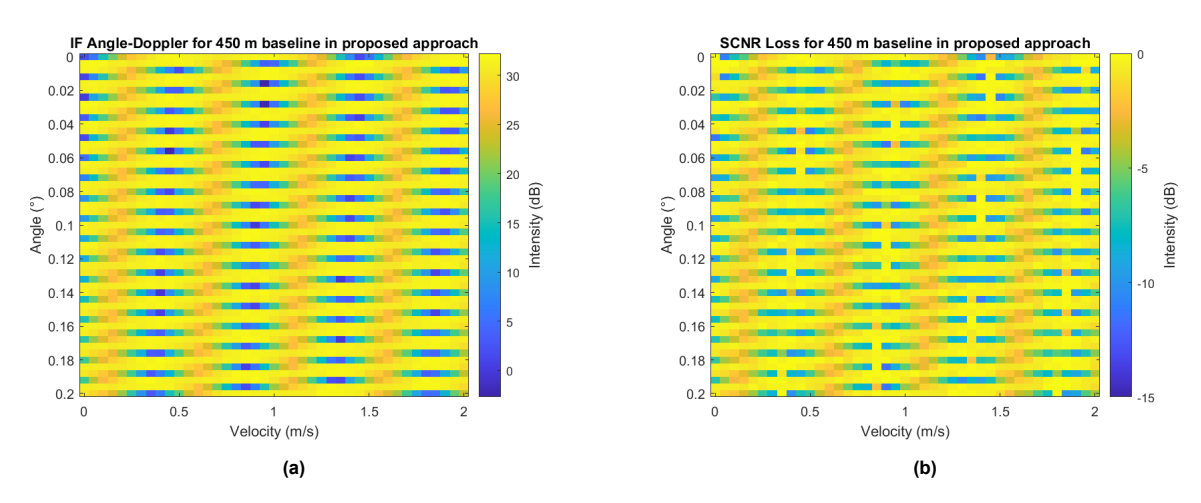
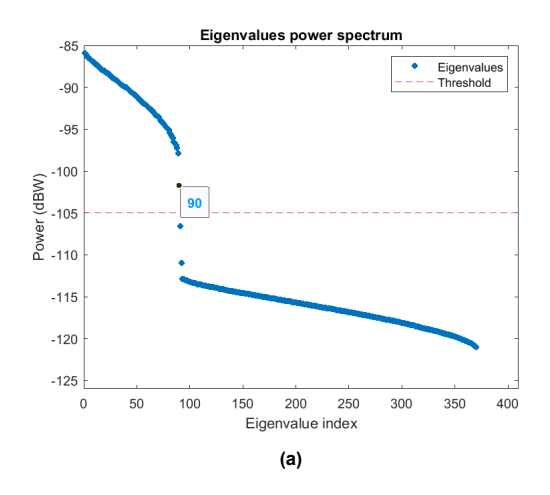


Figure 5.5: Angle-Doppler Improvement Factor (a) and  $SCNR_{Loss}$  (b) for 450 meters baseline using the proposed approach

It is also insightful to examine the eigenvalues obtained using this approach in comparison to the conventional method. Fig.5.6a shows the eigenvalues corresponding to the interference covariance matrix. Notably, the number of dominant eigenvalues selected by the threshold (90) is lower than that observed in the conventional approach with the smallest baseline (95 for a 50-meter baseline). This reduction is due to the decreased number of independent observations, as the trajectories of the virtual nodes are fully overlapped, since we wait until they are in the same position to start taking measurements in each satellite. Fig.5.6b shows the eigenvalues of the true interference covariance matrix, obtained using eq.4.7. The results confirm that the estimation was sufficiently accurate, as the number of dominant eigenvalues identified using the true covariance matrix (91) closely matches those obtained from the estimated matrix.



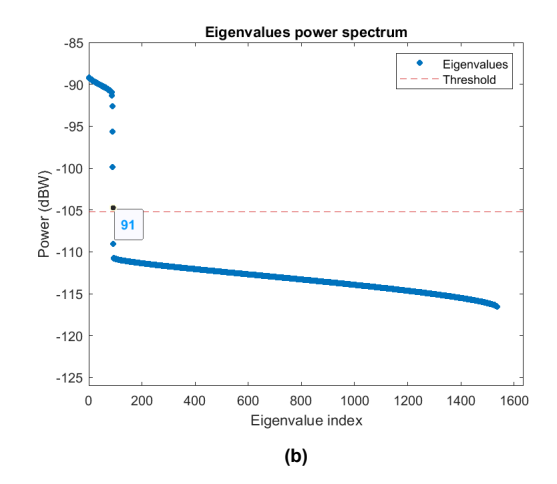


Figure 5.6: Power spectrum of (a) obtained eigenvalues and (b) true eigenvalues for 450 meter baseline in the proposed approach

#### 5.3.2. Non-Uniform Baseline results

This section explores a more general scenario in which the baselines between satellites are non-uniform, reflecting a more realistic configuration where inter-satellite distances vary. The concrete parameters for this case are highlighted in Table.5.2. With respect to the uniform baseline configuration, the distance between the transmitter and the farthest satellite increases by 250 meters. Additionally, we observe that both the temporal separation  $\Delta T$  and spatial separation  $\Delta x$  vary across each pair of adjacent virtual nodes.

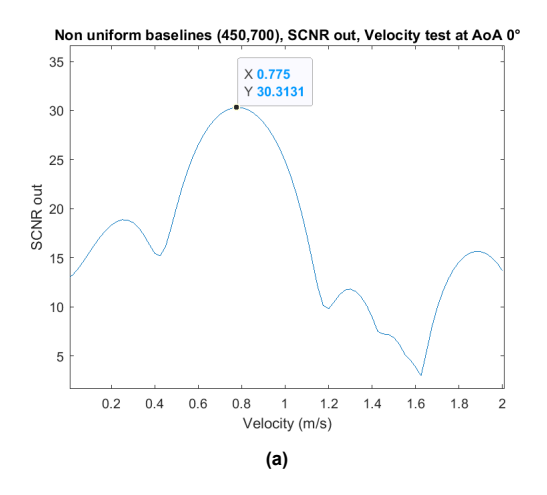
Parameter	Value
Number of Satellites	3
Number of Targets	1
Baseline (TX - RX2)	450 m
Baseline (TX - RX3)	700 m

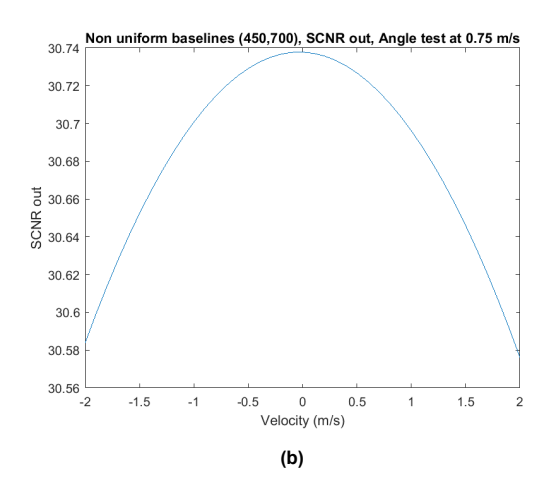
Parameter	Value
$\Delta T_{12}$	32.1 ms
$\Delta T_{23}$	49.9 ms
$\Delta x_{12}$	$0.33 \lambda$
$\Delta x_{23}$	$0.75 \lambda$
$\delta_{12}$	$0.008 \lambda$
$\delta_{23}$	$0.59 \lambda$

Table 5.2: Parameters for performance analysis of STAP proposed approach

As in the analysis of the uniform baseline configuration, we begin by implementing the STAP weight vector (eq. 2.24) for different pairs of angle of arrival and target velocity, in order to estimate these parameters based on the maximum obtained  $SCNR_{out}$ . The true velocity of the target is set to 0.75 m/s, and the true angle of arrival is set to 0 degrees. Fig.5.7a shows the velocity test at 0 degrees of angle of arrival. As expected, the estimated velocity aligns with the target's true velocity, with a peak observed at 0.75 m/s. However, the shape of the velocity response has noticeably changed. This behavior arises from the non-uniform sampling in both the spatial and temporal domains.

During the STAP interval, the separations between virtual nodes ( $\Delta x_{12}, \Delta x_{23}$ ) are not constant, and different time instants ( $\Delta T_{12}, \Delta T_{23}$ ) are required for the satellites to reach their respective data acquisition positions. Additionally, no velocity ambiguity is observed, as the response shows a single peak at the target's true velocity of 0.75 m/s. Regarding the angle test, Fig. 5.7b presents the results obtained by selecting different angles of arrival while fixing the target velocity at 0.75 m/s. We observe that, despite the non-uniform baseline, the angle response is approximately the same as that obtained in the uniform baseline case (Fig. 5.4b). Again, further investigation is needed to validate the angle response using the proposed approach. Although the virtual baseline is now larger—specifically,  $\Delta x_{23} = 0.75 \ \lambda$ —no significant change in the angle response is observed.





**Figure 5.7:** Implementation of STAP target velocity test (a) and angle of arrival test (b) for non uniform baselines, 450 meters and 700 meters, using the proposed approach

Regarding the performance analysis of the proposed approach in the implementation of STAP in non uniform baselines, Fig.5.8 presents a direct comparison of the IF at 0° angle of arrival for different velocities, considering both uniform and non-uniform baseline configurations. The most noticeable observation is the absence of ambiguity at 1.46 m/s, where a prominent peak appears, closely aligning with the theoretical maximum IF of approximately 31.86 dB. In contrast, two minima are observed at 1.125 and 1.72 m/s. However, these minima have significantly higher values compared to the minimum observed in the uniform baseline case, indicating that the suppression of certain velocities is less pronounced—and therefore less problematic—in the non-uniform configuration.

Note also that the notch slope is steeper in the non-uniform baseline case, due to the greater total separation between the nearest and the furthest satellite. The reason for the displacement and reduction of the minima is the non uniform sampling both in space and in time. During the STAP interval, the separations between virtual nodes  $(\Delta x_{12}, \Delta x_{23})$  are not constant, and different time instants  $(\Delta T_{12}, \Delta T_{23})$  are required for the satellites to reach their respective data acquisition positions. Further investigation is needed to fully understand the resulting shape of the IF in non-uniform baseline configurations. This line of research has the potential to lead to an analytical expression capable of predicting the displacement of nulls as a function of non-uniform inter-satellite distances, across different combinations of angle of arrival and target velocity.

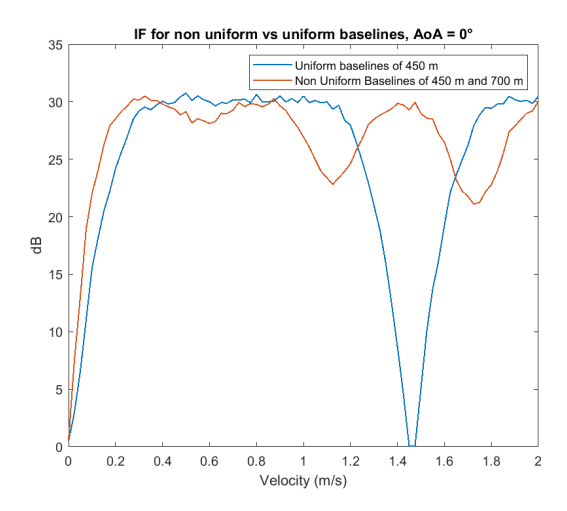


Figure 5.8: Comparison of Improvement Factor at 0° Angle of Arrival for Uniform (450 m) and Non-Uniform Baselines (450 m and 700 m)

Furthermore, Fig.5.9a presents the IF factor not only at 0 degrees but also across various combinations of angle and velocity. The figure illustrates how the positions of the minima shift with different angles of arrival. As the angle increases, the platform's motion induces a greater component of velocity along the line of sight, meaning that a lower target velocity is required to produce the same minimum. This interpretation is consistent with the reasoning we have applied throughout the project in analyzing these plots. In addition, Fig.5.9a shows the  $SCNR_{Loss}$  across various angle-velocity pairs. As observed previously, the largest losses occur for combinations that lie closer to the clutter subspace, where having an accurate interference covariance matrix has the most significant impact. Apart from these specific pairs, the observed  $SCNR_{Loss}$  remains relatively low—around 1 dB—which indicates that our estimate of the interference covariance matrix is sufficiently accurate, and that the coherent combination of samples from different satellites is working effectively.

Finally, Fig.5.10 shows the eigenvalues obtained through the estimate of the interference covariance matrix as well as the eigenvalues obtain with the true interference covariance matrix. As one could already deduce, the number of dominant eigenvalues (related to the clutter subspace) has not change with respect to the uniform baselines. This is because the observation window remains unchanged; the only difference is that one satellite must wait longer to reach its data acquisition position. However, in the proposed approach, this additional waiting time does not affect the overall length of the observation window, which remains constant. As a result, the number of independent observations—and consequently, the number of dominant eigenvalues—also remains unchanged. Table 5.3 presents the results of the proposed approach for both uniform and non-uniform baseline configurations. The MDV (Minimum Detectable Velocity) is not highlighted, as it would be even lower than 0.15 m/s—the MDV observed at 100 m in Table 4.3. In practical scenarios, ground clutter often exhibits some motion due to environmental factors such as wind, making extremely low MDV values less critical. Regarding the first ambiguous velocity and angle in the non-uniform baseline case, these are not considered ambiguous in this context, as the corresponding minima exhibit an IF (Interference Factor) of 25 dB. This indicates that targets at these velocities can still be detected with high efficiency.

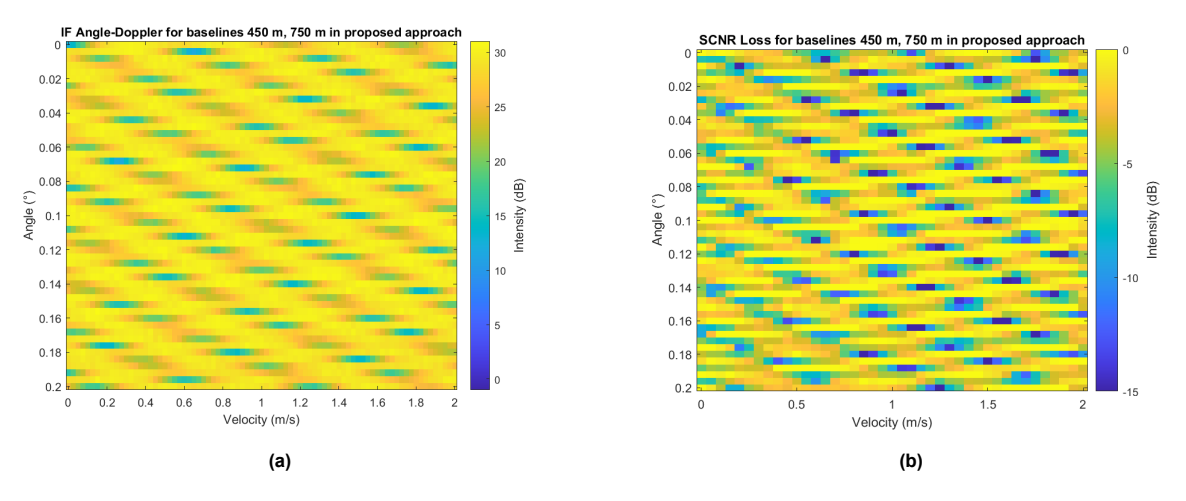
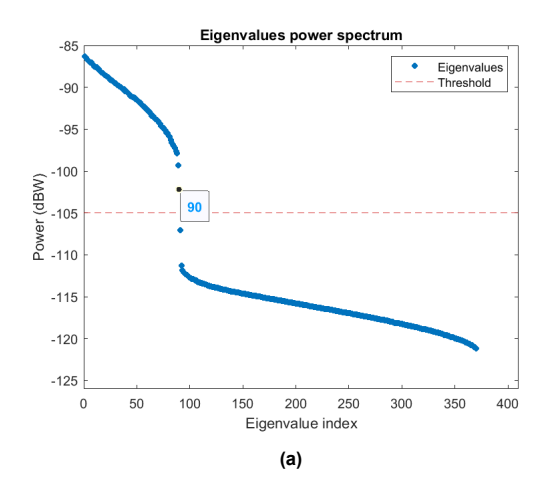


Figure 5.9: Angle-Doppler Improvement Factor (a) and  $SCNR_{Loss}$  (b) for non uniform non uniform baselines, 450 meters and 700 meters, using the proposed approach

Baseline (m)	First ambiguos velocity (m/s)	First ambiguos angle (°)	Number of dominant eigenvalues (out of 1536)
450	1.46	0.012	90
450, 700	-	-	90

Table 5.3: Proposed approach results

5.4. Summary 53



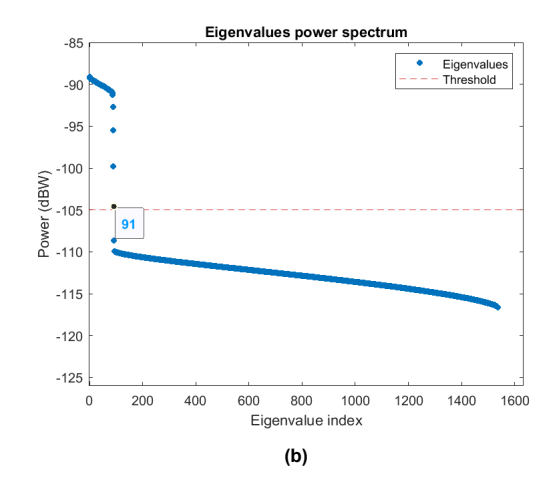


**Figure 5.10:** Power spectrum of (a) obtained eigenvalues and (b) true eigenvalues for non uniform baselines, 450 meters and 700 meters, using the proposed approach

### 5.4. Summary

This chapter proposed a methodology to prevent the measurement of different radial velocities for a single target—one per satellite—which occurs when using large baselines (greater than 100 m). In such cases, each satellite observes the target from a sufficiently different angle of arrival, resulting in variations in the measured radial velocity that exceed the velocity cell width. In addition to the challenge of obtaining different range-velocity detections—which makes it non-trivial to determine whether they correspond to the same target—the lack of coherent combination of spatial samples led to a reduction in the Improvement Factor by approximately 5 dB. The proposed approach addresses this issue by ensuring consistent velocity estimation across satellites despite the geometric disparities.

This approach involves waiting for the virtual nodes of each bistatic pair (with the satellite itself acting as the transmitter in its own pair) to reach the starting position of the virtual node associated with the bistatic pair whose receiver is located furthest away. This ensures that the Doppler velocity measured from the reflections remains consistent across all satellites. In addition, it introduces a method for computing the inverse of the interference covariance matrix based on orthogonal projection onto the clutter subspace. The approach also proposes an updated formulation of the steering vector to account for the additional phase differences between adjacent channels, which arise from the target's displacement during the time required for the satellites to reach their respective data acquisition positions. The results demonstrate that the proposed approach successfully achieves the objective of measuring the same target velocity across all satellites, thereby enabling the realization of array processing gain through coherent processing, both for uniform and non-uniform baseline configurations. In contrast to uniform baselines, which preserve the ambiguities as in the conventional approach, the results with non-uniform baselines demonstrate that the ambiguities are resolved. However, it is important to acknowledge that several ideal assumptions were made, including perfect synchronization between satellites, error-free satellite position estimates, and stationary clutter conditions.

## Conclusion and Future Lines

This chapter begins with the conclusions, summarizing the work carried out throughout the thesis and addressing the research question presented in Chapter 1. It then outlines potential directions for future research.

#### 6.1. Conclusion

This thesis analyzes the performance of a SwarmSAR configuration consisting of three satellites. It evaluates three different inter-satellite baselines—25 meters, 50 meters, and 100 meters. The results show that the primary limitation of applying STAP in a SwarmSAR system lies in the occurrence of angular ambiguities caused by large baselines. These angular ambiguities also lead to velocity ambiguities due to the coupling between the angle of arrival and the measured ground velocity, which is influenced by platform motion. As the baseline increases, the number of ambiguities also increases, which makes the non-ambiguous intervals for both target velocity and angle of arrival become shorter, causing targets with certain angle-velocity combinations to become undetectable. However, the results also highlight a key advantage of using large baselines: the ability to detect targets with lower velocities. Increasing the baseline reduces the MDV, which improves sensitivity to slow-moving targets.

An additional challenge emerges when using large baselines (greater than 100 meters), as each satellite measures a different radial velocity for the same target, often exceeding the velocity cell width. This leads to two main issues: first, the system cannot achieve array processing gain, resulting in reduced overall performance; second, it may produce multiple detections. The latter poses a non-trivial problem, as it becomes difficult to determine whether these multiple angle-velocity detections correspond to the same target. Addressing these challenges is of particular interest, especially since, from an engineering perspective, developing SwarmSAR systems with short baselines (less than 100 meters) is not practically feasible.

Therefore, Chapter 4 introduces an approach designed to overcome these limitations by presenting the necessary methodology for implementation within a SwarmSAR system. The core idea is to ensure that all satellites share the same observation geometry, thereby avoiding discrepancies in the measured target radial velocity across different satellites. This is achieved by waiting for the virtual nodes of each bistatic pair (with each transmitter satellite acting as the virtual node in its own pair) to reach a predefined reference position. To implement this approach efficiently, the target steering vector must be updated with respect to the conventional method, accounting for the target's displacement during the time required for the satellites to reach their respective data acquisition positions.

The implementation of this approach in both uniform and non-uniform baseline configurations demonstrates its efficiency: all satellites measure a single target velocity, and array processing gain is achieved. The obtained results align more closely with the theoretical predictions as the target velocity—angle of arrival pairs move further away from the clutter subspace. This is because more accurate estimation is required as the target approaches the clutter subspace, which in turn necessitates a larger number

6.1. Conclusion 55

of samples when estimating the interference covariance matrix. In addition, results from the uniform baseline configuration show that the number of ambiguities remains the same as in the conventional approach. In contrast, the non-uniform baseline configuration benefits from non-uniform sampling in space and time, which effectively mitigates these ambiguities. Altogether, the work presented in the preceding sections provides answers to the research questions outlined in Chapter 1. The answers to the sub-research questions leading up to the main research question are as follows:

#### Can STAP be efficiently implemented in a SwarmSAR system?

In a multistatic spaceborne system topology such as SwarmSAR, STAP can be effectively implemented, with clutter suppression improving as the target moves further from the clutter subspace. This implies that the further a target is from the clutter subspace, the easier it becomes to detect. Since baselines in SwarmSAR are significantly higher than the wavelength, targets can be detected at relatively low minimum velocities—below 1 m/s—because they are already sufficiently separated from the clutter subspace. However, for baselines of a few hundred meters or more—which are the only feasible option from an engineering perspective—the efficiency of conventional STAP (Chapter 3) decreases by a factor proportional to the array processing gain.

#### How does the system geometry influence STAP performance in a SwarmSAR system?

The major limitation of the system geometry in SwarmSAR is the large baselines inherent to a satellite formation. Since each satellite is treated as an array element at reception, grating lobes arise because the spacing between elements is always larger than the wavelength. The larger the baseline, the larger the number of grating lobes and the smaller the non-ambiguous interval. These grating lobes cause angular ambiguities, which translate into velocity ambiguities due to the coupling between angle of arrival and target velocity caused by platform motion. As a result, multiple angle-velocity pairs appear within the clutter, making targets with those specific angle-velocity combinations impossible to detect.

#### What strategies can be used to better manage the configurations required in a SwarmSAR system?

When the baselines are sufficiently large (a few hundred meters), causing each satellite to measure a target velocity that differs by more than the velocity cell width, the efficiency of STAP decreases by a factor corresponding to the array processing gain. This occurs because the spatial samples cannot be coherently combined when calculating the target space-time steering vector for a specific target velocity. Moreover, not only is the array processing gain lost, but multiple detections of the same target occur—one per satellite—since the target space-time steering vector produces a detection for the target velocity measured by each satellite. Note that each of these detections has an SCNR lower than the theoretically expected value by a factor equal to the array processing gain. To make STAP optimal when this issue arises and to avoid complex adaptation for each velocity, we propose a strategy to obtain the same observation geometry from each satellite, ensuring that all satellites measure the same target parameters. This is achieved by waiting for the virtual nodes of each bistatic pair (with each transmitter satellite acting as the virtual node in its own pair) to reach a predefined reference position.

# • How is the performance of STAP going to be influenced by the topology of a multistatic spaceborne system with a single antenna per node, such as a SwarmSAR system?

Although a SwarmSAR system enables high-performance detection of targets outside the clutter subspace—even at low minimum velocities (below 1 m/s)—the main limitation to STAP performance in a Swarm-SAR topology is the presence of large baselines. These baselines introduce multiple angle-of-arrival and target velocity ambiguities, which degrade detection performance, as multiple angle-velocity combinations fall within the clutter subspace, making targets with those specific parameters impossible to detect. Additionally, when the baselines are large enough that each satellite measures a different target velocity—differing by more than the velocity resolution—the efficiency of STAP decreases by a factor equal to the array processing gain, and a separate detection is produced by each satellite. For this reason, we propose an strategy to get the same observation geometry in each satellite. The results from this approach show that when the baselines between satellites are non-uniform, apart from getting the array processing gain and only a detection per target, the ambiguities are resolved. It is also important to note that these results were obtained under several ideal assumptions, including perfect

6.2. Future Lines 56

synchronization and phase stability between satellites, accurate knowledge of satellite positions, and stationary clutter.

#### 6.2. Future Lines

Future research should focus on implementing STAP in SwarmSAR systems under more generalized scenarios. It is important to highlight that this thesis represents an initial attempt at integrating and analyzing STAP within a SwarmSAR framework. This preliminary approach required several idealized assumptions to assess the feasibility of efficient STAP implementation. For this reason, future studies should investigate how removing these assumptions affects the results.

First, it would be valuable to move beyond the assumption of clutter stationarity. In real-world scenarios, ground clutter is not perfectly stationary—it exhibits small variations over time. For example, wind can cause movement in grass or trees, introducing temporal changes in the clutter. This consideration is particularly relevant when applying the STAP approach proposed in this thesis. During the time required for the satellites to reach their data acquisition positions, the properties of the clutter may change. Such changes can degrade the estimation of the interference covariance matrix, as the samples collected by different satellites may exhibit slightly different statistical characteristics. Additionally, if multiple pulses are integrated, the initial and final samples acquired by a satellite may also differ in their statistical properties. Therefore, alternative approaches for estimating the interference covariance matrix may be required when the assumption of stationary clutter is no longer valid.

Next, assuming precise knowledge of the exact transmission time of the satellites is overly optimistic, given their high velocities and large distances. In practice, the transmission time is always an estimate. To study the impact of removing this idealization, one could model the PRF as a random variable. This randomness would reflect the uncertainty in the exact transmission time. Such variability could affect the accuracy of the interference covariance matrix estimation, as the statistical consistency between samples may be compromised. It may also affect the location of the resulting ambiguities. This randomness could also be applied to the satellites' exact positions, as it is not possible to obtain perfectly accurate measurements without some degree of error. Finally, incorporating phase noise—which is inherent to all oscillators—would improve the realism of the model. At the same time, moving beyond the flat Earth assumption becomes particularly relevant when considering larger baselines than those explored in this thesis.

In addition to removing idealized assumptions, it would also be valuable to further analyze the angle of arrival response obtained in the angle test used for target detection with the STAP approach proposed in this thesis for SwarmSAR systems. The shape of the angle response observed in these tests has not yet been validated. One possible direction for further study would be to increase the grid size, which would result in a higher maximum angle of arrival—beyond the current 0.2 degrees. This would make the angle to have a greater influence on the target steering vector, allowing for a more detailed investigation of its effects. This analysis could also provide insight into how the secondary lobes of the antenna pattern influence the results. Furthermore, a dedicated study should be conducted to better understand the positions of the local minima that arise when using non-uniform baseline configurations. Being able to predict the locations of these minima based on the specific values of the non-uniform baselines would be a valuable contribution.

- [1] Alberto Moreira et al. "A tutorial on synthetic aperture radar". In: *IEEE Geoscience and Remote Sensing Magazine* 1.1 (2013), pp. 6–43. DOI: 10.1109/MGRS.2013.2248301.
- [2] Joachim Ender. "Space-time processing for multichannel synthetic aperture radar". In: *Electronics & Communication Engineering Journal* 11 (Mar. 1999), pp. 29–38. DOI: 10.1049/ecej:19990106.
- [3] Alfonso Farina. "STAP for SAR". In: *Military Application of Space-Time Adaptive Processing* (2003).
- [4] James Ward. "Space-time adaptive processing for airborne radar". In: 1995 International Conference on Acoustics, Speech, and Signal Processing. Vol. 5. 1995, 2809–2812 vol.5. DOI: 10. 1109/ICASSP.1995.479429.
- [5] Lorenzo Iannini, Paco Lopez-Dekker, and Peter Hoogeboom. "A Highly Flexible and Scalable S-band SwarmSAR from Very Simple Nodes". In: 2020 IEEE Radar Conference (RadarConf20). 2020, pp. 1–6. DOI: 10.1109/RadarConf2043947.2020.9266527.
- [6] Stefan V. Baumgartner and Gerhard Krieger. "Chapter 18 Multi-Channel SAR for Ground Moving Target Indication". In: *Academic Press Library in Signal Processing: Volume 2*. Ed. by Nicholas D. Sidiropoulos et al. Vol. 2. Academic Press Library in Signal Processing. Elsevier, 2014, pp. 911–986. DOI: https://doi.org/10.1016/B978-0-12-396500-4.00018-1. URL: https://www.sciencedirect.com/science/article/pii/B9780123965004000181.
- [7] CE Livingstone et al. "RADARSAT-2 system and mode description". In: *Meeting Proceedings RTO-MP-SCI-150, Paper.* Vol. 15. 2005.
- [8] Tim J Nohara et al. "SAR-GMTI processing with Canada's Radarsat 2 satellite". In: Proceedings of the IEEE 2000 Adaptive Systems for Signal Processing, Communications, and Control Symposium (Cat. No. 00EX373). IEEE. 2000, pp. 379–384.
- [9] Delphine Cerutti-Maori, Ishuwa Sikaneta, and Christoph H Gierull. "Optimum SAR/GMTI processing and its application to the radar satellite RADARSAT-2 for traffic monitoring". In: *IEEE Transactions on Geoscience and Remote Sensing* 50.10 (2012), pp. 3868–3881.
- [10] Wolfram Bürger. "Space-Time Adaptive Processing: Fundamentals". In: *Advanced Radar Signal and Data Processing*. Vol. 2. 2006, pp. 6-1-6–14.
- [11] Z. Allahgholi Pour and Lotfollah Shafai. "An overview of latest advancements in displaced phase centre antenna (DPCA) techniques". In: 2013 USNC-URSI Radio Science Meeting (Joint with AP-S Symposium). 2013, pp. 22–22. DOI: 10.1109/USNC-URSI.2013.6715328.
- [12] A N Leukhin, A A Voronin, and V I Bezrodny. "Detection of moving targets in SAR". In: *Journal of Physics: Conference Series* 1096.1 (2018), p. 012049. DOI: 10.1088/1742-6596/1096/1/012049. URL: https://dx.doi.org/10.1088/1742-6596/1096/1/012049.
- [13] Junchi Liu. "SAR-GMTI Simulation of T72 Based on DPCA". In: 2022 14th International Conference on Signal Processing Systems (ICSPS). 2022, pp. 115–122. DOI: 10.1109/ICSPS58776. 2022.00026.
- [14] Sun Huadong, Zhang Lizhi, and Jin Xuesong. "Parameter Estimations Based on DPCA-FrFT Algorithm for Three-channel SAR-GMTI System". In: 2011 Fourth International Conference on Intelligent Computation Technology and Automation. Vol. 2. 2011, pp. 640–644. DOI: 10.1109/ICICTA.2011.445.
- [15] Zhongyu Li et al. "Dual-Channel DPCA technique in Bistatic Forward-looking SAR for moving target detection and imaging". In: *Proceedings of 2011 IEEE CIE International Conference on Radar*. Vol. 1. 2011, pp. 942–945. DOI: 10.1109/CIE-Radar.2011.6159696.

[16] Xianliang Pu et al. "GEO Spaceborne-Airborne Bistatic SAR Clutter Supression Using Improved DPCA Method". In: *IGARSS 2022 - 2022 IEEE International Geoscience and Remote Sensing Symposium.* 2022, pp. 559–562. DOI: 10.1109/IGARSS46834.2022.9884741.

- [17] Hui Wang et al. "Moving target detection method of the Ka FMCW SAR based on DPCA". In: 2017 Signal Processing Symposium (SPSympo). 2017, pp. 1–4. DOI: 10.1109/SPS.2017.8053670.
- [18] Katlego E. Mosito et al. "Detection, Tracking and Geo-location of Moving Targets in Airborne Radar Data using a DPCA GMTI Technique". In: 2022 IEEE Radar Conference (RadarConf22). 2022, pp. 1–6. DOI: 10.1109/RadarConf2248738.2022.9763912.
- [19] Ahmed Hussain et al. "Displaced Phase Center Antenna Processing For Airborne Phased Array Radar". In: 2021 International Bhurban Conference on Applied Sciences and Technologies (IBCAST). 2021, pp. 988–992. DOI: 10.1109/IBCAST51254.2021.9393224.
- [20] H.S.C. Wang. "Mainlobe clutter cancellation by DPCA for space-based radars". In: 1991 IEEE Aerospace Applications Conference Digest. 1991, pp. 1/1–128. DOI: 10.1109/AER0.1991.1545 20.
- [21] L. Lightstone, D. Faubert, and G. Rempel. "Multiple phase centre DPCA for airborne radar". In: *Proceedings of the 1991 IEEE National Radar Conference*. 1991, pp. 36–40. DOI: 10.1109/NRC. 1991.114720.
- [22] Delphine Cerutti-Maori and Ishuwa Sikaneta. "A Generalization of DPCA Processing for Multichannel SAR/GMTI Radars". In: *IEEE Transactions on Geoscience and Remote Sensing* 51.1 (2013), pp. 560–572. DOI: 10.1109/TGRS.2012.2201260.
- [23] Kang Xueyan et al. "Radial velocity ambiguity mitigation of moving target by dual-subband ATI approach with a two-channel SAR". In: 2014 International Radar Conference. 2014, pp. 1–6. DOI: 10.1109/RADAR.2014.7060468.
- [24] Xueyan Kang et al. "Two-antenna SAR/ATI with multiple carrier frequencies for radial velocity estimation of moving targets". In: 2016 17th International Radar Symposium (IRS). 2016, pp. 1– 5. DOI: 10.1109/IRS.2016.7497308.
- [25] Zhang Hui and Hong Jun. "Sensitivity analysis of Along-Track Interferometric Synthetic Aperture Radar (ATI-SAR) in the presence of squint". In: *IET International Radar Conference 2013*. 2013, pp. 1–5. DOI: 10.1049/cp.2013.0181.
- [26] Fu Jiayu et al. "Performance Analysis of GEO-LEO SAR ATI". In: 2024 IEEE International Conference on Signal, Information and Data Processing (ICSIDP). 2024, pp. 1–8. DOI: 10.1109/ICSIDP62679.2024.10868657.
- [27] Zhibin Wang et al. "A Least-Squares-Based Algorithm for Estimating ATI SAR Interferometric Phase Errors". In: 2024 IEEE International Conference on Signal, Information and Data Processing (ICSIDP). 2024, pp. 1–5. DOI: 10.1109/ICSIDP62679.2024.10867908.
- [28] Xiao Yang and Junfeng Wang. "GMTI based on a combination of DPCA and ATI". In: *IET International Radar Conference 2015*. 2015, pp. 1–5. DOI: 10.1049/cp.2015.1202.
- [29] Fang Qin, Xiaoling Zhang, and Min Dong. "A method of hybrid ATI and DPCA technique to detect moving target". In: 2006 CIE International Conference on Radar. 2006, pp. 1–4. DOI: 10.1109/ICR.2006.343187.
- [30] Wolfgang Pitz and David Miller. "The TerraSAR-X Satellite". In: *IEEE Transactions on Geoscience and Remote Sensing* 48.2 (2010), pp. 615–622. DOI: 10.1109/TGRS.2009.2037432.
- [31] Franz Meyer et al. "Performance analysis of the TerraSAR-X Traffic monitoring concept". In: *IS-PRS Journal of Photogrammetry and Remote Sensing* 61.3 (2006). Theme Issue: Airborne and Spaceborne Traffic Monitoring, pp. 225–242. ISSN: 0924-2716. DOI: https://doi.org/10.1016/j.isprsjprs.2006.08.002. URL: https://www.sciencedirect.com/science/article/pii/S0924271606000943.
- [32] Stefan V. Baumgartner and Gerhard Krieger. "Dual-Platform Large Along-Track Baseline GMTI". In: *IEEE Transactions on Geoscience and Remote Sensing* 54.3 (2016), pp. 1554–1574. DOI: 10.1109/TGRS.2015.2483019.

[33] Gerhard Krieger et al. "TanDEM-X: A Satellite Formation for High-Resolution SAR Interferometry". In: *IEEE Transactions on Geoscience and Remote Sensing* 45.11 (2007), pp. 3317–3341. DOI: 10.1109/TGRS.2007.900693.

- [34] T.J. Nohara. "Comparison of DPCA and STAP for space-based radar". In: *Proceedings International Radar Conference*. 1995, pp. 113–119. DOI: 10.1109/RADAR.1995.522530.
- [35] Zetao Wang et al. "Subspace-Augmented Clutter Suppression Technique for STAP Radar". In: *IEEE Geoscience and Remote Sensing Letters* 13.3 (2016), pp. 462–466. DOI: 10.1109/LGRS. 2016.2519765.
- [36] Zhihui Li et al. "Low-Complexity Off-Grid STAP Algorithm Based on Local Search Clutter Subspace Estimation". In: *IEEE Geoscience and Remote Sensing Letters* 15.12 (2018), pp. 1862–1866. DOI: 10.1109/LGRS.2018.2865536.
- [37] G. Ginolhac and P. Forster. "Performance analysis of a Robust Low-Rank STAP filter in low-rank Gaussian clutter". In: 2010 IEEE International Conference on Acoustics, Speech and Signal Processing. 2010, pp. 2746–2749. DOI: 10.1109/ICASSP.2010.5496218.
- [38] Chong Song et al. "A Moving Target Detection Method for Airborne Multichannel Circular SAR Based on Post-Doppler STAP". In: 2021 CIE International Conference on Radar (Radar). 2021, pp. 848–851. DOI: 10.1109/Radar53847.2021.10028274.
- [39] Christopher M. Teixeira. "Performance analysis of post-Doppler STAP". In: 2008 42nd Asilomar Conference on Signals, Systems and Computers. 2008, pp. 551–555. DOI: 10.1109/ACSSC. 2008.5074466.
- [40] Xiang Zhao et al. "Spatial Null Estimation in Beam-Space Post-Doppler Stap for Airborne Collocated Mimo Radar". In: *IGARSS 2018 2018 IEEE International Geoscience and Remote Sensing Symposium*. 2018, pp. 7890–7893. DOI: 10.1109/IGARSS.2018.8519200.
- [41] Magnus Gisselfält and Thomas Pernstål. "STAP analysis using multi-channel airborne radar data from flight trials". In: 2010 IEEE Radar Conference. 2010, pp. 407–411. DOI: 10.1109/RADAR. 2010.5494588.
- [42] Stefan V. Baumgartner and Gerhard Krieger. "A priori knowledge-based Post-Doppler STAP for traffic monitoring applications". In: 2012 IEEE International Geoscience and Remote Sensing Symposium. 2012, pp. 6087–6090. DOI: 10.1109/IGARSS.2012.6352218.
- [43] Jinfeng Hu et al. "A Novel Covariance Matrix Estimation via Cyclic Characteristic for STAP". In: *IEEE Geoscience and Remote Sensing Letters* 17.11 (2020), pp. 1871–1875. DOI: 10.1109/LGRS.2019.2957023.
- [44] D. W. Bliss et al. "GMTI MIMO radar". In: 2009 International Waveform Diversity and Design Conference. 2009, pp. 118–122. DOI: 10.1109/WDDC.2009.4800327.
- [45] Chun-Yang Chen and P. P. Vaidyanathan. "A Subspace Method for MIMO Radar Space-Time Adaptive Processing". In: 2007 IEEE International Conference on Acoustics, Speech and Signal Processing ICASSP '07. Vol. 2. 2007, pp. II-925-II-928. DOI: 10.1109/ICASSP.2007.366388.
- [46] Ting Wang et al. "A reduced-rank STAP algorithm for simultaneous clutter plus jamming suppression in airborne MIMO radar". In: 2017 18th International Radar Symposium (IRS). 2017, pp. 1–10. DOI: 10.23919/IRS.2017.8008095.
- [47] Ziying Hu, Wei Wang, and Fuwang Dong. "A Low-Complexity MIMO Radar STAP Strategy for Efficient Sea Clutter Suppression". In: *IEEE Geoscience and Remote Sensing Letters* 19 (2022), pp. 1–5. DOI: 10.1109/LGRS.2022.3175822.
- [48] A. K. M. Tohidur Rahman et al. "Target detection performance of coherent MIMO radar using Space Time Adaptive Processing". In: 2014 International Conference on Informatics, Electronics & Vision (ICIEV). 2014, pp. 1–5. DOI: 10.1109/ICIEV.2014.6850682.
- [49] Guohua Wang, Yilong Lu, and Jinping Sun. "STAP performance analysis for MIMO radar with waveform diversity". In: 2009 IEEE Radar Conference. 2009, pp. 1–6. DOI: 10.1109/RADAR. 2009.4976936.

[50] Fan Yang et al. "STAP Performance Evaluation for Spaceborne Radar Systems with Different Clutter Distribution Models". In: *IGARSS 2023 - 2023 IEEE International Geoscience and Remote Sensing Symposium*. 2023, pp. 6129–6132. DOI: 10.1109/IGARSS52108.2023.10282923.

- [51] Joachim H. G. Ender, Christoph H. Gierull, and Delphine Cerutti-Maori. "Improved Space-Based Moving Target Indication via Alternate Transmission and Receiver Switching". In: *IEEE Transactions on Geoscience and Remote Sensing* 46.12 (2008), pp. 3960–3974. DOI: 10.1109/TGRS. 2008.2002266.
- [52] Delphine Cerutti-Maori and Ishuwa Sikaneta. "Optimum GMTI Processing for Space-based SAR/GMTI Systems Theoretical Derivation". In: 8th European Conference on Synthetic Aperture Radar. 2010, pp. 1–4.
- [53] Delphine Cerutti-Maori and Ishuwa Sikaneta. "Optimum GMTI Processing for Space-based SAR/GMTI Systems Simulation Results". In: 8th European Conference on Synthetic Aperture Radar. 2010, pp. 1–4.
- [54] Delphine Cerutti-Maori, Ishuwa Sikaneta, and Christoph Gierull. "Ship detection with spaceborne multi-channel SAR/GMTI radars". In: *EUSAR 2012; 9th European Conference on Synthetic Aperture Radar.* 2012, pp. 400–403.
- [55] Delphine. Cerutti-Maori and Joachim H. G Ender. "An approach to multistatic spaceborne SAR/MTI processing and performance analysis". In: *IGARSS 2003. 2003 IEEE International Geoscience and Remote Sensing Symposium. Proceedings (IEEE Cat. No.03CH37477)*. Vol. 7. 2003, 4446–4449 vol.7. DOI: 10.1109/IGARSS.2003.1295542.
- [56] Yan Zhang, Yunhua Zhang, and Xueyan Kang. "Array configurations and space-time adaptive processing for spaceborne distributed GMTI radar". In: 2009 2nd Asian-Pacific Conference on Synthetic Aperture Radar. 2009, pp. 185–188. DOI: 10.1109/APSAR.2009.5374242.
- [57] Xianghai Li et al. "A Closed-Form Expression of STAP Performance for Distributed Aperture Coherence MIMO Radar". In: *IEEE Geoscience and Remote Sensing Letters* 21 (2024), pp. 1–5. DOI: 10.1109/LGRS.2024.3388513.
- [58] Xianghai Li et al. "A Novel Knowledge-Aided Training Samples Selection Method for Terrain Clutter Suppression in Hybrid Baseline Radar Systems". In: *IEEE Transactions on Geoscience and Remote Sensing* 60 (2022), pp. 1–16. DOI: 10.1109/TGRS.2022.3197992.
- [59] Mark Richards, J.A. Scheer, and W.A. Holm. *Principles of modern radar: Basic principles*. Jan. 2010, pp. 1–925.
- [60] R.P. Perry, R.C. DiPietro, and R.L. Fante. "SAR imaging of moving targets". In: *IEEE Transactions on Aerospace and Electronic Systems* 35.1 (1999), pp. 188–200. DOI: 10.1109/7.745691.
- [61] H Griffith. "Bistatic: introduction and historical background". In: *NATO SET-136 Lecture Series* (2009).
- [62] Alle-Jan van der Veen. "Array signal processing An algebraic approach". In: TU Delft, Faculty of Electrical Engineering, Mathematics, Computer Science Section Circuits, and System, 2022, pp. 50–62.
- [63] Lorenzo Iannini et al. "PRF Sampling Strategies for Swarmsar Systems". In: IGARSS 2019 -2019 IEEE International Geoscience and Remote Sensing Symposium. 2019, pp. 8621–8624. DOI: 10.1109/IGARSS.2019.8898476.
- [64] Fawwaz Ulaby, M Craig Dobson, and José Luis Álvarez-Pérez. *Handbook of radar scattering statistics for terrain*. Artech House, 2019.
- [65] Bo Yan et al. "A Target Detection and Tracking Method for Multiple Radar Systems". In: *IEEE Transactions on Geoscience and Remote Sensing* 60 (2022), pp. 1–21. DOI: 10.1109/TGRS. 2022.3183387.
- [66] Prabha Gopinathan, Natarajamani S, and Kirthiga S. "Direction-of-Arrival Estimation in Non-Linear Array with Gain-Phase Error Compensation." In: (May 2021). DOI: 10.21203/rs.3.rs-554578/v1.